POROSITY-SEISMIC VELOCITY RELATIONSHIP AND EVOLUTION

OF SHALLOW OCEANIC CRUST NEAR SPREADING CENTERS

OF THE PACIFIC AND ATLANTIC OCEAN

A DISSERTATION SUBMITTED TO THE GRADUATE DIVISION OF THE
UNIVERSITY OF HAWAII IN PARTIAL FULFILLMENT OF THE
REQUIREMENTS FOR THE DEGREE OF

DOCTOR OF PHILOSOPHY

IN

GEOLOGY AND GEOPHYSICS

AUGUST 1996

By

Rainer Ludwig

Dissertation Committee:

Gerard J. Fryer, Chairperson
Eduard Berg
L. Neil Frazer
Roy H. Wilkens
Alexander Malahoff

We certify that we have read this dissertation and that, in our opinion, it is satisfactory in scope and quality as a dissertation for the degree of Doctor of Philosophy in Geology and Geophysics.

DISSERTATION COMMITTEE

_____
Chairperson

_____

_____

_____

ACKNOWLEDGMENTS

ABSTRACT

In this dissertation, I investigate the relationship between measured seismic velocities and the porosity structure of young, shallow oceanic crust. Data from on-bottom seismic refraction experiments on the axis and flanks of the East Pacific Rise near 9°30'N provide the necessary input parameters for an iterative inversion algorithm which relates seismic velocities to the porosity structure of rocks using rock physics theories. Porosity models fitting the seismic data are non-unique, but for zero age crust the distribution of pore space over aspect ratio is bimodal. The maximum volume in the distribution occurs for high-aspect-ratio void space, such as vesicles, inter-pillow voids, and breccia, but the large Poisson's ratio associated with small shear-wave velocities can only be explained with another peak at very low aspect ratio, representing thin cracks and joints. A distinctive change in the porosity structure occurs at a depth of about 80 m below the seafloor, which I interpret as the Layer 2A/2B boundary in zero-age crust being a boundary between extrusives and sheeted dikes. The surficial high-porosity zone thickens rapidly away from the axis, probably from lava overflowing the top of the summit graben during extensive flank eruptions. By 120 ka age the surface porosity has decreased to about 20%, a decrease consistent with progressive alteration and associated crack sealing.

For a similar analysis on a hand-sample scale, I then analyze physical properties and ultrasonic measurements on 24 minicores recovered at the TAG hydrothermal mound during Ocean Drilling Program Leg 158. Seismic velocities, densities, porosities, and the distribution of pore shapes are extremely variable within very short distances of the mound, both horizontally and vertically. However, if the sulfide and sulfate samples are classified according to their mineralogy and their location within major internal zones of the mound, the measured physical properties exhibit distinct characteristics which I discuss in detail.

By applying rock physics theories, I present porosity distribution models for representative samples of each major lithologic zone within the TAG mound which are constrained by microscopic observations.

TABLE OF CONTENTS

LIST OF TABLES

LIST OF FIGURES

CHAPTER 1

INTRODUCTION

1.1 SEISMIC VELOCITY AND POROSITY STRUCTURE OF OCEANIC CRUST

A generally layered structure of ocean crust is recognized from remote seismic surveys by surface ships [e.g. *Solomon and Toomey*, 1992], by analogy with ophiolites, which are fragments of ocean crust exposed on land [*Casey et al.*, 1983; *Moores*, 1982], and by direct sampling of oceanic crust [e.g. *Francheteau et al.*, 1992]. Pelagic sediments overlie a sequence of basaltic volcanic rocks, a few hundred meters to 1 km thick, which comprises pillow basalts, massive flows and breccias. These are underlain by a sheeted dike complex, approximately 1 km thick, consisting of vertical sheet-like feeders for the overlying volcanic rocks. Beneath are up to several kilometers of gabbroic rocks, the coarse-grained rocks that crystallize from slowly-cooled magma, yielding an average crustal thickness of 7 km [*White et al.*, 1992].

Physical properties vary with depth and lithology. From ODP (Ocean Drilling Program) Hole 504B, the deepest basement hole anywhere in the oceans, it has been shown that porosity and permeability are highest in the upper most volcanics (seismic Layer 2A) which contain abundant open fractures [*Wilkens et al.*, 1991]. In the lower volcanics of seismic Layer 2B, porosity and permeability are lower because fractures are now filled with secondary minerals [*Pezard*, 1990]. Porosity than decreases drastically in the sheeted dikes of seismic Layer 2C.

Not many measurements have been made in very young oceanic crust. In the second chapter of my dissertation, I will use seismic refraction data that resolves the structure of the upper few hundreds of meters of young oceanic crust at the East Pacific Rise to determine a porosity structure by applying rock physics theories that relate seismic velocities to porosity.

Along zero-age crust of the EPR axis, anomalous high velocities and attenuation for the upper most crust indicate that the sheeted dikes extend very close to the surface [*Solomon and Toomey*, 1992]. Low seismic velocities in the top most 100 to 200 m-thick Layer 2A at the axis reflect high porosities and fracturing of the volcanics, and these low-velocity volcanics thicken outward for 1-3 km off-axis as flows accumulate [*McClain et al.*, 1985; *Purdy*, 1987; *Solomon and Toomey*, 1992; *Vera et al.*, 1990]. Seismic velocities increase sharply in the underlying 400-500 m of Layer 2B where higher confining pressure and/or cementation by secondary minerals result in lower porosities, and the underlying dikes of Layer 2C have still lower porosities and slightly higher velocities [*McClain et al.*, 1985; *Purdy*, 1987; *Solomon and Toomey*, 1992; *Vera et al.*, 1990]. The implication here is that lithology controls porosity and permeability and, hence, fluid circulation and hydrothermal alteration. Much greater volumes of seawater can circulate more freely through the heterogeneous, permeable and porous volcanic section than through the more uniform, massive sheeted dike section. The second chapter of this dissertation will discuss new findings about the Layer 2A/2B boundary near the EPR in greater detail.

Within the volcanic section, thick massive flows may locally act as barriers to circulation, whereas breccia zones can provide pathways for enhanced flow of seawater [*Hyndman and Salisbury*, 1983; *Pezard et al.*, 1992]. In the low-velocity Layer 2A at the top of the volcanic section, seismic velocities increase in older crust (10-100 Ma), which may in part be due to cementation of pore space with secondary minerals [*Houtz and*

Ewing, 1976; *Jacobson*, 1992; *Purdy*, 1987; *Wilkens et al.*, 1991]. The persistence of Layer 2A, however, indicates that circulation in the uppermost crust may continue for up to 10's of million years.

Chapter 3 of my dissertation presents results from physical properties measurements of seismic velocities, densities, and porosities of hand sample-scale rock specimens obtained by drilling into the hydrothermally active TAG mound. Implications from these measurements for the formation and subsurface structure as well as a proposed porosity distribution will be discussed in detail .

1.2 REFERENCES

Casey, J. F., J. F. Dewey, P. J. Fox, J. A. Karson, and E. Rosencrantz, Heterogeneous nature of oceanic crust and upper mantle: a perspective from the Bay of Islands ophiolite complex, in *The Sea*, edited by C. Emiliani, pp. 305-338, John Wiley and Sons, Inc., New York, 1983.

Francheteau, J., R. Armijo, J. L. Cheminee, R. Hekinian, P. Lonsdale, and N. Blum, Dyke complex of the East Pacific Rise exposed in the walls of Hess Deep and the structure of the upper oceanic crust, *Earth and Planetary Science Letters*, *111*, 109-121, 1992.

Houtz, R., and J. I. Ewing, Upper crustal structure as a function of plate age, *J. Geophys. Res.*, *81*, 2490-2498, 1976.

Hyndman, R. D., and M. H. Salisbury, The physical nature of the oceanic crust on the Mid-Atlantic Ridge, DSDP Hole 395A, in *Init.Repts. DSDP, 78B*, edited by W.G. Melson, and P.D. Rabinowitz, pp. 839-848, U.S. Govt. Printing Office, Washington, 1983.

Jacobson, R. S., Impact of crustal evolution on changes of the seismic properties of the uppermost ocean crust, *Rev. Geophys.*, *30*, 23-42, 1992.

McClain, J. S., J. A. Orcutt, and M. Burnett, The East Pacific Rise in cross section: a seismic model, *J. Geophys. Res.*, *90*, 8627-8639, 1985.

Moores, E. M., Origin and emplacement of ophiolites, *Reviews of Geophysics and Space Physics*, *20*, 735-760, 1982.

Pezard, P. A., Electrical properties of mid-ocean ridge basalt and implications for the structure of the upper oceanic crust in Hole 504B, *J. Geophys. Res.*, *95*, 9237-9264, 1990.

Pezard, P. A., R. N. Anderson, W. B. F. Ryan, K. Becker, J. C. Alt, and P. Gente, Accretion, structure and hydrology of intermediate spreading-rate oceanic crust from drillhole experiments and seafloor observations, *Marine Geophysical Researches*, *14*, 93-123, 1992.

Purdy, G. M., New observations of the shallow seismic structure of young oceanic crust, *J. Geophys. Res.*, *92*, 9351-9362, 1987.

Solomon, C. S., and D. R. Toomey, The structure of mid-ocean ridges, *Ann. Rev. Earth. Planet. Sci.*, *20*, 329-364, 1992.

Vera, E. E., J. C. Mutter, P. Buhl, J. A. Orcutt, A. J. Harding, M. E. Kappus, R. S. Detrick, and T. M. Brocher, The structure of 0- to 0.2-m.y.-old oceanic crust at 9°N on the East Pacific Rise from expanded spread profiles, *J. Geophys. Res.*, *95*, 15529-15556, 1990.

White, R. S., D. McKenzie, and R. K. O'Nions, Oceanic crustal thickness from seismic measurements and rare earth element inversions, *J. Geophys. Res.*, *97*, 19,683-19,715, 1992.

Wilkens, R. H., G. J. Fryer, and J. Karsten, Evolution of porosity and seismic structure of upper oceanic crust: importance of aspect ratios, *J. Geophys. Res.*, *96*, 17981-17995, 1991.

CHAPTER 2

POROSITY AND EVOLUTION OF THE SHALLOW OCEANIC CRUST AT THE EAST PACIFIC RISE

2.1 SUMMARY

From seismic velocities measured in on-bottom seismic refraction experiments on the axis and flanks of the East Pacific Rise near 9°30'N, we have inferred the porosity structure of uppermost extrusives of the ocean floor. Our technique is an iterative inversion of rock physics theories relating seismic velocities to porosity. Amplitude matching using synthetic seismograms shows that the Poisson's ratio at the seafloor must be at least 0.43, corresponding to a seismic shear-wave velocity of 0.48 km/s for zero age crust. This imposes tight constraints on the distribution of pore shapes. Porosity models fitting the seismic data are non-unique, but one feature is common to all: the distribution of pore space over aspect ratio is bimodal. The maximum volume in the distribution occurs for high-aspect-ratio void space, such as vesicles, inter-pillow voids, and breccia, but the large Poisson's ratio associated with small shear-wave velocities cannot be modeled without another peak at very low aspect ratio, representing thin cracks and joints. Such bimodal distribution qualitatively matches observations made at the Troodos ophiolite.

At zero age on the East Pacific Rise we obtain porosity bounds of 26 and 33% at the seafloor. This is a low-velocity ($V_p \sim 2.3$ km/s) layer of pillow and sheet flows which is about 35 m thick. The high porosity implies substantial fracturing. Porosity decreases to

7% at 82 m. We interpret this as the layer 2A/2B boundary associated with a distinctive change in the porosity structure indicating the top of the sheeted dikes. The surficial high-porosity zone thickens rapidly away from the axis, probably from lava flows overtopping the summit graben during extensive flank eruptions. By 120 ka age the surface porosity has decreased to about 20%, a decrease consistent with progressive alteration and associated crack sealing.

2.2 INTRODUCTION

It is widely recognized that the large difference between seismic measurements of seafloor basalts (compressional wave speed 2.5–4.0 km/s) and ultrasonic measurements of seafloor basalts in the laboratory (compressional wave speed as much as 7.0 km/s) result from fractures and cracks at a scale larger than that sampled by the dredging or drilling which provides the laboratory samples [*Wilkens et al.*, 1991]. That the extrusives contain an abundance of thin cracks at larger-than-hand-sample scale is clear from observations on ophiolites [*Ludwig et al.*, 1993a]. As the crust gets older and is progressively altered we can expect the total porosity to be reduced and the shape of the fractures and cracks to be modified. Some void space will be filled and thin cracks may be bridged by secondary mineralization, creating a structure which is much stiffer than the original fractured extrusives, even though the overall porosity reduction may be small [*Wilkens et al.*, 1991]. This crustal aging can be expected to increase seismic velocities much more than the alteration of the rock matrix itself will reduce velocities, especially in very young crust. The details of such crustal aging processes, however, are very poorly known. In particular, the age-dependence of the crustal porosity structure, and the interrelationships between crustal

alteration processes and the processes of construction of the oceanic crust are little more than conjecture.

For the Ocean Drilling Program's attempts to drill zero-age bare rock at the axis of a mid-ocean spreading center it was essential that the thickness of any surficial rubble layer (and hence the amount of drill-in casing necessary to stop collapse of a hole) be known. As a site survey for the East Pacific Rise site at 9°30'N, a series of detailed refraction surveys using bottom shots and receivers was carried out in 1991 [*Christeson et al.*, 1992; *Christeson et al.*, 1994]. The goals were to identify those sites for which drilling conditions would be most favorable, and to look at crustal construction and crustal evolution processes active from zero to 120 thousand years age. The seismic structure and inferences from that structure for crustal construction have been described by *Christeson et al.* [1994]. Seismic velocities alone, however, may be misleading. For example, a severely altered massive basalt may have an identical compressional-wave speed to a fresh but fractured basalt, but the two rocks will have experienced very different conditions and will undergo very different subsequent alteration histories. Porosity (and especially the distribution of porosity over pore shape), if it can be determined, tells a lot more about bottom conditions. With some assumptions about the properties of the rock matrix, and as long as there is some control on shear-wave velocities, it is possible to use compressional-wave velocities to infer both the porosity and the distribution of that porosity over different crack and pore shapes [*Ludwig et al.*, 1993*b*]. Such porosity information is much more informative about the state of the rock than seismic velocities alone. Porosities and pore aspect ratios from the East Pacific Rise site survey are the subject of this paper.

2.3 ROCK PHYSICS THEORIES

The velocities of seismic waves traveling through a rock are affected by the rock's porosity, the shape of its pores, and the media filling the pores. To infer porosity and pore shape from seismic velocities requires a theory relating these different properties, but as *Berge et al.* [1992] show, no theory is completely adequate for the high porosities and broad range of pore shapes present in the seafloor. There are two broad groups of theories: self-consistent theories, for which each crack is treated as if it were embedded in a cracked background medium (following rock physics orthodoxy we use "crack" to identify any pore space), and noninteraction theories, which treat each crack as if it were isolated in an uncracked background. Strictly, these theories are valid only for very small crack densities (i.e., for small porosities). As crack density is increased, self-consistent theories will tend to overestimate the softening effects of cracks, so for a given porosity the velocity they predict will be too small. Noninteraction theories underestimate the effects of cracks and err in the other direction, predicting velocities which are too high for a given porosity. The disagreement between the theories at large porosity can be significantly reduced by treating the total porosity as if it has been built up recursively, a small number of cracks at a time, with each new crack "feeling" the cracks which came before but being unaffected by the cracks which have yet to be added. The result is an hybrid or extended theory, which combines both noninteraction and self-consistent philosophies and which is correct at least to second order in the crack density [*Berge et al.*, 1992; *Cheng*, 1978] .

Berge [1991] performed numerical modeling and compared theoretical predictions with published laboratory measurements to test the various extended theories. She concluded that Kuster-Toksöz theory, a predominantly noninteraction theory which includes only a small amount of crack-crack interaction [*Cheng*, 1978; *Kuster and Toksöz*,

1974*a*; *Kuster and Toksöz*, 1974*b*] , slightly overestimates the softening effects of cracks if recast as an extended theory. Extended versions of self-consistent theories slightly underestimate the effects of cracks [*Berge*, 1991]. The known biases of these extended theories and the fact that these biases are small together mean that we can use the extended theories to impose bounds on the velocity-porosity relationships, for any hypothesized distribution of porosity over different crack shapes. These bounds are necessarily much tighter than those obtained by the classical method of *Hashin and Shtrikman* [1963], which does not take pore shape into consideration.

Berge et al. [1992] attempted to apply these extended theories to the seismic refraction survey data to establish bounds on the porosity of young seafloor at the East Pacific Rise. Their interpretations, however, were made without the benefit of any constraints on shear-wave velocities. Without such control, their results are misleading, as we shall see.

2.4 THE EAST PACIFIC RISE EXPERIMENTS

The seismic data were acquired from seven high-resolution, on-bottom seismic refraction experiments at the East Pacific Rise near 9°30'N (Figure 2.1) and one additional experiment at 12°50'N. They were carried out using the deep-towed explosive source NOBEL (Near Ocean Bottom Explosives Launcher) [*Koelsch et al.*, 1991]. Shots were detonated within a few meters of the seafloor and recorded at ocean bottom hydrophones. The near-bottom geometry of this experiment assured direct observation of the energy which had turned in the uppermost 500 meters of the crust, unlike traditional seismic refraction experiments with the source at the sea surface, where the desired resolution is hindered by the onset of the water wave [*Purdy*, 1987].
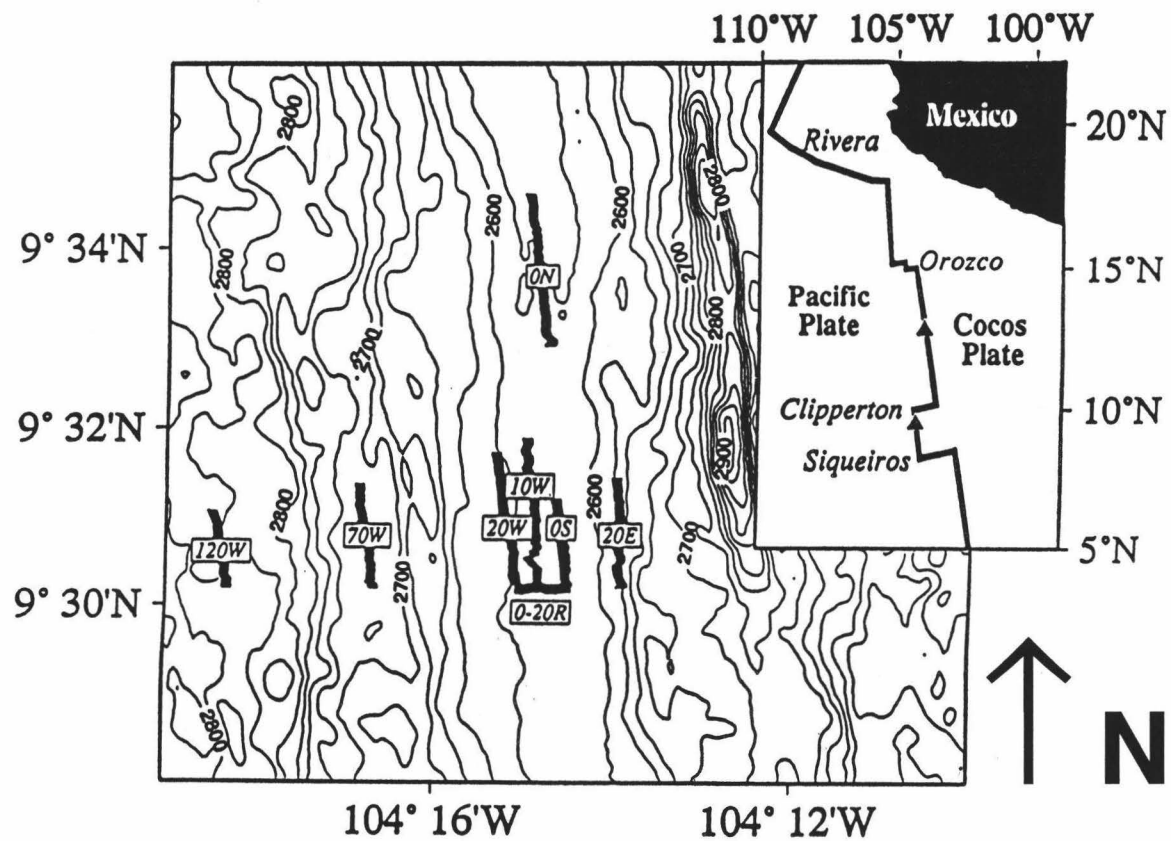
Figure 2.1 Location map of the seven high-resolution, on-bottom

seismic refraction experiments at the East Pacific Rise near 9°30'N.

Two experiments were located within the axial summit caldera (ASC), labeled 0N and 0S in Figure 2.1, five lines were located on the flanks of the East Pacific Rise axis, labeled 10W, 20W, 20E, 70W and 120W (the number represents the approximate age in kiloyears, i.e. ka). The additional experiment at 12°50'N was located near the western wall of the ASC and is referred to here as Line 0F.

Christeson et al. [1992] made a preliminary interpretation of the data using one-dimensional ray-tracing to match first arrival times. These models were used by *Berge et al.* [1992] to infer the porosity structure, but with only compressional-wave velocities to work from, the inversion for porosity is inadequately constrained. To improve on the simple travel-time inversion, *Christeson et al.* [1994] iteratively refined the models by constructing reflectivity synthetic seismograms to reproduce the observed amplitudes across the record sections while reproducing the partitioning of energy between arrivals. For the lines with the best data, the axial lines and line 120W, these syntheses impose quite strict constraints on the shear-wave velocity in the uppermost extrusives, despite the fact that no shear waves were themselves recorded. The final results of the velocity-depth model for these lines are shown in Table 2.1. The remaining flank lines (on 10, 20, and 70 ka crust) unfortunately suffered from technical problems (poor signal-to-noise from deteriorating hydrophones), so detailed amplitude modeling for those lines was not warranted.

The final models of *Christeson et al.* [1994] for the three lines on zero-age crust are shown in Figure 2.2. All have a thin surficial low-velocity layer, with compressional-wave velocities between 2.1 and 2.4 km/s, and shear-wave velocities of about 0.45 km/s. This translates into a Poisson's ratio σ of about 0.48, dramatically higher than the 0.3 typical of seafloor basalts [*Christensen*, 1972; *Christensen*, 1978]. Within 150 m of the seafloor, however, seismic velocities increase rapidly, exceeding 5 km/s for compressional waves and 2.7 km/s for shear waves, to yield the more basalt-typical Poisson's ratio $\sigma=0.3$.

Table 2.1. Velocity - depth model for young upper oceanic crust at the East Pacific Rise near 9°30' N and 12°50' N and total porosity values after extended Kuster - Toksöz Modeling (KT+) and Extended Walsh Modeling (Walsh+).

Depth [m]	V_p [km/s]	V_s [km/s]	Total Porosity [%] (KT+)	Total Porosity [%] (Walsh+)
Line 0 S				
0 - 32	2.33 - 2.38	0.47 - 0.48	**27.2 - 26.1**	**30.2 - 29.0**
32 - 72	2.38 - 4.18	0.48 - 2.21	26.1 - 8.0	29.0 - 8.9
72 - 82	4.18 - 4.19	2.21 - 2.26	8.0 - 6.9	8.9 - 7.5
82 - 129	4.19 - 5.00	2.26 - 2.67	6.9 - 5.2	7.5 - 5.9
129 - 209	5.00 - 5.21	2.67 - 2.78	5.2 - 4.7	5.9 - 5.2
Line 0 N				
0 - 55	2.11 - 2.40	0.42 - 0.48	**28.4 - 26.0**	**33.2 - 28.8**
55 - 137	2.40 - 4.90	0.48 - 2.65	26.0 - 5.4	28.8 - 6.2
137 - 177	4.90 - 4.97	2.65 - 2.68	5.4 - 5.2	6.2 - 5.7
177 - 192	4.97 - 5.17	2.68 - 2.79	5.2 - 4.6	5.7 - 5.1
192 - 322	5.17 - 5.21	2.79 - 2.81	4.6 - 4.3	5.1 - 4.7
Line 0 F				
0 - 42	2.25 - 2.28	0.45 - 0.46	**27.6 - 27.3**	**31.0 - 30.7**
42 - 122	2.28 - 5.14	0.46 - 2.78	27.3 - 4.8	30.7 - 5.2
122 - 132	5.14 - 5.16	2.78 - 2.79	4.8 - 4.7	5.2 - 5.2
132 - 162	5.16 - 5.29	2.79 - 2.86	4.7 - 4.1	5.2 - 4.5
162 - 222	5.29 - 5.37	2.86 - 2.90	4.1 - 3.7	4.5 - 4.1
Line 120W (a)				
0 - 107	2.63 - 2.63	0.53 - 0.53	19.8	21.1
107 - 157	2.63 - 4.18	0.53 - 2.26	19.8 - 6.9	21.1 - 7.5
157 - 287	4.18 - 4.50	2.26 - 2.43	6.9 - 5.8	7.5 - 6.4
287 - 307	4.50 - 4.90	2.43 - 2.65	5.8 - 5.4	6.4 - 6.2
307 - 357	4.90 - 5.02	2.65 - 2.71	5.4 - 5.1	6.2 - 5.9
Line 120W (b)				
0 - 137	2.63 - 3.35	0.53 - 0.70	19.8 - 15.1	21.1 - 16.1
137 - 187	3.35 - 4.18	0.70 - 2.26	15.1 - 6.9	16.1 - 7.5
187 - 317	4.18 - 4.50	2.26 - 2.43	6.9 - 5.8	7.5 - 6.4
317 - 337	4.50 - 4.90	2.43 - 2.65	5.8 - 5.4	6.4 - 6.2
337 - 387	4.90 - 5.02	2.65 - 2.71	5.4 - 5.1	6.2 - 5.9
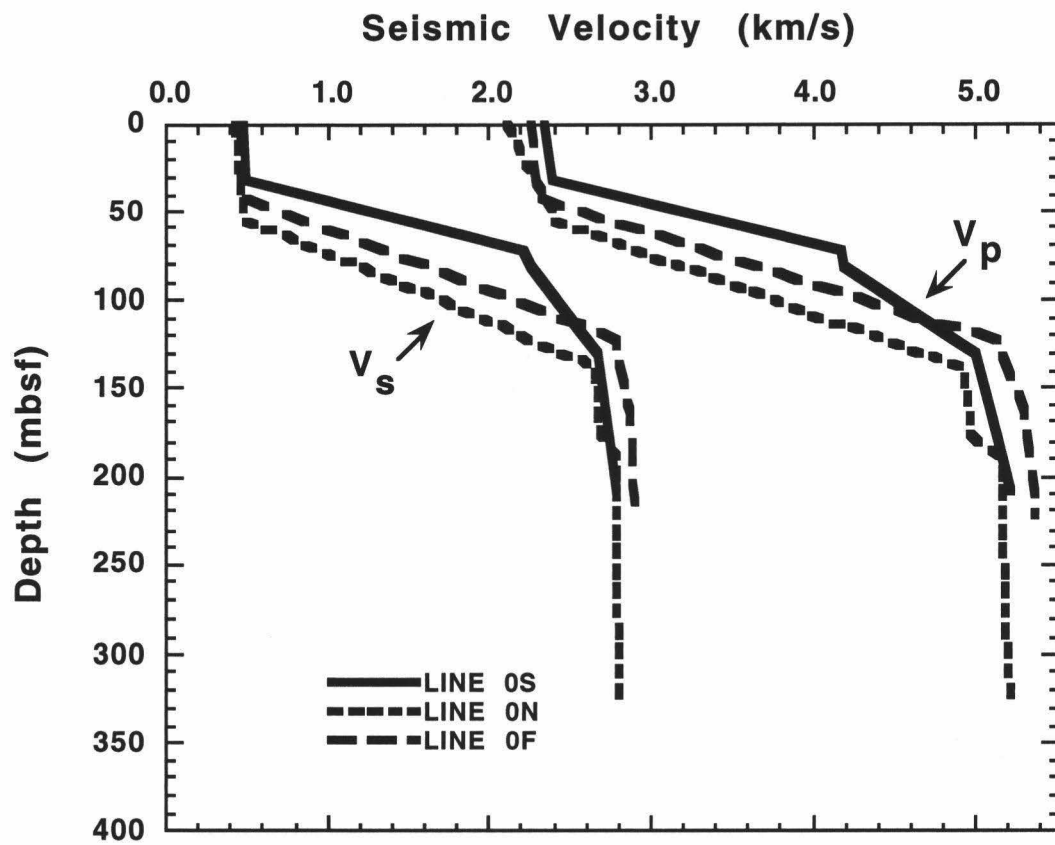
Figure 2.2 Velocity-depth model for zero age crust near 9°30'N and 12°50'N (after Christeson et al., 1994).

The structure for the 120 ka old crust located approximately 6 km west of the ASC is shown in Figure 2.3. Two different models are suggested by *Christeson et al.* [1994], 120W(a) and 120W(b), which basically differ in the thickness and velocity gradient of the surficial low-velocity layer. In Model 120W(a) the surficial layer is 100 m thick and has a constant compressional wave velocity of 2.63 km/s and a constant shear wave velocity of 0.53 km/s. In Model 120W(b) the surficial layer is a 140 m-thick gradient zone, with compressional wave velocity increasing from 2.63 to 3.35 km/s and shear wave velocity increasing from 0.53 to 0.70 km/s. Neither model is perfect. 120W(b) does marginally better at reproducing secondary arrivals, but *Christeson et al.* [1994] prefer Model 120W(a) because it does better at reproducing a triplication in the data.

2.5 POROSITY MODELS

In order to interpret seismic data by applying the extended theories, which relate seismic velocities to porosities, it is necessary to assume a distribution of pore shapes and their relative contribution to the total porosity. Unfortunately, the availability even of total porosity information is very limited. Thermal neutron porosity logs in ocean drill holes can be used to estimate porosity, but only a few quality crustal measurements have been made, and even these are open to interpretation for our depth range of interest, the uppermost 100 m below the seafloor [*Broglia and Ellis*, 1990] . To estimate pore aspect ratio spectra for the top few hundred meters of oceanic layer 2, *Wilkens et al.* [1991] supplemented well log data with laboratory measurements of velocity made on basalt samples from DSDP/ODP drillholes and by making inferences from field observations of ophiolites. Using Kuster-Toksöz theory, *Wilkens et al.* [1991] were able to show that progressive crack sealing of a single seafloor structure can explain both the porosities and seismic velocities seen at Hole

15
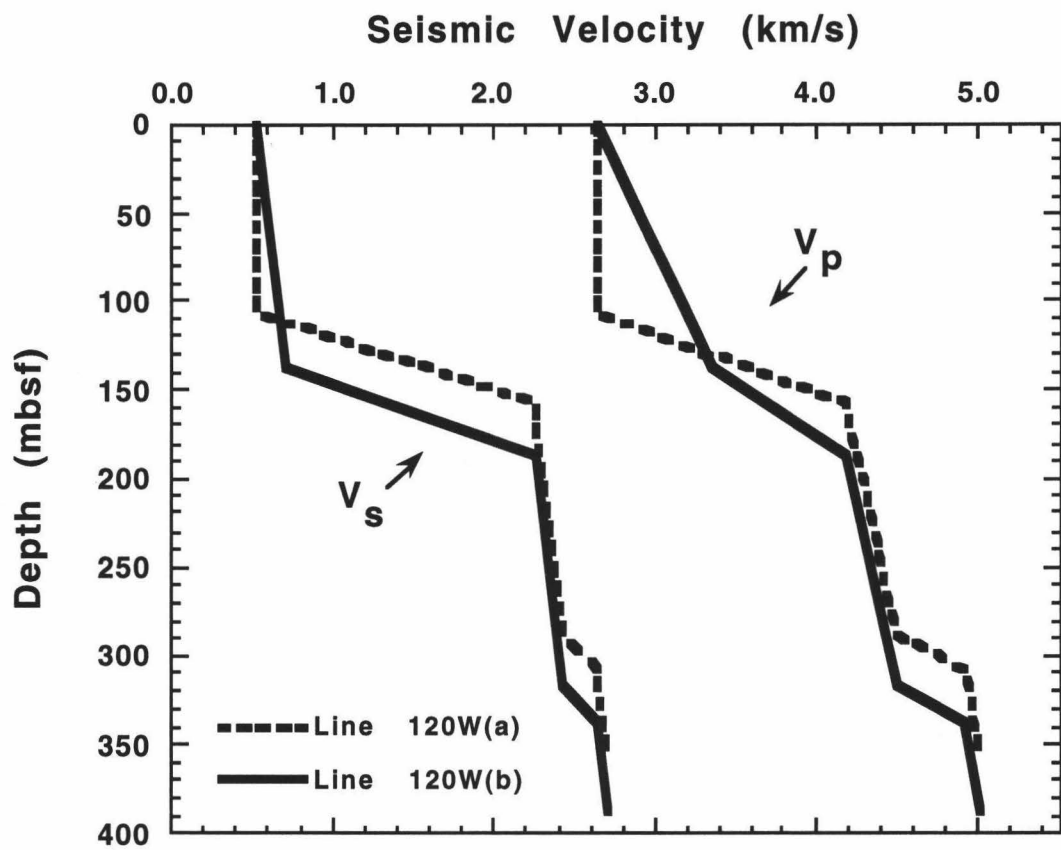
Figure 2.3. Velocity-depth model for approximately 120,000 year old crust near 9°30'N west of the East Pacific Rise's axial summit caldera (after Christeson et al., 1994).

504B (6 ma) and 418A (100 ma). Guided by the *Wilkens et al.* [1991] results, *Berge et al.* [1992] attempted to fit a porosity model to the East Pacific Rise site survey data which was the minimum modification of the Wilkens et al. model for Hole 504B. *Berge et al.* [1992] only had compressional-wave velocities to work from, the initial seismic interpretations of *Christeson et al.* [1992]. The Poisson's ratio implicit in the work of *Berge et al.* [1992] is about 0.2 for the surficial low-velocity layer, significantly less than the value of greater than 0.45 determined by *Christeson et al.* [1994] from their detailed reanalysis. Because of this discrepancy, the *Berge et al.* [1992] estimates of porosity (26–43% for zero-age crust) must be dismissed.

To determine the porosity structure we applied the extended Kuster-Toksöz and extended Walsh theories [*Walsh*, 1969] to a succession of porosity models to try to reproduce the seismic velocities given in Table 1. For each line, the starting model we chose for this iterative scheme was the appropriate porosity model from *Berge et al.* [1992], which matches the compressional-wave velocities but not the shear-wave velocities. The *Berge et al.* [1992] solution for Line 0S and its similarity to the Wilkens et al. model for Hole 504B is shown in Figure 2.4, and specifies the porosity within each of eight aspect ratio bins ranging from $\alpha=0.5$ to $\alpha=0.001$ (larger aspect ratios, e.g., vesicles with $\alpha=1$ or tubes and inter-pillow voids with $a>1$, are lumped into the $\alpha=0.5$ bin; this is legitimate because the dependence of seismic velocity on aspect ratio is very small at such large aspect ratios). Using the extended theories, we computed the theoretical velocities for the model, compared the result to Table 2.1, and adjusted the model by changing the contribution to porosity in each bin. As porosity at any particular aspect ratio is adjusted, both V_p and V_s are affected. Very roughly, an increasing population of thin, water-filled cracks ($a<0.01$) will reduce V_s faster than it reduces V_p, while an increasing population of thick cracks ($a>0.01$) will reduce V_p faster than V_s [*Shearer*, 1988]. From this knowledge
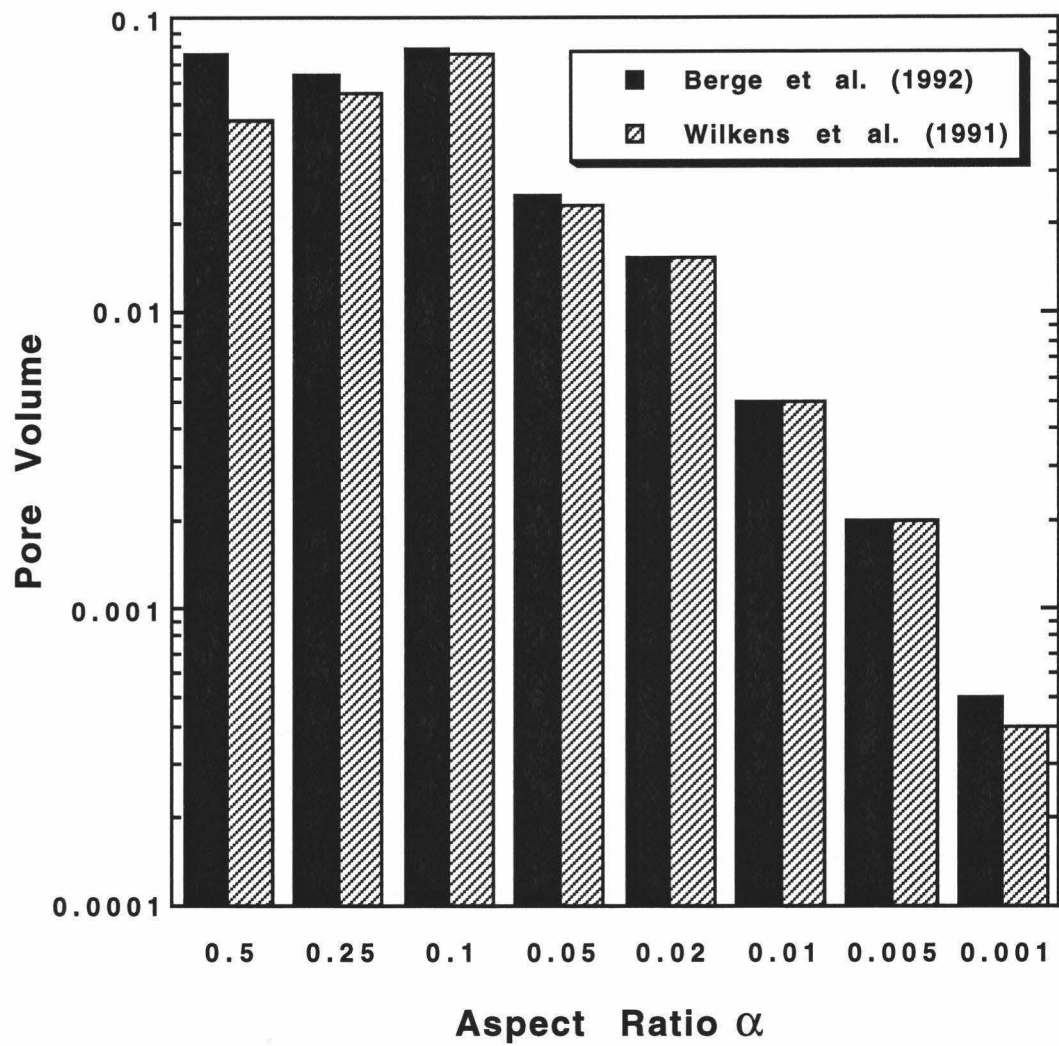
Figure 2.4. The best-fitting aspect ratio distribution for Line 0S by Berge et al. (1992), modeling compressional-wave velocities only. This solution was constrained by minimum modifications to the results by Wilkens et al. (1991) model for Hole 504B.

it is relatively easy to work out how to adjust the porosity at each aspect ratio to achieve the desired velocities.

Our final pore shape distributions for the uppermost layer of Line 0S, using the extended Kuster-Toksöz and the extended Walsh theories are shown in Figure 2.5. How far we were forced to diverge from the distribution obtained by *Berge et al.* [1992] in order to satisfy the velocity-depth models of zero age crust (Figure 2.2) is shown in Figure 2.6. While several slightly different aspect ratio distributions can be found which satisfy the seismic velocities, all require a decrease in the concentration of intermediate aspect ratio pores and a substantial increase in the concentration of low aspect ratio pores (i.e., thin cracks and joints). Only by increasing the proportion of low aspect ratio features can we obtain the required low shear wave velocities. The bimodal distribution of pore space, broad peaks at high and low aspect ratio with a distinct dip between, was required for every one of the lines we analyzed. While the major contribution to the total porosity of oceanic crust comes from high-aspect-ratio void space such as vesicles, inter-pillow voids and breccia, a significant population of very low aspect-ratio cracks is demanded by the data.

By summing the porosities in each aspect ratio bin, we obtain the total porosity, with the extended Walsh modeling providing us an upper porosity bound and the extended Kuster-Toksöz modeling provided a lower bound. The resulting porosity bounds are displayed as functions of depth for the zero-age lines in Figure 2.7. The porosities are also listed in Table 2.1. In all our models the difference between the higher and the lower bounds is less than 5% for the uppermost crustal layer and less than 2% for the deeper layers.

Figure 2.7 illustrates a drastic decrease in porosity for zero age crust at the base of the surficial layer. While the total porosity Φ decreases only slightly from approximately 33% to 26% within a depth of 30 to 50 m below the seafloor, an abrupt reduction of Φ to

Figure 2.5. Bimodal aspect ratio distribution of zero age crust at line 0 S at the seafloor after using extended Kuster - Toksöz (KT+) and extended Walsh (Walsh+) theory.
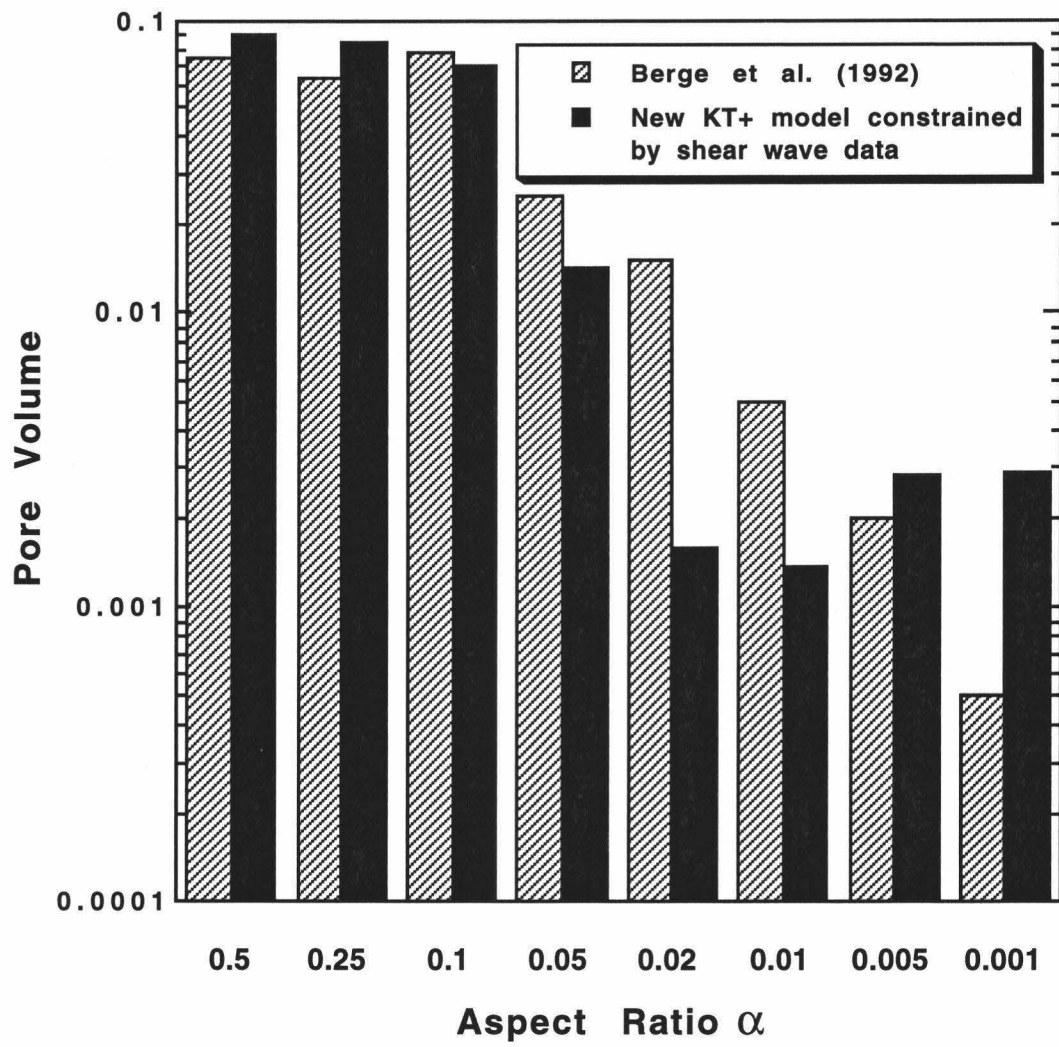
Figure 2.6. Comparison between new bimodal aspect ratio distribution constrained by modeling seismic compressional and shear wave data using the extended Kuster Toksöz (KT+) theory and the model proposed by Berge et al. (1992).
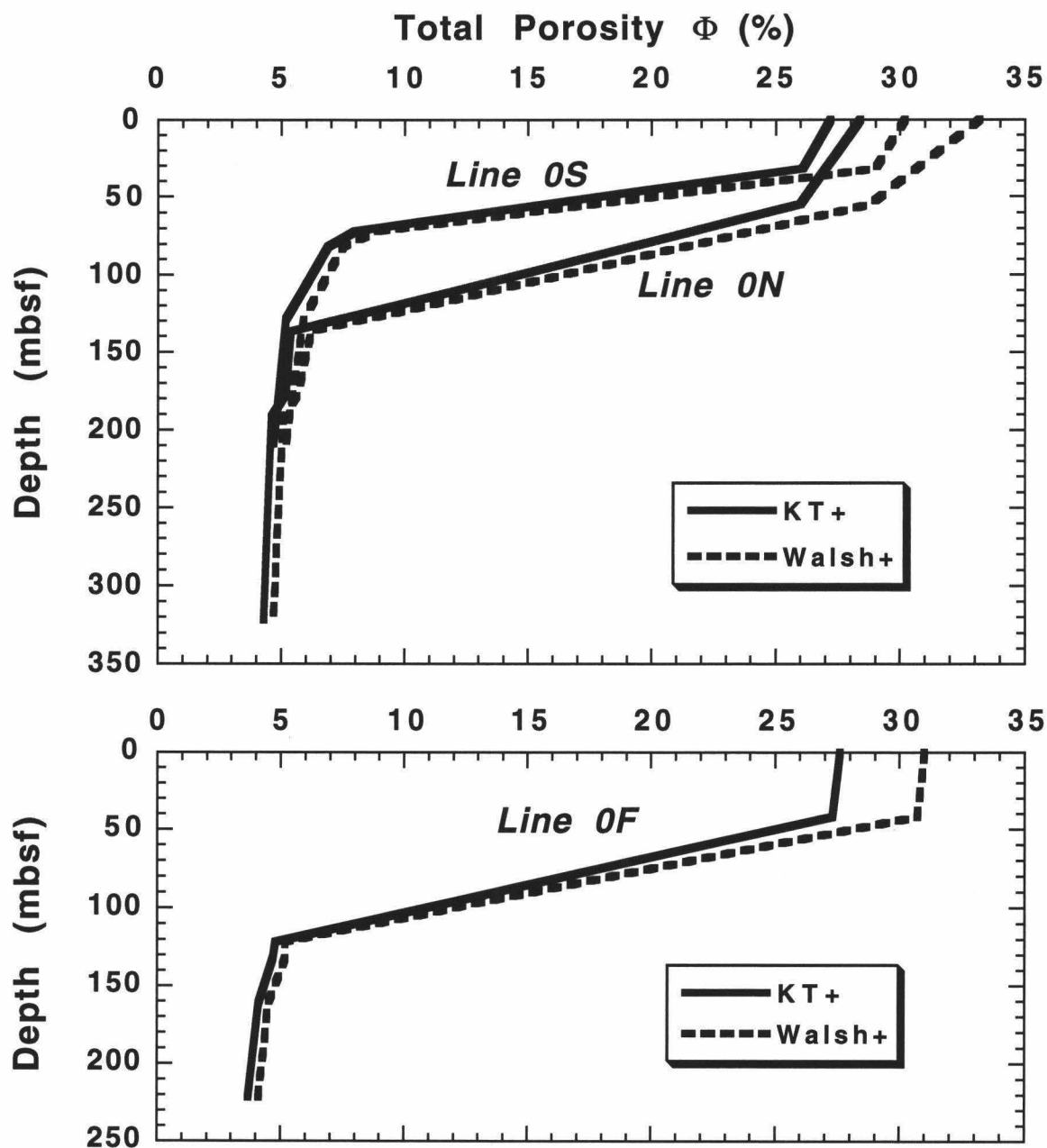
Figure 2.7. Total porosity structure for zero age lines located within the axial summit caldera of the East Pacific Rise. Lines 0S and 0N were located near 9°30' N, Line 0F near 12°50' N. The extended Kuster-Toksöz (KT+) modeling provides a lower porosity bound and the extended Walsh (Walsh +) modeling provides an upper bound.

less than 10% follows within the next 40 to 80 m. The corresponding aspect ratio distribution for 82 m depth on line 0S is shown in Figure 2.8. We find that the population of thin cracks is significantly less than at the surface, suggesting a progressive sealing of thin cracks with depth. We note that such behaviour was predicted by *Wilkens et al.* [1991] and has been measured in older crust by *Shaw* [1994].

In Figure 2.9 we show porosity results for 120 ka crust. The two figures correspond to the two solutions of *Christeson et al.* [1994], model 120W(a) with a constant-velocity surficial layer model and model 120W(b) with a surficial velocity gradient. For these structures the decline of porosity Φ is not as prominent as for the zero-age crust. Total porosity reduces from approximately 20% (significantly less than the surface porosity of about 30% for zero-age crust) to less than 8% at a depth of 160 to 190 m below the seafloor. Figure 2.10 shows the aspect ratio distribution at the seafloor for Line 120W. There is a significant reduction in the concentration of small aspect ratio pore spaces compared to the porosity structure for the upper zero age crust. However, not all of the thin cracks get sealed by the alteration of oceanic crust during the first 120 ka.

2.6 DISCUSSION

2.6.1 The Technique

The two extended rock physics theories of *Berge et al.* [1992] have proven useful in imposing constraints on porosity from a given seismic velocity structure (e.g., Figures 2.7 and 2.9), although it must be recognized that those constraints are only as good as the porosity models. Our technique to fit a porosity model to seismic velocities is essentially one of trial and error, a reasonably effective way to find a solution when only a few parameters (in our case the pore volume within each of eight aspect ratio bins) are to be
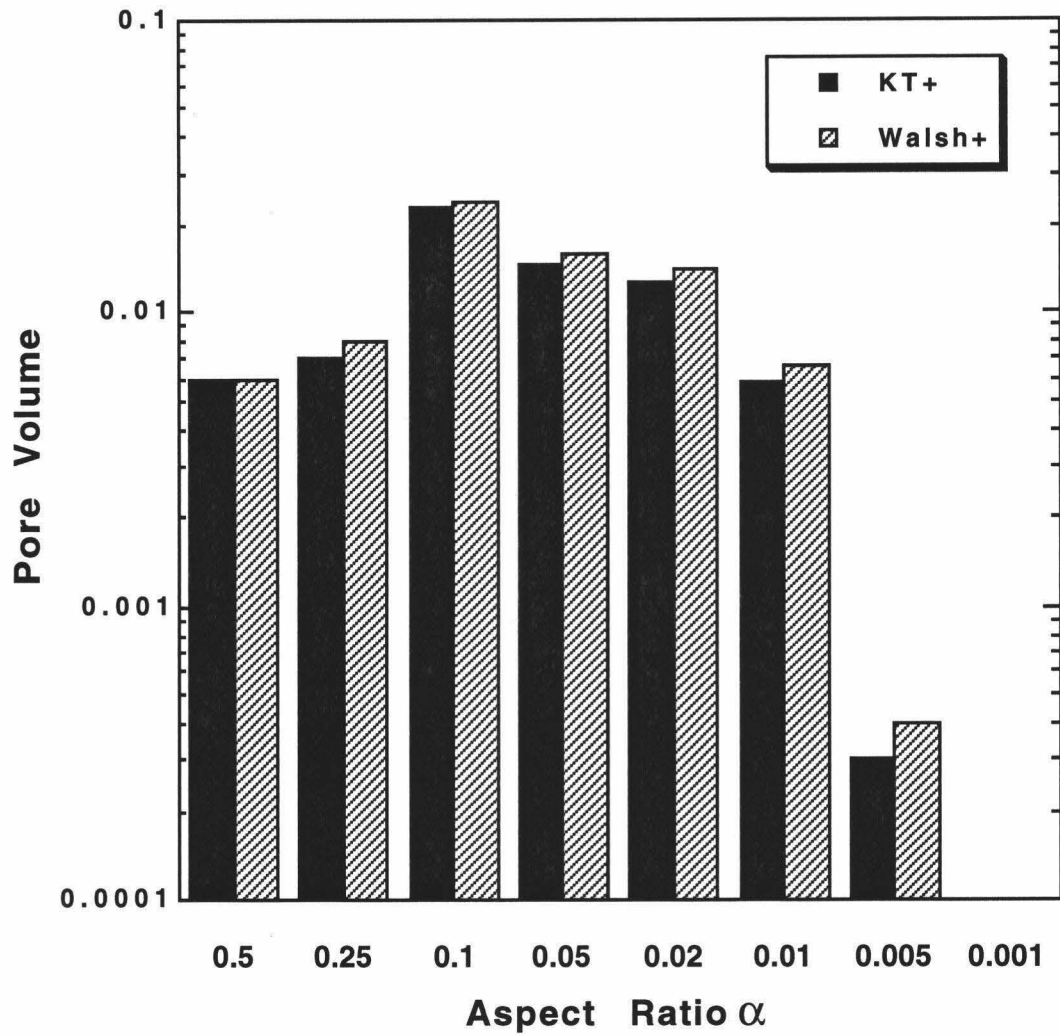
Figure 2.8. Aspect Ratio distribution of zero age crust, line 0S at a depth of 82 meters below the seafloor after using extended Kuster - Toksöz (KT+) and extended Walsh (Walsh+) theory. The total porosity $\Phi = 6.9\%$ for the KT+ model and $\Phi = 7.5\%$ for the Walsh+ model.
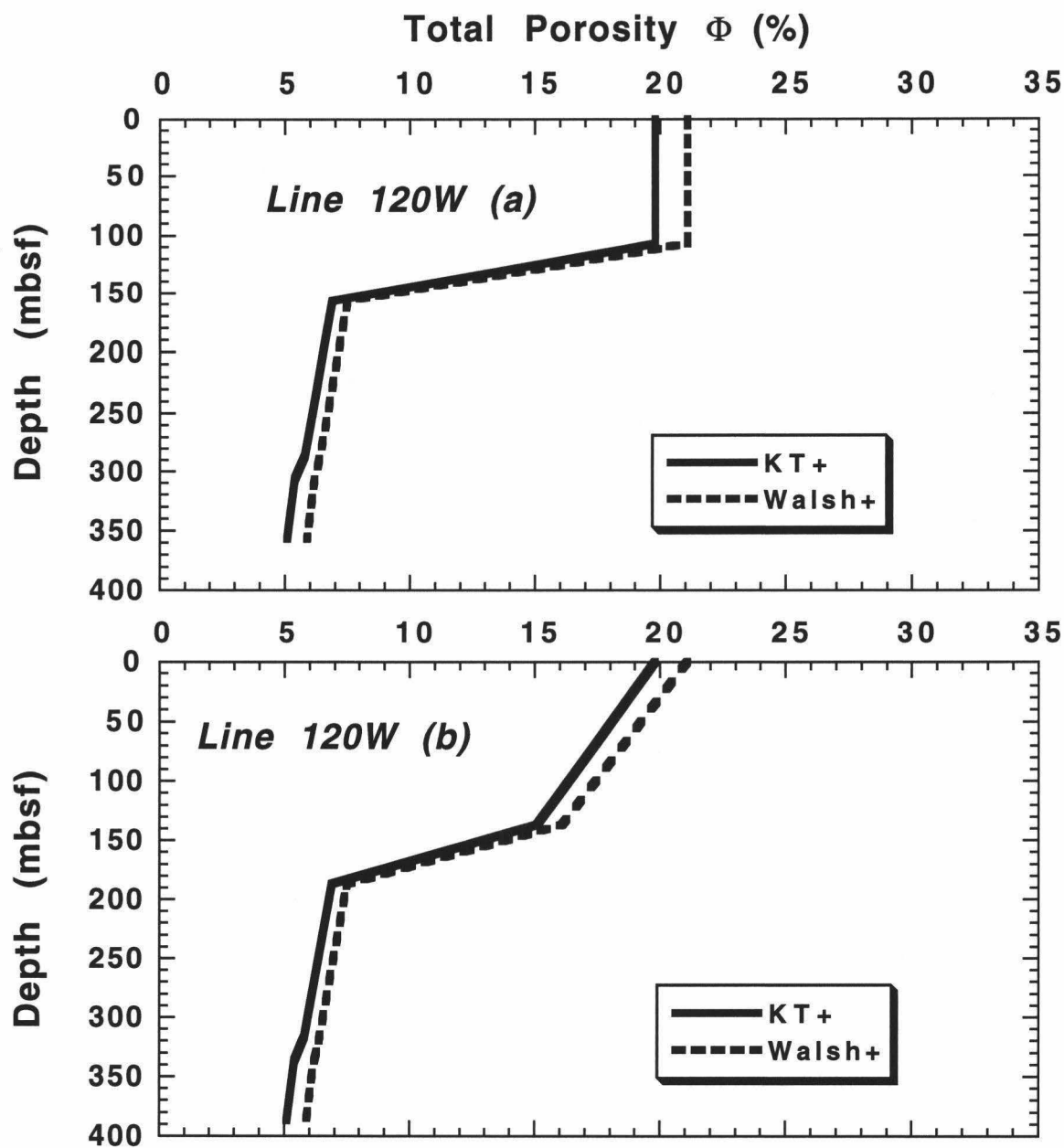
Figure 2.9. Total porosity structure for 120 ka crust at Line 120W. The two graphs correspond to the two solutions of Christeson et al. (1994). Model 120W (a) has a constant-velocity surficial layer and model 120W(b) has a surficial velocity gradient. The extended Kuster-Toksöz (KT+) modeling provides a lower porosity bound and the extended Walsh (Walsh +) modeling provides an upper bound.
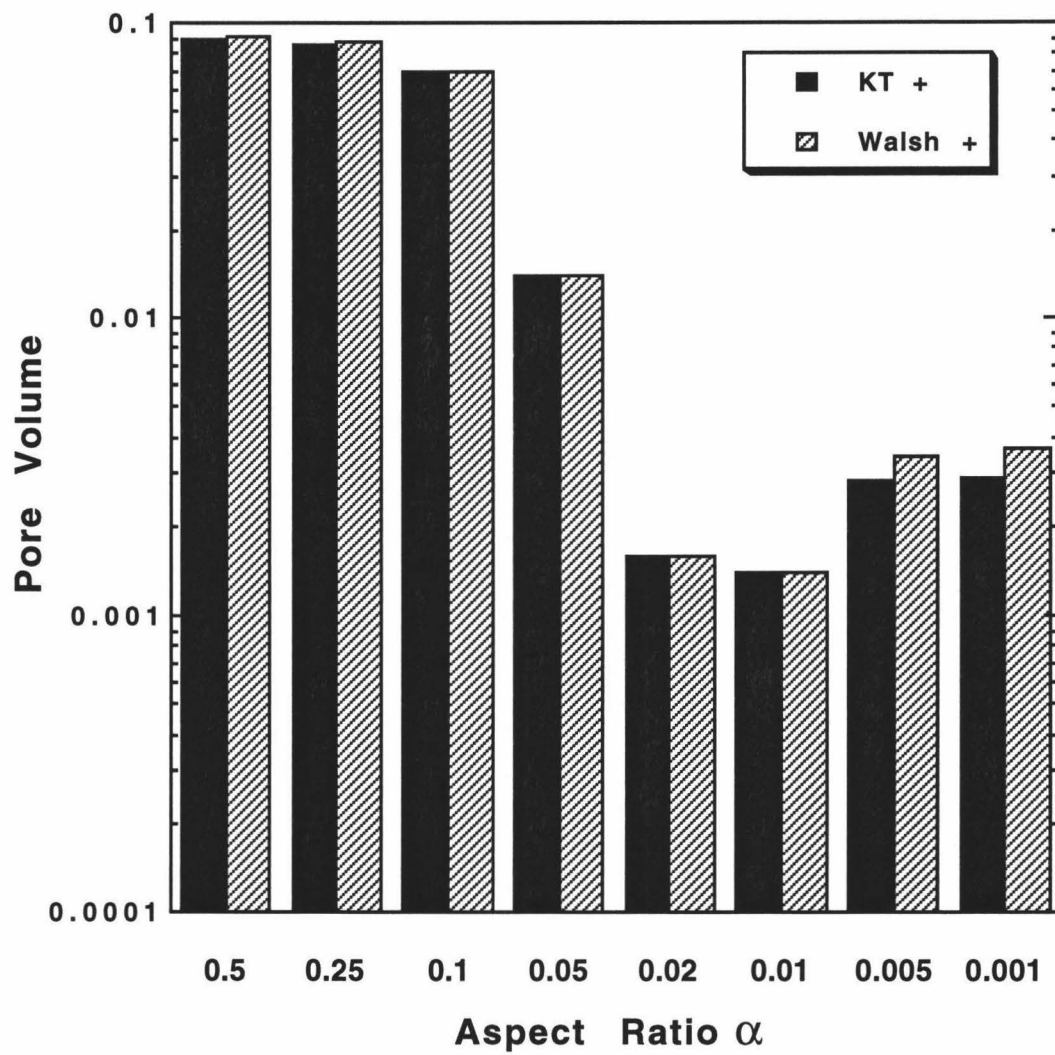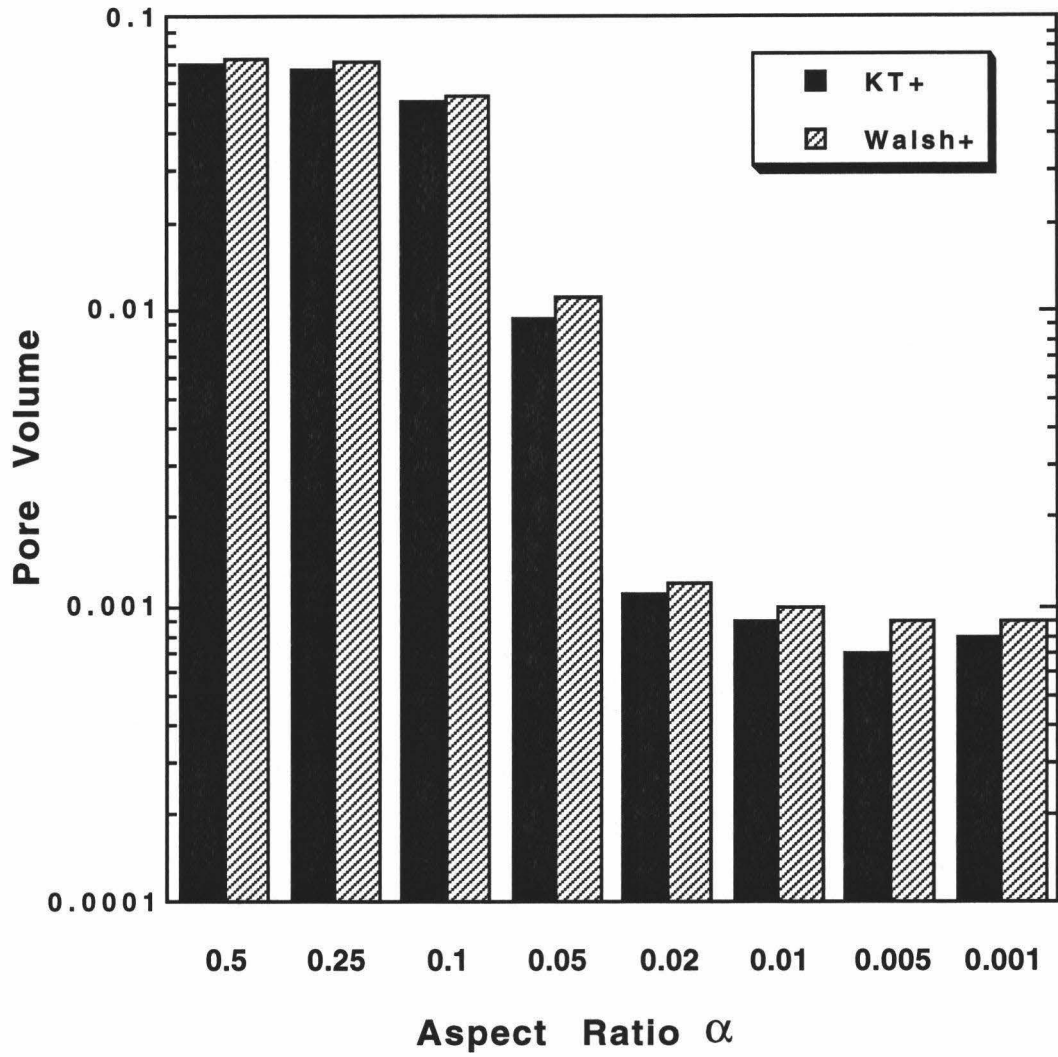
Figure 2.10. Aspect Ratio distribution of 120 ka crust for line 120W at the seafloor after using extended Kuster - Toksöz (KT+) and extended Walsh (Walsh+) theory. The total porosity $\Phi = 19.8\%$ for the KT+ model and $\Phi = 21.1\%$ for the Walsh+ model.

determined. Although this parameter estimation problem does not have a unique solution, for the East Pacific Rise data all satisfactory models were qualitatively similar: we were forced to adopt a bimodal aspect ratio distribution, with a subsidiary peak near aspect ratio of 0.001, to satisfy the high Poisson's ratio. The same general form was obtained regardless of the starting model. The entire procedure would lend itself well to a Monte Carlo search of solution space, which would also yield some idea of model uniqueness. We have not yet attempted such automation.

2.6.2 Comparison with the Troodos Ophiolite

The bimodal aspect ratio distribution displayed in Figure 2.5 demonstrates that the bulk of the porosity is in near-equant pores (i.e., aspect ratio near unity), but that there is a significant population of thin cracks. There may actually be more structure to the aspect ratio distribution than we are capable of detecting. From direct measurements of outcrops and from image analysis of outcrop photographs, *Ludwig et al.* [1993a] report a trimodal distribution of porosity in seafloor extrusives of the Troodos Ophiolite, Cyprus. The details for the Upper Pillow Lavas at Troodos are given by *Ludwig et al.* [1993a]: at formation the extrusives had 13% porosity from vesicles, inter-pillow voids and vugs (aspect ratio 1.0–0.5), 4% porosity from selvages and veins (aspect ratio 0.1–0.05), and 2–3% from thin cracks and joints (aspect ratio ~0.001). The porosity estimates of *Ludwig et al.* [1993a] are very crude, however, as they are estimates of the properties of three-dimensional structure from two-dimensional exposures. Our own estimates of porosity in the 0.5 and 0.25 bins are not entirely independent (our resolution improves at smaller aspect ratios), so we cannot resolve the higher aspect ratio peaks of *Ludwig et al.* [1993a]. At smaller aspect ratios ($\alpha < 0.005$), however, the Troodos field observations do broadly match the Troodos field

27

observations. In particular, neither suite of measurements finds a significant population of cracks in the aspect ratio range from 0.03 to 0.007.

2.6.3 The Layer 2A/2B Boundary

The seismic models of *Christeson et al.* [1994] all show a dramatic velocity increase at the base of the surficial low-velocity zone. This transition deepens with age, starting at only 30 m depth at zero age but deepening to more than 100 m at 120 ka. The surficial low velocity layer and the bulk of the transition zone beneath it (i.e., all material with a P–velocity of less than 4.5–5.0 km/s) comprise the classical Layer 2A [*Houtz and Ewing*, 1976], and the higher velocity material beneath is Layer 2B. The 2A/2B boundary has variously been explained either as the lithologic boundary between the extrusive sequence and the underlying sheeted dike complex [*Christeson et al.*, 1992; *Harding et al.*, 1993; *Herron*, 1982; *Toomey et al.*, 1990] or as a porosity boundary within the extrusives. A porosity boundary could either be an upward propagating metamorphic front generated by secondary mineralization (open pores above, sealed pores below) [*Rohr et al.*, 1988; *Vera et al.*, 1990; *Wilkens et al.*, 1991] or a downward propagating cracking front controlled by local tectonics [*McClain et al.*, 1985]. The downward propagating front can be dismissed, because the zone of active tectonism is much broader than the zone over which layer 2A thickens [*Vera and Diebold*, 1994]. But we are still left with a choice between a lithologic boundary and a porosity boundary. We note that in either case the only mechanism for thickening Layer 2A is lava flows overflowing the axial summit graben.

To investigate the 2A/2B transition, we have plotted the porosity structure for the uppermost part of Layer 2B in Figure 2.8. It shows the aspect ratio distribution at a depth of 82 m in the zero-age crust sampled by Line 0S. This was the only line for which

reasonable shear-wave velocity constraints below Layer 2A could be imposed by the seismic modeling [*Christeson et al.*, 1994].

If the 2A/2B boundary marked an upward propagating alteration front, then the initial aspect ratio distribution below the front should be the same as that above it. In other words, just by sealing cracks (reducing porosity) we should be able to get from Figure 2.5 to Figure 2.8. At intermediate aspect ratios (0.05 to 0.01), however, the deeper distribution (Figure 2.8) shows higher porosity than the shallow structure (Figure 2.5). Further, we should expect almost no change in the population of large aspect ratio cracks, since those take a large volume of alteration material to seal. The pore space distribution for the deeper structure (Figure 2.8), however, indicates a much lower population of cracks at large aspect ratio (0.5 to 0.1) compared to the high population of large aspect ratio cracks present at the seafloor (Figure 2.5). We must conclude that the pore space distribution of the deeper structure, shown in Figure 2.8, cannot be reached simply by sealing up cracks in the seafloor structure, shown in Figure 2.5. The 2A/2B boundary cannot be a mere porosity change.

The major difference between the pore space distribution at the seafloor and that at 82 m depth is the lack of porosity near unit aspect ratio. In other words, the material at the deeper structure has no vesicles. Vesicles are formed in volcanic rocks by gases exolving during rapid decompression [*Batiza and Niu*, 1992]. In dikes, because of the slower cooling and the lack of rapid pressure change, exolved gases are left in irregular voids which may be bounded by crystal faces; instead of the equant porosity of round vesicles, dikes have porosity concentrated at smaller aspect ratio, consistent with the results from our deeper structure model shown in Figure 2.8. In addition, dikes will have thermal contraction cracks, though these will typically have a larger aspect ratio than the extensive fine thin cracks which riddle extrusives. Rather than a bimodal or trimodal aspect ratio

distribution, we might expect dikes to display a broad single peak, precisely what is observed in the distribution illustrated in Figure 2.8. We conclude that the 2A/2B boundary in zero-age crust is a boundary between extrusives and dikes.

2.6.4 Evolution of Layer 2A

In Figure 2.11 we compare the zero-age structure of line 0S with the 120 ka structure of model 120W(b). The most obvious change is the thickening of Layer 2A. As *Christeson et al.* [1994] describe, this thickening is almost certainly caused by lava flows overflowing the axial summit graben. Figure 2.11 also shows a decrease in the porosity of Layer 2A with age. At 120 ka the surface porosity has decreased to about 20% from its zero-age value of about 29%. The surface aspect ratio distribution at 120 ka is shown in Figure 2.10. We see that the major difference between 120 ka and zero-age (Figure 2.5) is the lower porosity at small aspect ratio. Reduction of porosity at small aspect ratio is what is predicted by *Wilkens et al.* [1991] from progressive alteration. The *Wilkens et al.* [1991] model was developed for older crust; for the young crust sampled here the preferential sealing of thin cracks will be complicated by the emplacement of further flows and the thickening of Layer 2A, but Figure 2.11 shows that a crustal aging signal can still be detected.

While the overall porosity decreases slightly with age, a relatively high population of thin cracks persists, as Figure 2.10 shows. Even at 120 ka, Layer 2A must be largely unsealed.
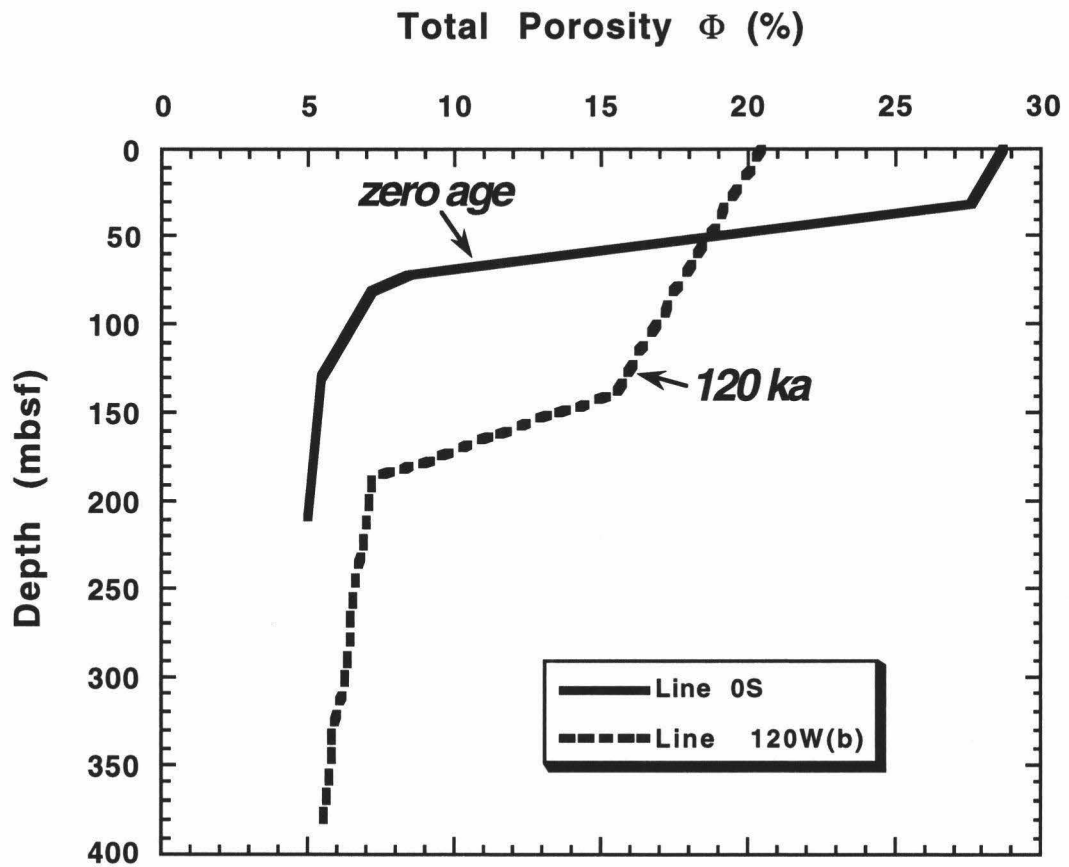
Figure 2.11. Comparison of the porosity structure between zero age crust of line 0S and 120 ka old crust of line 120W (b). The total porosities plotted represent the average obtained after using the extended Kuster - Toksöz (KT+) and the extended Walsh (Walsh+) theories.

2.7 CONCLUSIONS

We have inverted seismic velocity information for porosity as a function of aspect ratio to reach the following conclusions:

1. From zero to 120 ka the surficial porosity of Layer 2A decreases from about 30 to about 20% through the sealing of the narrowest cracks.

2. For zero-age crust the distribution of pore space over aspect ratio is bimodal. The maximum in the distribution occurs for high-aspect-ratio void space (vesicles, inter-pillow voids, breccia), the other peak is at very low aspect ratio (thin cracks and joints). Such bimodal distribution for the porosity structure of young oceanic crust is broadly comparable with the porosity inferred from direct observation of extrusives in the Troodos Ophiolite.

3. The Layer 2A/2B boundary, at least in crust of 120 ka and less, is a lithologic boundary between lava flows and dikes.

It is important to recognize that these findings, and the entire technique of inversion of seismic velocities for the aspect ratio distribution, depend critically on the availability of good shear-wave velocity information. For the EPR seismic experiment the shear-wave velocities were inferred indirectly by seismogram synthesis of hydrophone records and are really only reliable for Line 0S and the top of Layer 2A at Line 120 [*Christeson et al.*, 1994]. Our conclusions must therefore be taken as rather speculative. To confirm these conclusions and to define the structure and evolution of young ocean crust completely will require a series of on-bottom refraction experiments using seismometers rather than the hydrophones so that reliable shear-wave information can be obtained.

2.8. REFERENCES

Batiza, R., and Y. Niu, Petrology and magma chamber processes at the East Pacific Rise ~9°30'N, *J. Geophys. Res.*, *97*, 6779-6797, 1992.

Berge, P. A., Seismic anisotropy and velocity-porosity relationships in the seafloor, Ph.D. dissertation, Univ. of Hawaii, Honolulu, 1991.

Berge, P. A., G. J. Fryer, and R. H. Wilkens, Velocity-porosity relationships in the upper oceanic crust: theoretical considerations, *J. Geophys. Res.*, *97*, 15239-15254, 1992.

Broglia, C., and D. Ellis, Effect of alteration, formation absorption, and standoff on the response of the thermal neutron porosity log in gabbros and basalts: Examples from Deep Sea Drilling Project - Ocean Drilling Program Sites, *J. Geophys. Res.*, *95*, 9171-9188, 1990.

Cheng, C. H., Seismic velocities in porous rocks: direct and inverse problems, Ph.D. thesis, Mass. Inst. of Tech., Cambridge, 1978.

Christensen, N. I., Compressional and shear wave velocities at pressures to 10 kilobars for basalts from the East Pacific Rise, *Geophys. J. R. Astron. Soc.*, *28*, 425-429, 1972.

Christensen, N. I., Ophiolites, seismic velocities and oceanic crustal structure, *Tectonophysics*, *47*, 131-157, 1978.

Christeson, G. L., G. M. Purdy, and G. J. Fryer, Structure of young upper crust at the East Pacific Rise near 9°30'N, *Geophys. Res. Lett.*, *19* (10), 1045-1048, 1992.

Christeson, G. L., G. M. Purdy, and G. J. Fryer, Seismic constraints on shallow crustal emplacement processes at the fast-spreading East Pacific Rise, *J. Geophys. Res.*, *99*, 17957-17966, 1994.

Harding, A. J., G. M. Kent, and J. A. Orcutt, A multichannel seismic investigation of upper crustal structure at 9°N on the East Pacific Rise: Implications for crustal accretion, *J. Geophys. Res.*, *98*, 13925-13944, 1993.

Hashin, Z., and S. Shtrikman, A variational approach to the theory of the elastic behaviour of multiphase materials, *J. Mech. Phys. Solids*, *11*, 127-140, 1963.

Herron, T. J., Lava flow layer - East Pacific Rise, *Geophys. Res. Lett.*, *9*, 17-20, 1982.

Houtz, R., and J. I. Ewing, Upper crustal structure as a function of plate age, *J. Geophys. Res.*, *81*, 2490-2498, 1976.

Koelsch, D. E., G. M. Purdy, and J. E. Broda, A multiple charge deep deployed explosive source for high resolution seismic refraction experiments in the deep ocean, in *Fall MTS Conference*, edited by , pp. , , New Orleans, 1991.

Kuster, G. T., and M. N. Toksöz, Velocity and attenuation of seismic waves in two-phase media, Part I, Theoretical formulations, *Geophysics*, *39*, 587-606, 1974*a*.

Kuster, G. T., and M. N. Toksöz, Velocity and attenuation of seismic waves in two-phase media, Part II, Experimental results, *Geophysics*, *39*, 607-618, 1974*b*.

Ludwig, N. A., J. L. Karsten, R. H. Wilkens, and G. J. Fryer, Geometry and orientation of pore space in oceanic crust: Constraints from the Troodos Ophiolite, *EOS Trans. AGU*, *74* (43), 1993*a*.

Ludwig, R. J., G. J. Fryer, G. L. Christeson, and G. M. Purdy, Porosity in the shallow crust at the East Pacific Rise, *EOS Trans. AGU, 74* (43), 1993*b*.

McClain, J. S., J. A. Orcutt, and M. Burnett, The East Pacific Rise in cross section: a seismic model, *J. Geophys. Res., 90*, 8627-8639, 1985.

Purdy, G. M., New observations of the shallow seismic structure of young oceanic crust, *J. Geophys. Res., 92*, 9351-9362, 1987.

Rohr, K. M. M., B. Milkereit, and C. J. Yorath, Asymmetric deep crustal structure across the Juan de Fuca Ridge, *Geology, 16*, 533-537, 1988.

Shaw, P. R., Age variations of oceanic crust Poisson's ratio: Inversion and a porosity evolution model, *J. Geophys. Res., 99*, 3057-3065, 1994.

Shearer, P. M., Cracked media, Poisson's ratio and the structure of the upper oceanic crust, *Geophys. J. R. Astron. Soc., 92*, 357-362, 1988.

Toomey, D. R., G. M. Purdy, S. C. Solomon, and W. S. D. Wilcock, The three-dimensional seismic velocity structure of the East Pacific Rise near latitude 9°30'N, *Nature, 347*, 639-645, 1990.

Vera, E. E., and J. E. Diebold, Seismic imaging of oceanic Layer 2A between 9°30'N and 10°N on the East Pacific Rise from two-ship wide-aperture profiles, *J. Geophys. Res., 99*, 3031-3041, 1994.

Vera, E. E., J. C. Mutter, P. Buhl, J. A. Orcutt, A. J. Harding, M. E. Kappus, R. S. Detrick, and T. M. Brocher, The structure of 0- to 0.2-m.y.-old oceanic crust at 9°N on the East Pacific Rise from expanded spread profiles, *J. Geophys. Res.*, *95*, 15529-15556, 1990.

Walsh, J. B., New analysis of attenuation in partially melted rock, *J. Geophys. Res.*, *74*, 4333-4337, 1969.

Wilkens, R. H., G. J. Fryer, and J. Karsten, Evolution of porosity and seismic structure of upper oceanic crust: importance of aspect ratios, *J. Geophys. Res.*, *96*, 17981-17995, 1991.

CHAPTER 3

SEISMIC VELOCITY - POROSITY RELATIONSHIP OF SULFIDE, SULFATE, AND BASALT SAMPLES FROM THE TAG HYDROTHERMAL MOUND

3.1 SUMMARY

Physical properties and ultrasonic measurements on 24 minicores recovered at the TAG hydrothermal mound during Ocean Drilling Program Leg 158 provide a unique reference data set for subsurface sulfide, sulfate, and basalt samples from an active sediment-free hydrothermal system. Seismic velocities, densities, porosities, and the distribution of pore shapes are extremely variable within very short distances of the mound, both horizontally and vertically. However, if the sulfide and sulfate samples are classified according to their mineralogy and their location within major internal zones of the mound the measured physical properties exhibit distinct characteristics which are discussed in this paper.

Seismic velocities of the samples were determined by ultrasonic measurements at confining pressures of 5 to 100 MPa. The transducers of the velocimeter generate a compressional wave, propagating along the vertical axis of the minicore in a plane parallel to the seafloor, and two orthogonal shear waves, S1 and S2, so that S2 propagates in the plane parallel to the borehole axis and S1 perpendicular to the borehole axis. This geometry allows for testing of anisotropy effects, which was only observed for massive sulfide

samples recovered in close proximity to the active Black Smoker Complex. V_p/V_s ratios for rock types of the different internal zones are distinctive: high values of 1.9 for massive sulfides near the seafloor, medium values averaging 1.7 for anhydrite-rich samples, and low values of 1.55 for the deeper more silicified samples. Seismic velocities of basalt samples, which were recovered at the edges of the mineralized upflow zone, are relatively low (V_p = 6.1 km/s; V_s = 3.4 km/s) compared to "normal" mid-ocean ridge basalts. Their total porosity is low (~1.5%). This indicates that the reduced velocities are caused by hydrothermal alteration rather than porosity effects.

We present the first-time application of an iterative modeling scheme using rock physics theories that relate seismic velocities to porosity structure on a hand-sample scale. Porosity distribution models were calculated for representative samples of each major lithologic zone within the TAG mound. Microscopic observations on thin sections corresponding to the ultrasonically-measured minicores together with index property measurements, provided constraints on starting models for this non-unique parameter estimation problem. Lacking any other porosity-structure information, these porosity models yield satisfactory results that match both the limited visual observations of pore shapes and the seismic velocity measurements. The results of this research will provide useful constraints on future studies exploring permeability, fluid flow and alteration mechanisms of hydrothermal systems.

3.2 INTRODUCTION

Hydrothermal circulation of seawater is one of the fundamental processes associated with crustal accretion along oceanic spreading centers. Driven by heat from magmatic intrusion and emplacement of new crust, seawater circulates through the

permeable portions of the crust and upper mantle and discharges at the seafloor as both high-temperature (400°C) focused and lower temperature (< ~250°C) diffuse fluid flow. The circulating hydrothermal fluids interact with the oceanic basement in a complex series of seawater-rock reactions that influence the physical properties and composition of the upper crust [e.g. *Alt*, 1995; *Jacobson*, 1992; *Thompson*, 1983]. Another effect of these interactions is the formation of massive sulfide deposits at the seafloor. These represent modern analogues of many ancient ophiolite-based deposits. The similarities between modern volcanic-dominated mid-ocean ridge deposits and ancient deposits allow many direct comparisons, particularly with Troodos-type massive sulfides which are considered to have formed in similar mid-ocean ridge settings [*Herzig et al.*, 1991]. However, while the internal structure of ophiolites can be observed relatively easily through field work on land, the subsurface of active submarine hydrothermal systems is generally not directly accessible.

Ocean Drilling Program Leg 158 provided a unique opportunity for subsurface sampling by drilling a series of holes into a large sediment-free hydrothermally active mound in the TAG hydrothermal field on the eastern side of the median valley of the Mid-Atlantic Ridge. The ridge segment along which the TAG hydrothermal field is located, is about 40 km long, trends north-northeasterly, and is bounded by non-transform discontinuities to the south and north at 25°55'N and 26°17'N respectively [*Purdy et al.*, 1990; *Smith and Cann*, 1992]. Seafloor spreading has been asymmetric over the last 10 ma; half spreading rates are 13 mm/year to the east and 11 mm/year to the west [*McGregor et al.*, 1977]. Based on these present seafloor-spreading rates the active high-temperature field lies on oceanic crust that is at least 100,000 years old about 1.5 km to the east of the bathymetric axis of the rift valley. Although hydrothermal deposits have been found over an area of about 5 km x 5 km, known high-temperature venting is presently confined to the

TAG active mound, strikingly circular in shape, with a diameter of about 200 m and a height of 50 m compared to the surrounding seafloor [*Rona et al.*, 1993; *Rona et al.*, 1986]. The TAG mound is located at a water depth of 3,650 m at 26°08'N and 44°49'W (Figure 3.1).

This paper will concentrate on the subsurface physical structure of the predominantly sulfide-rich rocks drilled at the TAG hydrothermal system as well as the underlying basement rocks recovered in the deeper hole sections of Site 957. Mineralization of ocean crust occurs where metals, leached from large volumes of altered crust at depth, are concentrated at or near the surface by hydrothermal circulation [*Hannington et al.*, 1995]. Hydrothermal alteration and the formation of secondary minerals influences the seismic velocity, density and porosity structure of oceanic crust [*Wilkens et al.*, 1991]. However, actual velocities and porosities within a hydrothermal system have never been measured. Results from post-cruise ultrasonic measurements on cylindrical samples (minicores) which determined both compressional and shear wave velocities and their implication on the physical properties of the samples, especially on porosity and pore shape distribution are the subject of this paper.

3.3 EXPERIMENTAL TECHNIQUES AND ANALYTICAL METHODS

3.3.1 Sample Preparation

Twenty horizontally oriented and four non-oriented minicores with a diameter of 2.54 cm were drilled perpendicular to the in-situ vertical axis of the core. The minicores were carefully polished either with 240 and/or 600 grit on a glass plate to assure parallel faces and to smooth the contact area. The length of each minicore was checked using a
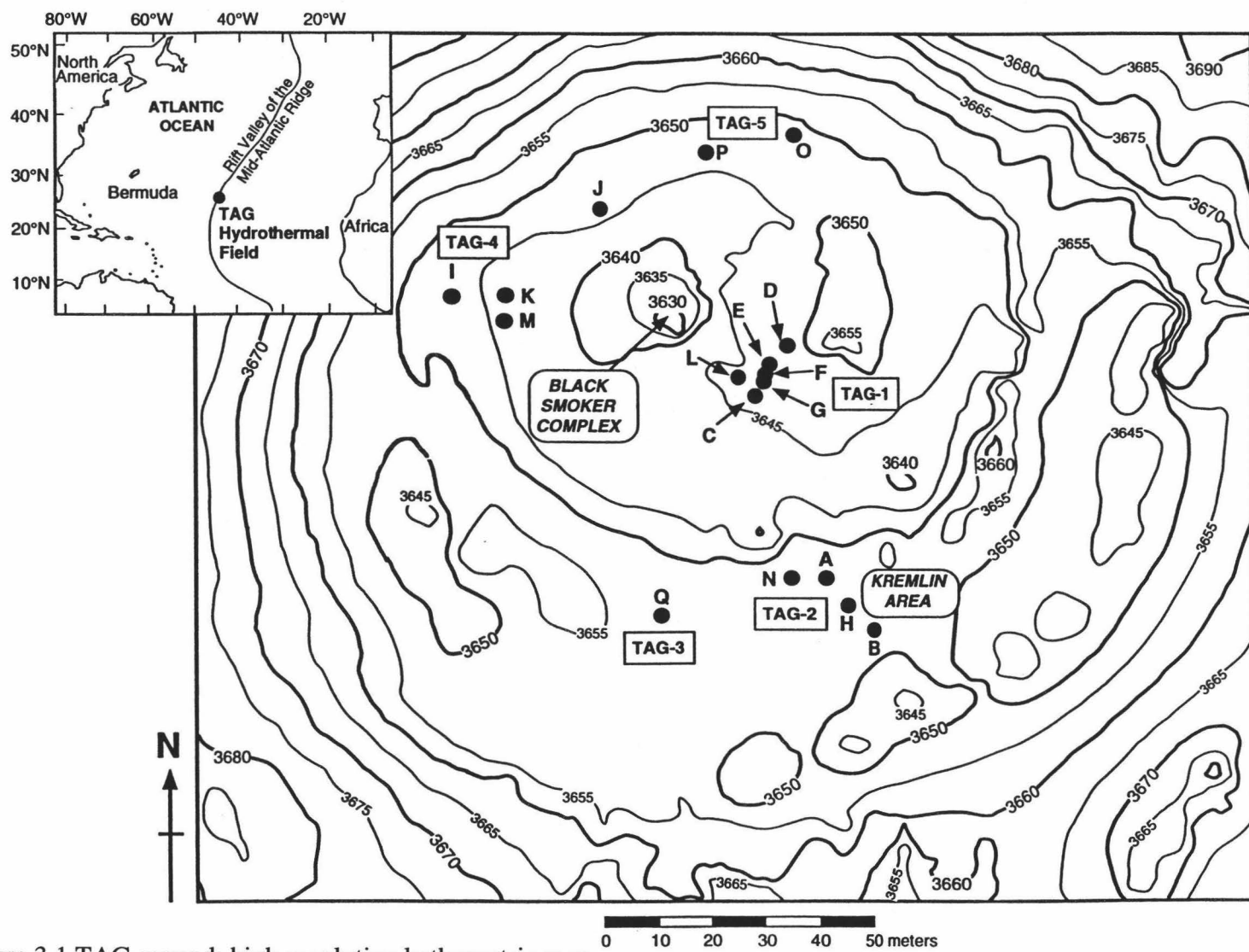
Figure 3.1 TAG mound: high-resolution bathymetric map.

digital caliper micrometer along its circumference, and polishing continued until all length measurements were within 0.02 mm. The grit was later removed by thoroughly cleaning the samples in an ultrasonic bath. In order to saturate the samples and displace air from their pores, the minicores were immersed in seawater and put under a vacuum in a bell jar for 24 to 48 hours prior to measurement. Polished thin sections were made from 11 cut-off sample slabs for petrographic analyses and microscopic analysis of the porosity structure.

3.3.2 Determination of Index Properties

Index properties (bulk density, grain density, bulk water content, porosity) were calculated from measurements of wet and dry sample weights and dry volumes on all minicores. For the wet measurements, samples were saturated in seawater and placed in a vacuum for 24 hours to achieve in-situ wet conditions. After completion of the wet measurements the samples were dried for 24 hours, the sulfide samples at 35° C, the basalts at 60° C. The relatively low drying temperature for the sulfide samples was necessary to prevent changes in mineralogy. Experiments with different drying durations confirmed that even at 35° C, one day was sufficient time to completely dry the samples, owing to their relatively high porosity. All measurements were corrected for salt content assuming a pore fluid salinity of 0.035.

Sample mass was determined aboard the *JOIDES Resolution* to a precision of ±0.01 g using a Scitech electronic balance with a computer averaging system to account for ship motion. The sample mass was counterbalanced by a known mass such that only actual mass differentials of less than 1 g were measured. Volumes were determined using a Quantachrome Penta-Pycnometer, which is an instrument specifically designed to measure the volume and true density of the samples by employing Archimedes' principle of fluid displacement. The displaced fluid is helium, which assures penetration into crevices and

42

interconnected pore spaces approaching 10^{-10} m in dimension. An initial purge time of 3 minutes was used to approach a helium-saturated steady state condition. Thereafter sample volumes were repeatedly measured in 1 minute purge intervals, until two consecutive measurements yielded the specimen volumes within 0.02 cm^3 of each other, the approximate precision of the Quantachrome Penta-Pycnometer. A reference volume was run with each group of samples. The standard was rotated between cells in order to check for systematic error. Additionally all cells of the pycnometer were calibrated daily and the O-rings of the cell lids were changed occasionally to assure continuous accuracy.

The calculation of index properties derived from these measurements is explained in detail in the "Physical Properties" section of the "Explanatory Notes" chapter of the Volume 158 *Initial Reports* [*Humphris et al.*, 1996]. Index properties for the 24 minicores that were used for the ultrasonic measurements are presented in Table 3.1.

3.3.3 Porosity Constraints

During the preparation of the minicores a cut-off slab was kept whenever feasible to further examine the microstructure of the sample. Polished thin sections were made from 10 such core-end billets for petrographic analysis and microscopic examination of the porosity structure. These analyses were used to refine visual observations of the porosity structure for the different rock types and to document textural relationships and mineralogy in greater detail. A summary of the results is presented in Table 3.2 along with the total porosity Φ determined from the index properties measurements. This study provided necessary constraints and starting models for the porosity modeling discussed later in Chapter 3.7.

Table 3.1. Index properties of the 24 ultrasonically-measured minicores collected during ODP Leg 158 at the TAG hydrothermal mound.

Sample (Core-Sec, Int)	Depth (mbsf)	Bulk Density (g/cm^3)	Grain Density (g/cm^3)	Total Porosity (%)	Rock Type
TAG-1 *(East of BSC)*					
Hole 158-957 C					
7N-2, 8-10 cm	20.93	3.35	3.62	10.49	Nod. silic. pyrite-anhydrite breccia
7N-2, 114-116 cm	21.99	3.40	3.82	15.22	anhydrite vein
7N-3, 15-17 cm	22.50	2.79	2.98	9.62	anhydrite vein
11N-3, 118-120 cm	34.79	3.42	3.52	3.90	pyrite-silica breccia
15N-1, 115-117 cm	43.35	3.58	3.67	3.59	silicified wallrock breccia
16N-1, 35-37 cm	46.55	3.21	3.33	5.12	nodular pyrite-silica breccia
Hole 158-957 E					
8R-1, 10-12 cm	72.90	3.30	3.46	6.48	silicified wallrock breccia
15R-1, 30-32 cm	106.80	3.49	3.62	4.89	chloritized basalt breccia
Hole 158-957 F					
1N-1, 62-64 cm	1.62	3.57	3.83	9.28	massive pyrite breccia
1N-1, 71-73cm	1.71	3.68	3.80	4.48	massive pyrite breccia
Hole 158-957 G					
3N-1, 12-14 cm	21.12	4.10	4.40	9.14	mass. pyrite-anhydrite breccia
TAG-2 *(Kremlin Area)*					
Hole 158-957H					
5N-1, 4-6 cm	26.74	4.62	4.96	8.58	massive granular pyrite
5N-2, 29-31 cm	27.89	4.33	4.69	9.92	silicified wallrock breccia
Hole 158-957 N					
1W-1, 62-64 cm	0.62	3.45	3.64	7.36	nodular pyrite-silica breccia
TAG-4 *(West of BSC)*					
Hole 158-957 M					
9R-1, 61-63 cm	42.91	2.88	2.90	1.17	altered basalt
10R-1, 39-41 cm	46.59	2.88	2.91	1.45	altered basalt
10R-1, 47-49 cm	46.67	2.87	2.90	1.70	altered basalt
TAG-5 *(North of BSC)*					
Hole 158-957 O					
2R-1, 34-36 cm	8.24	3.94	4.27	10.22	nodular pyrite breccia
4R-1, 19-21 cm	16.09	3.71	3.93	7.69	pyrite-anhydrite breccia
4R-1, 29-31 cm	16.19	4.19	4.46	7.84	nod. pyrite-anhydrite breccia
Hole 158-957 P					
1R-1, 49-51 cm	0.49	3.56	4.04	15.95	pyrite-anhydrite breccia
6R-1, 11-13 cm	26.61	4.23	4.56	9.29	nodular pyrite breccia
9R-1, 4-6 cm	40.14	3.27	3.39	4.95	nodular pyrite-silica breccia
12R-2, 67-69 cm	56.31	4.31	4.43	3.42	pyrite-silica breccia

Table 3.2. Detailed porosity structure and mineralogical composition, determined by visual and microscopic observations.

Sample (Core-Sec, Int)	Depth (mbsf)	Rock Type	Observed Porosity Structure (TS=Thin Section, V=Visual)	Major Sulfide Mineralogy					Comments	Total Porosity (%)
				pyrite	chalco-pyrite	anhydrite	quartz	clays		
TAG-1 *(East of BSC)*										
Hole 158-957 C										
7N-2, 8-10 cm	20.93	nod. silic. pyrite-anhydrite breccia	TS: high porosity, many thin cracks, some vesicular	40%	10%	40%	10%		cracks adjacent to massive pyrite clasts	10.49
7N-2, 114-116 cm	21.99	anhydrite vein	V: high porosity, large spherical pore spaces, thin cracks and veins			75%	25%		large anhydrite clasts, chimney fragments	15.22
7N-3, 15-17 cm	22.50	anhydrite vein	TS: high porosity, large fluid inclusions, large vapor bubbles	1%	4%	95%			pure anhydrite with cavity filling	9.62
11N-3, 118-120 cm	34.79	pyrite-silica breccia	V: low porosity, few cracks	15%		5%	60%		highly silicified	3.90
15N-1, 115-117 cm	43.35	silicified wallrock breccia	TS: low porosity, irregular void spaces in the order of 100 μm, veins	40%			50%	10%	many pyrite clasts are fractured	3.59
16N-1, 35-37 cm	46.55	nodular pyrite-silica breccia	TS: intermediate porosity, mainly cracks and cavities	25%			65%		pyrite nodules are surrounded by cavities and cracks	5.12
Hole 158-957 E										
8R-1, 10-12 cm	72.90	silicified wallrock breccia	V: low porosity, mostly vesicular	30%			70%		angular altered basalt in pyrite-silica matrix	6.48
15R-1, 30-32 cm	106.80	chloritized basalt breccia	V: low porosity, some thin cracks	40%			55%	3%	sulfides and quartz occur mainly in veins	4.89
Hole 158-957 F										
1N-1, 62-64 cm	1.62	massive pyrite breccia	TS/V: high porosity	85%	5%	10%			damaged thin section, big pyrite clasts	9.28
1N-1, 71-73cm	1.71	massive pyrite breccia	V: intermediate porosity	85%	5%	10%			big pyrite clasts, small chalcopyrite clasts	4.48
Hole 158-957 G										
3N-1, 12-14 cm	21.12	massive pyrite-anhydrite breccia	V: low porosity, mostly vesicular	80%		15%			clasts of pyrite-silica in granular pyrite matrix	9.14
TAG-2 *(Kremlin Area)*										
Hole 158-957 H										
5N-1, 4-6 cm	26.74	massive granular pyrite	V: low porosity, mostly vesicular adjacent to nodular pyrite clasts	95%					big clasts of nodular pyrite	8.58
5N-2, 29-31 cm	27.89	silicified wallrock breccia	TS: intermediate porosity, some thin cracks, near quartz veins	60%		2%	30%	5%	most open spaces fill with quartz	9.92

45

Table 3.2. (Continued) Detailed porosity structure and mineralogical composition, determined by visual and microscopic observations.

Sample (Core-Sec, Int)	Depth (mbsf)	Rock Type	Observed Porosity Structure (TS=Thin Section, V=Visual)	pyrite	chalco-pyrite	anhydrite	quartz	clays	Comments	Total Porosity (%)
TAG-2 cont. (Kremlin Area)										
Hole 158-957 N										
1W-1, 62-64 cm	0.62	nodular pyrite-silica breccia	V: low porosity	30%		2%	65%		many quartz veins	7.36
TAG-4 (West of BSC)										
Hole 158-957 M										
9R-1, 61-63 cm	42.91	altered basalt	TS: very low porosity (≈1%), mostly vesicles and other circular voids (size ≈0.09 - 0.3 mm)						few cracks and veins	1.17
10R-1, 39-41 cm	46.59	altered basalt	TS: very low porosity (≈1-2%), mostly vesicles and other circular voids (size ≈0.1 mm), some elongated voids (≈0.4 mm)						veins, some hair thin cracks (size< 0.01mm)	1.45
10R-1, 47-49 cm	46.67	altered basalt	V: same as other 2 basalt samples						same as other 2 basalt samples	1.70
TAG-5 (North of BSC)										
Hole 158-957 O										
2R-1, 34-36 cm	8.24	nodular pyrite breccia	TS: high porosity, many cracks adjacent to anhydrite veins	50%	10%	30%	10%		very porous, anhydrite only partially fills open spaces	10.22
4R-1, 19-21 cm	16.09	pyrite-anhydrite breccia	V: low porosity	60%	5%	35%			some cracks within anhydrite veins	7.69
4R-1, 29-31 cm	16.19	nodular pyrite-anhydrite breccia	V: low porosity	75%	3%	20%			big pyrite clasts cut by anhydrite veins	7.84
Hole 158-957 P										
1R-1, 49-51 cm	0.49	pyrite-anhydrite breccia	TS: high porosity, elongated cracks, unfilled voids near anhydrite veins	60%	10%	30%			void spaces concentrated near veins	15.95
6R-1, 11-13 cm	26.61	nodular pyrite breccia	V: intermediate porosity, mostly vesicular adjacent to pyrite clasts	90%		9%			massive granular pyrite	9.29
9R-1, 4-6 cm	40.14	nodular pyrite-silica breccia	V: low porosity, few circular voids, some thin cracks	30%			70%		nodular pyrite clasts in silica matrix	4.95
12R-2, 67-69 cm	56.31	pyrite-silica breccia	V: low porosity, few circular voids, very few thin cracks	35%			60%	5%	wallrock clasts extensively replaced by silica and pyrite	3.42

46

3.3.4 Ultrasonic Measurements

Seismic velocities were measured at the Petrophysics Laboratory of the Rosenstiel School of Marine and Atmospheric Science (RSMAS), University of Miami. Velocities were measured with a 100 MPa (1 kbar) velocimeter at hydrostatic pressures ranging from 5 to 100 MPa and a constant pore pressure of 2 MPa (Figure 3.2). A unique feature of the system's 1 MHz transducer configuration is that two orthogonal shear waves (S1 and S2) are propagated through the sample along with a single compressional wave. The minicores were aligned so that the S2 wave propagated in the plane defined by the orientation marks of the sample, whereas the S1 wave propagated in a plane oriented 90° from the S2 plane (Figure 3.3). The precision of both V_p and V_s measurements is approximately 1% to 2%. The ultrasonic data are presented in Table 3.3.

The seismic velocities were measured during increasing pressure cycles in 5 MPa increments between 5 and 20 MPa and in 10 MPa increments between 20 and 100 MPa. One exception was made for measurements on an almost pure anhydrite sample (Sample 158-957C- 7N-3, 15-17 cm, denoted with an asterisk * in Table 3.3). The delicate nature of the anhydrite in a water-saturated state demanded quick measurements. The measurements were made in 10 MPa increments starting at a confining pressure of 20 MPa and increasing up to 100 MPa. Thereafter the pressure was slowly reduced and the remaining ultrasonic measurements were performed at 15, 10, and 5 MPa respectively.

3.4 SAMPLE DESCRIPTIONS

Samples are described according to the sulfide classification scheme developed aboard the ship [*Humphris et al.*, 1996], unless the mineralogy of the section interval,
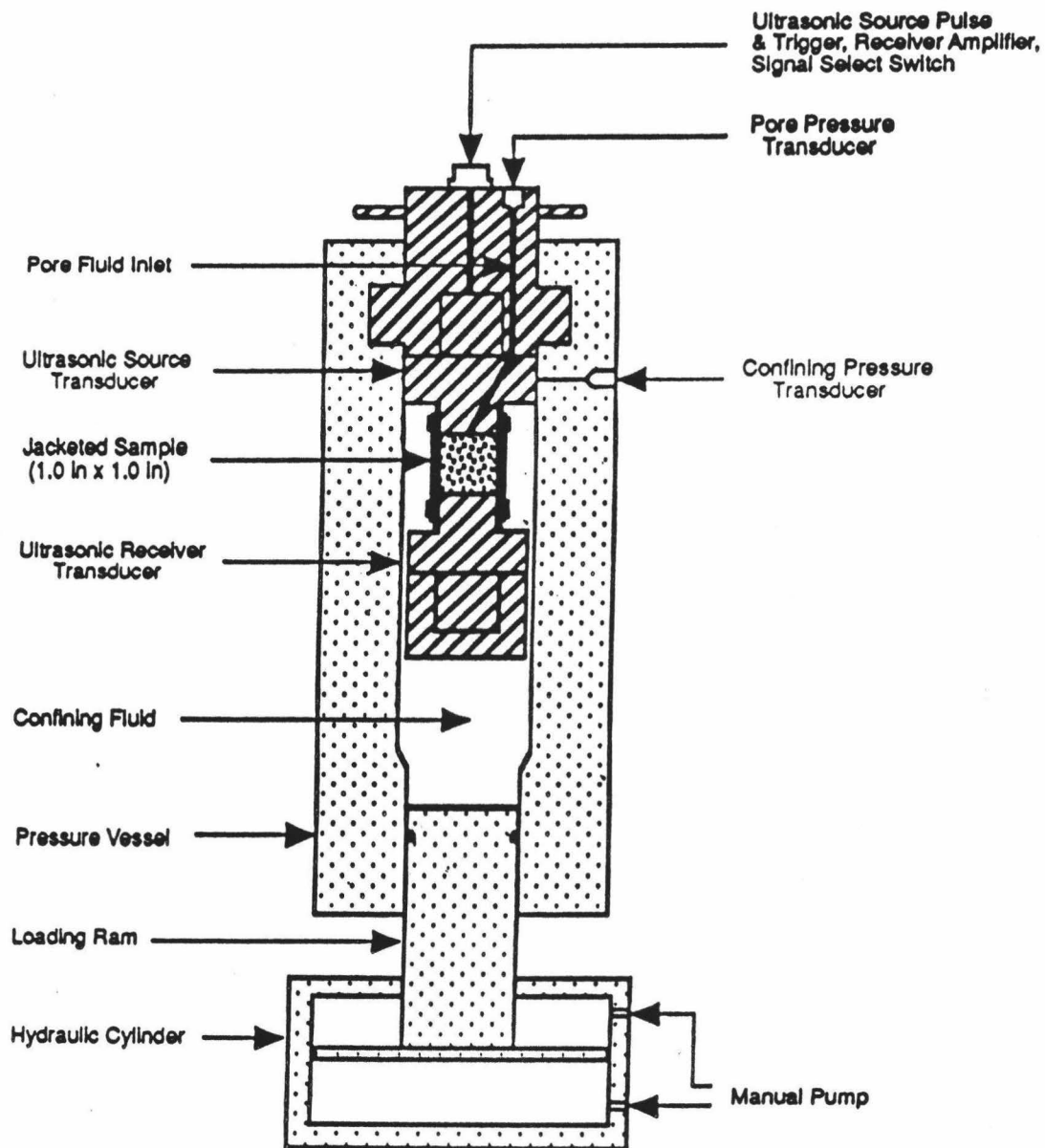
Figure 3.2. Schematic diagram of the sample assembly and pressure vessel for the 100 MPa velocimeter located at the Petrophysics Laboratory of the Rosenstiel School of Marine and Atmospheric Science (RSMAS), University of Miami.
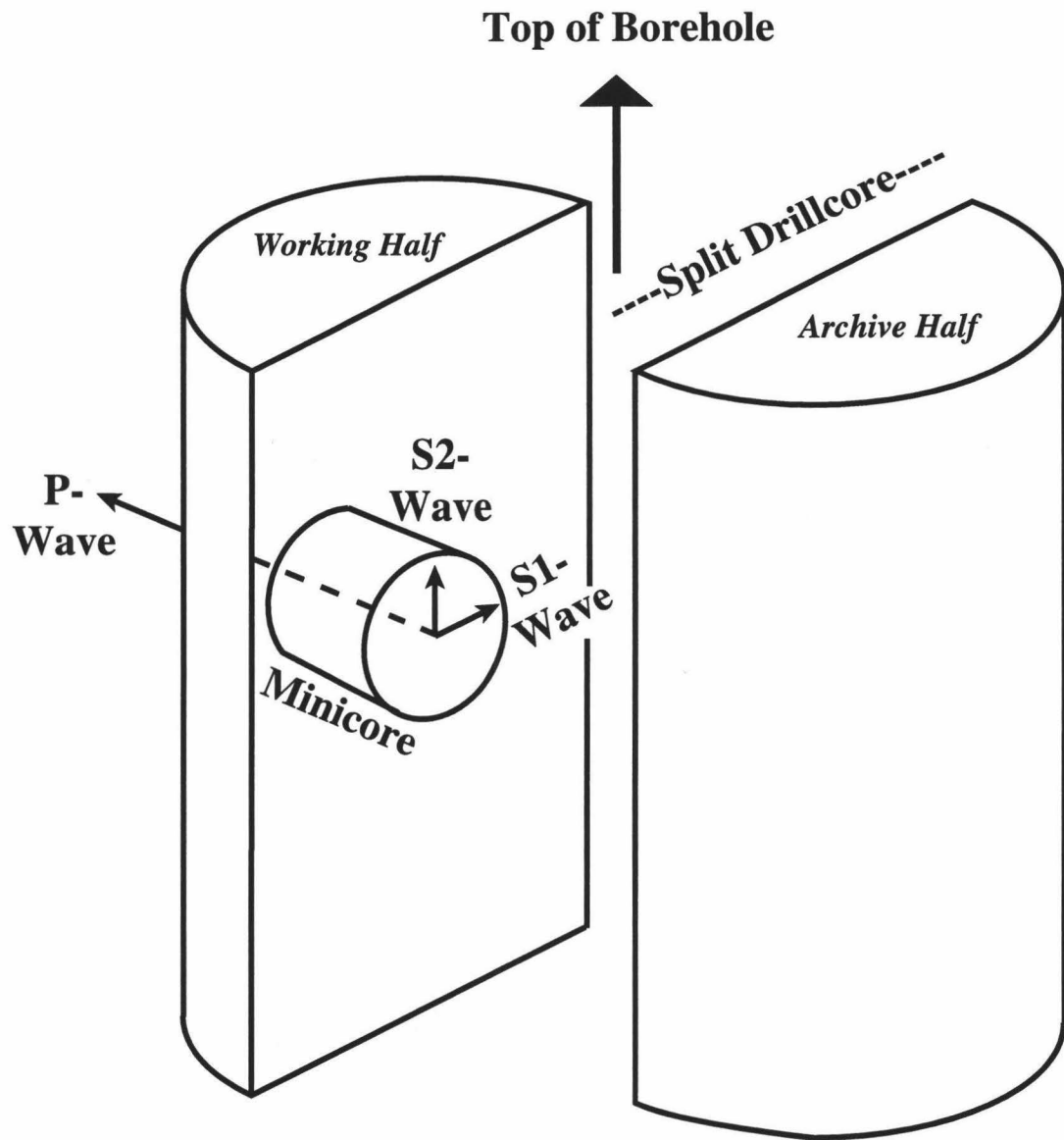
Figure 3.3 Geometry of ultrasonic measurements on minicore samples, extracted from the working half of the split drillcore: A compressional wave propagates along the vertical axis of the minicore in a plane parallel to the seafloor. Two orthogonal shear waves, S1 and S2, propagate through the sample so that S2 propagates in the plane parallel to the borehole axis and S1 perpendicular to the borehole axis.

49

Table 3.3. Compressional-wave and shear-wave velocities for sulfide, sulfate, and basalt samples from the TAG active mound measured ultrasonically at increasing confining pressures.

| Sample (Core-Sec, Int)	Depth (mbsf)	Rock Type	Velocity (km/s)	Pressure (MPa)												Oriented Sample
				5	10	15	20	30	40	50	60	70	80	90	100	
TAG-1 *(East of BSC)*																
Hole 158-957 C																
7N-2, 8-10 cm	20.93	nod. silic. pyrite-anhydrite breccia	V$_P$	4.76	4.85	4.90	5.05	5.09	5.13	5.15	5.19	5.20	5.25	5.26	5.30	Yes
			V$_{S1}$	2.62	2.66	2.75	2.80	2.88	2.94	3.02	3.08	3.11	3.13	3.14	3.16	
			V$_{S2}$	2.71	2.72	2.77	2.82	2.97	3.03	3.10	3.12	3.15	3.16	3.17	3.18	
7N-2, 114-116 cm	21.99	anhydrite vein	V$_P$	3.94	3.92		4.17	4.49	4.52	4.56	4.58	4.60	4.66	4.72	4.80	Yes
			V$_{S1}$	2.61	3.05		3.11	2.39	2.40	2.40	2.42	2.45	2.48	2.51	2.55	
			V$_{S2}$	2.55	4.79		3.13	2.34	2.36	2.41	2.43	2.46	2.48	2.52	2.56	
7N-3, 15-17 cm	22.50	anhydrite vein	V$_P$	3.82*	3.86*	3.90*	3.79	3.93	4.06	4.13	4.21	4.27	4.31	4.39	4.42	Yes
			V$_{S1}$	1.87*	2.09*	2.14*	2.10	2.21	2.31	2.34	2.43	2.48	2.50	2.53	2.55	
			V$_{S2}$	1.96*	2.05*	2.11*	2.10	2.22	2.31	2.37	2.39	2.44	2.49	2.49	2.51	
11N-3, 118-120 cm	34.79	pyrite-silica breccia	V$_P$	5.16	5.23	5.29	5.31	5.36	5.40	5.42	5.44	5.46	5.49	5.51	5.52	Yes
			V$_{S1}$	3.12	3.16	3.20	3.24	3.28	3.32	3.35	3.38	3.40	3.41	3.42	3.43	
			V$_{S2}$	3.16	3.21	3.26	3.31	3.35	3.39	3.40	3.42	3.44	3.45	3.47	3.48	
15N-1, 115-117 cm	43.35	silicified wallrock breccia	V$_P$	5.16	5.23	5.38	5.40	5.45	5.53	5.56	5.60	5.63	5.66	5.70	5.72	Yes
			V$_{S1}$	2.94	3.02	3.11	3.18	3.25	3.30	3.35	3.41	3.43	3.45	3.47	3.50	
			V$_{S2}$	2.80	2.85	3.03	3.08	3.25	3.34	3.40	3.45	3.49	3.51	3.54	3.55	
16N-1, 35-37 cm	46.55	nodular pyrite-silica breccia	V$_P$	5.21	5.26	5.27	5.29	5.33	5.41	5.45	5.48	5.51	5.53	5.56	5.58	Yes
			V$_{S1}$	3.03	3.15	3.20	3.31	3.40	3.46	3.48	3.50	3.52	3.55	3.57	3.58	
			V$_{S2}$	3.11	3.16	3.33	3.34	3.47	3.47	3.48	3.51	3.53	3.55	3.57	3.58	
Hole 158-957 E																
8R-1, 10-12 cm	72.90	silicified wallrock breccia	V$_P$	5.37	5.39	5.45	5.50	5.56	5.60	5.62	5.63	5.69	5.69	5.71	5.72	No
			V$_{S1}$	3.21	3.35	3.38	3.41	3.48	3.49	3.52	3.53	3.56	3.57	3.59	3.61	
			V$_{S2}$	3.17	3.36	3.38	3.39	3.49	3.53	3.54	3.58	3.61	3.62	3.63	3.65	
15R-1, 30-32 cm	106.80	chloritized basalt breccia	V$_P$	5.29	5.38	5.50	5.53	5.61	5.68	5.73	5.78	5.81	5.83	5.85	5.88	No
			V$_{S1}$	3.20	3.33	3.42	3.46	3.52	3.58	3.62	3.66	3.68	3.72	3.74	3.77	
			V$_{S2}$	3.29	3.34	3.42	3.47	3.53	3.59	3.66	3.69	3.70	3.73	3.75	3.78	

Table 3.3. (Continued) Compressional-wave and shear-wave velocities for sulfide, sulfate, and basalt samples from the TAG active mound measured ultrasonically at increasing confining pressures.

Sample (Core-Sec, Int)	Depth (mbsf)	Rock Type	Velocity (km/s)	Pressure (MPa)												Oriented Sample
				5	10	15	20	30	40	50	60	70	80	90	100	
TAG-1 cont. *(East of BSC)*																
Hole 158-957 F																
1N-1, 62-64 cm	1.62	massive pyrite breccia	V_P	5.17	5.18	5.21	5.22	5.23	5.25	5.28	5.30	5.25	5.26	5.27	5.30	Yes
			V_{S1}	2.75	2.75	2.76	2.77	2.77	2.80	2.80	2.83	2.83	2.85	2.86	2.88	
			V_{S2}	2.73	2.73	2.75	2.76	2.78	2.80	2.82	2.82	2.82	2.83	2.83	2.84	
1N-1, 71-73cm	1.71	massive pyrite breccia	V_P	5.63	5.58	5.67	5.68	5.70	5.71	5.73	5.74	5.76	5.77	5.77	5.79	Yes
			V_{S1}	3.21	3.21	3.25	3.33	3.34	3.34	3.35	3.35	3.36	3.35	3.26	3.27	
			V_{S2}	3.12	3.03	3.10	3.11	2.98	3.01	3.07	3.07	3.07	3.06	3.07	3.07	
Hole 158-957 G																
3N-1, 12-14 cm	21.12	massive pyrite-anhydrite breccia	V_P	6.01	6.05	6.10	6.12	6.15	6.17	6.18	6.20	6.21	6.23	6.25	6.26	Yes
			V_{S1}	3.60	3.66	3.72	3.73	3.76	3.79	3.80	3.81	3.81	3.82	3.82	3.82	
			V_{S2}	3.63	3.75	3.72	3.77	3.78	3.80	3.81	3.81	3.82	3.83	3.83	3.85	
TAG-2 *(Kremlin Area)*																
Hole 158-957 H																
5N-1, 4-6 cm	26.74	massive granular pyrite	V_P	6.66	6.68	6.68	6.68	6.70	6.72	6.74	6.74	6.74	6.76	6.78	6.80	Yes
			V_{S1}	4.05	4.09	4.11	4.14	4.16	4.18	4.19	4.20	4.21	4.21	4.22	4.23	
			V_{S2}	4.04	4.12	4.13	4.13	4.15	4.16	4.17	4.18	4.19	4.19	4.20	4.22	
5N-2, 29-31 cm	27.89	silicified wallrock breccia	V_P	6.32	6.39	6.47	6.54	6.64	6.68	6.76	6.78	6.80	6.82	6.84	6.86	Yes
			V_{S1}	3.43	3.44	3.60	3.67	4.10	4.14	4.15	4.16	4.16	4.17	4.19	4.20	
			V_{S2}	3.54	3.74	3.78	3.92	4.10	4.13	4.14	4.14	4.15	4.16	4.17	4.18	
Hole 158-957 N																
1W-1, 62-64 cm	0.62	nodular pyrite-silica breccia	V_P	5.25	5.26	5.31	5.35	5.39	5.46	5.49	5.50	5.52	5.53	5.55	5.57	No
			V_{S1}	2.98	3.11	3.25	3.29	3.37	3.40	3.40	3.43	3.45	3.45	3.46	3.47	
			V_{S2}	2.76	3.02	3.19	3.24	3.37	3.44	3.48	3.50	3.51	3.51	3.52	3.53	

Table 3.3. (Continued) Compressional-wave and shear-wave velocities for sulfide, sulfate, and basalt samples from the TAG active mound measured ultrasonically at increasing confining pressures.

Sample (Core-Sec, Int)	Depth (mbsf)	Rock Type	Velocity (km/s)	Pressure (MPa)												Oriented Sample
				5	10	15	20	30	40	50	60	70	80	90	100	
TAG-4 *(West of BSC)*																
Hole 158-957 M																
9R-1, 61-63 cm	42.91	altered basalt	V_P	5.89	5.92	5.93	5.94	5.96	5.99	6.00	6.01	6.03	6.04	6.06	6.07	Yes
			V_{S1}	3.21	3.24	3.25	3.26	3.26	3.27	3.29	3.30	3.33	3.33	3.34	3.35	
			V_{S2}	2.88	3.16	3.17	3.18	3.24	3.25	3.28	3.31	3.34	3.34	3.36	3.36	
10R-1, 39-41 cm	46.59	altered basalt	V_P	5.98	5.99	6.01	6.01	6.02	6.04	6.04	6.06	6.06	6.06	6.06	6.06	Yes
			V_{S1}	3.32	3.35	3.39	3.39	3.38	3.38	3.38	3.39	3.39	3.40	3.40	3.41	
			V_{S2}	3.37	3.37	3.38	3.38	3.37	3.38	3.38	3.39	3.39	3.40	3.40	3.40	
10R-1, 47-49 cm	46.67	altered basalt	V_P	5.89	5.91	5.95	5.97	5.97	5.97	5.97	5.99	5.99	5.99	5.99	6.00	No
			V_{S1}	3.32	3.32	3.39	3.40	3.41	3.41	3.41	3.41	3.41	3.41	3.41	3.41	
			V_{S2}	3.31	3.32	3.46	3.46	3.46	3.41	3.42	3.43	3.43	3.43	3.42	3.43	
TAG-5 *(North of BSC)*																
Hole 158-957 O																
2R-1, 34-36 cm	8.24	nodular pyrite breccia	V_P	5.28	5.39	5.46	5.49	5.59	5.61	5.62	5.67	5.67	5.69	5.73	5.74	Yes
			V_{S1}	2.80	2.86	2.99	3.07	3.23	3.25	3.29	3.32	3.34	3.36	3.36	3.38	
			V_{S2}	2.94	2.99	3.13	3.21	3.28	3.29	3.32	3.34	3.36	3.37	3.38	3.39	
4R-1, 19-21 cm	16.09	pyrite-anhydrite breccia	V_P	5.64	5.85	5.96	5.97	6.06	6.12	6.13	6.15	6.16	6.18	6.19	6.21	Yes
			V_{S1}	2.95	3.10	3.24	3.24	3.31	3.37	3.40	3.45	3.48	3.50	3.54	3.55	
			V_{S2}	2.75	2.89	3.03	3.05	3.09	3.10	3.30	3.36	3.40	3.43	3.45	3.47	
4R-1, 29-31 cm	16.19	nodular pyrite-anhydrite breccia	V_P	5.74	5.78	5.81	5.84	5.88	5.94	5.97	5.98	6.01	6.03	6.06	6.07	Yes
			V_{S1}	3.18	3.21	3.26	3.29	3.33	3.38	3.39	3.41	3.42	3.44	3.47	3.51	
			V_{S2}	2.99	3.08	3.16	3.27	3.27	3.34	3.42	3.44	3.47	3.49	3.50	3.53	

Table 3.3. (Continued) Compressional-wave and shear-wave velocities for sulfide, sulfate, and basalt samples from the TAG active mound measured ultrasonically at increasing confining pressures.

Sample (Core-Sec, Int)	Depth (mbsf)	Rock Type	Velocity (km/s)	Pressure (MPa)												Oriented Sample
				5	10	15	20	30	40	50	60	70	80	90	100	
TAG-5 cont. *(North of BSC)*																
Hole 158-957 P																
1R-1, 49-51 cm	0.49	pyrite-anhydrite breccia	V_P	4.69	4.77	4.78	4.79	4.81	4.85	4.88	4.90	4.91	4.93	4.96	4.98	Yes
			V_{S1}	2.53	2.62	2.66	2.69	2.72	2.74	2.76	2.77	2.77	2.78	2.78	2.79	
			V_{S2}	2.54	2.54	2.59	2.61	2.68	2.70	2.72	2.73	2.74	2.74	2.75	2.76	
6R-1, 11-13 cm	26.61	nodular pyrite breccia	V_P	5.74	5.80	5.84	5.92	5.96	5.99	6.02	6.04	6.06	6.08	6.10	6.13	Yes
			V_{S1}	3.36	3.45	3.52	3.55	3.59	3.64	3.68	3.71	3.72	3.74	3.74	3.76	
			V_{S2}	3.43	3.46	3.50	3.51	3.56	3.58	3.59	3.61	3.63	3.68	3.68	3.70	
9R-1, 4-6 cm	40.14	nodular pyrite-silica breccia	V_P	5.62	5.66	5.69	5.70	5.74	5.77	5.78	5.78	5.80	5.81	5.82	5.84	Yes
			V_{S1}	3.02	3.63	3.71	3.75	3.75	3.76	3.76	3.76	3.77	3.77	3.78	3.79	
			V_{S2}	3.06	3.56	3.65	3.67	3.71	3.72	3.74	3.74	3.75	3.76	3.76	3.77	
12R-2, 67-69 cm	56.31	pyrite-silica breccia	V_P	6.52	6.61	6.63	6.67	6.69	6.71	6.72	6.74	6.74	6.74	6.76	6.76	Yes
			V_{S1}	4.04	4.07	4.07	4.09	4.12	4.15	4.15	4.16	4.17	4.18	4.18	4.19	
			V_{S2}	4.13	4.10	4.13	4.14	4.18	4.19	4.20	4.21	4.22	4.22	4.22	4.23	

where the minicore sample was extracted from the core, is distinctively different from the surrounding structure described in the initial report's sulfide log.

One of the most striking features from the TAG mound is the dominance of breccias throughout the mound and in the upper parts of the underlying upflow zone. Based on the overall internal structure of the mound and the upflow zone, four major zones can be distinguished, not all of which may be present in one section [*Humphris et al.*, 1995].

Zone 1 consists of massive sulfides reflecting the formation of new hydrothermal precipitates (e.g. massive pyrite breccia at TAG-1/Hole 957F: Samples 1N-1, 62-64 cm and 1N-1, 71-73 cm; nodular pyrite-silica breccia at TAG-2/Hole 957N: Sample 1W-1, 62-64 cm; nodular pyrite breccia at TAG-5/Hole 957O: Sample 2R-1, 34-36 cm; Tables 3.1-3.3 and Figure 3.4). This zone is restricted to the upper few meters at each drilling location.

Zone 1 is underlain by an anhydrite-rich Zone 2, identified only in the TAG-1 and TAG-5 areas (e.g. TAG-1/Hole 957C: Samples 7N-2, 114-116 cm and 7N-3, 15-17 cm, Hole 957G: Sample: 3N-1, 12-14 cm; TAG-5/Hole 957O: Samples 4R-1, 19-21 cm and 4R-1, 29-31 cm, Hole 957P: Sample 1R-1, 49-51 cm; Tables 3.1-3.3 and Figure 3.4). Anhydrite veining is extremely well-developed throughout this zone, where composite veins up to 45 cm thick are present. The minicore samples from this zone are very porous and many void spaces of different shapes can be identified visually and microscopically (Table 3.2). Most of the cracks and vesicular pores are concentrated near the anhydrite veins which comprise complex, multi-stage fracture fillings and cavity linings, some of which include disseminated, fine-grained pyrite and chalcopyrite.

Zone 3 consists of intensely silicified and brecciated wallrock which comprises the upflow zone beneath the mound. Pyrite-silica breccias occur in the upper part of this zone and are underlain by silicified wallrock breccias, which are distinguished from the

Figure 3.4. Variations of compressional-wave velocities measured at 100 MPa vs. depth for the 24 minicore samples. The plot symbols correspond to the major internal structure zones of the active TAG mound.

overlying pyrite-silica breccias in that they contain significantly less pyrite ($<$ 50% by volume) and are dominantly clast-supported. Seven of the twenty-four minicore samples analyzed in this study represent Zone 3 (Tables 3.1-3.3 and Figure 3.4). These are: At TAG-1/Hole 957C: Samples 11N-3, 118-120 cm, 15N-1, 115-117 cm, and 16N-1, 35-37 cm; Hole 957E: Sample 8R-1, 10-12 cm. At TAG-2/Hole 957H: Sample 5N-2, 29-31 cm. At TAG-5/Hole 957P: Samples 9R-1, 4-6 cm and 12R-2, 67-69 cm.

Zone 4 starts below about 100 mbsf, where the silicified wallrock breccias grade into a chloritized basalt breccia (e.g. TAG-1/Hole 957E: Sample 15R-1, 30-32 cm; Tables 3.1-3.3 and Figure 3.4). In this zone chloritized and weakly mineralized basalt fragments (1-5 cm in size) are cemented by quartz and pyrite, and are cross-cut by veins of pyrite, quartz, and quartz plus pyrite.

Relatively unaltered pillow basalts were recovered near the edges of the mound at depths of about 25 mbsf at TAG-2 and 45 mbsf at TAG 4 (Hole 957M: Samples 9R-1, 61-63 cm, 10R-1, 39-41 cm, and 10R-1, 47-49 cm; Tables 3.1-3.3). These basalts constrain the lateral extent of intense crustal alteration and mineralized upflow zone to about 80 m.

3.5 GENERAL RESULTS

The compressional-wave velocities (V_p) at a confining pressure of 100 MPa for all twenty-four minicore samples versus depth are shown in Figure 3.4. The four major internal zones of the TAG mound can easily be identified. Although very porous (about 10%, Table 3.1) the massive sulfides of Zone 1 all have relatively high seismic velocities of 5.3 to 5.8 km/s owing to their high content of pyrite. The underlying anhydrite-rich Zone 2 illustrates a large variety in V_p from the almost pure anhydrite Sample 957C-7N-3, 15-17 cm with $V_p = 4.42$ km/s up to a massive pyrite-anhydrite breccia sample (957G-3N-1,

12-14 cm with V_p = 6.26 km/s both at a depth of about 22 mbsf. Zone 3 extends from about 25 mbsf to 100 mbsf. Most samples in this category have compressional-wave velocities of about 5.7 km/s, however two pyrite-rich samples have an extremely high V_p of about 6.8 km/s (Samples 957H-5N-2, 29-31 cm and 957P-12R-2, 67-69 cm). The one sample from Zone 4, a chloritized basalt breccia (Sample 957E-15R-1, 30-32 cm) at a depth of 107 mbsf had a relatively high V_p = 5.88 km/s. In addition two massive sulfide samples shown as massive pyrite breccias are plotted in Figure 3.4 (Samples 957H-5N-1, 4-6 cm and 957P-6R-1, 11-13 cm). They were both recovered at a depth of about 27 mbsf and can not be classified as being representative of any of the four major zones.

Extremely difficult drilling conditions prevented any run of special downhole measurement and logging tools during ODP Leg 158. Therefore, on-board physical properties measurements provide the only geophysical data available so far for rocks from a sediment-free subsurface hydrothermal system. However, shipboard measurements on minicores using the "Hamilton frame" only allow a crude estimate of compressional-wave velocities and they do not represent the in-situ properties of the rocks. The ultrasonic data for the TAG-1 and TAG-5 area are shown in Figures 3.5 and 3.6. They illustrate the improvement achieved over the original shipboard measurements of the same samples. While shipboard P-velocities seem widely scattered, the ultrasonic measurements indicate a general velocity increase with depth. A possible explanation for this trend is the increasing cementation and silicification from sulfides to silicified wallrock breccias with depth observed throughout the mound.

Two samples from TAG-1 were extracted from massive anhydrite veins (Samples 957C-7N-2, 114-116 cm and 957C-7N-3, 15-17 cm). Although shipboard measurements on those samples were unsuccessful and in spite of their instability when seawater-saturated, clear signals were recorded during the ultrasonic measurements at all confining

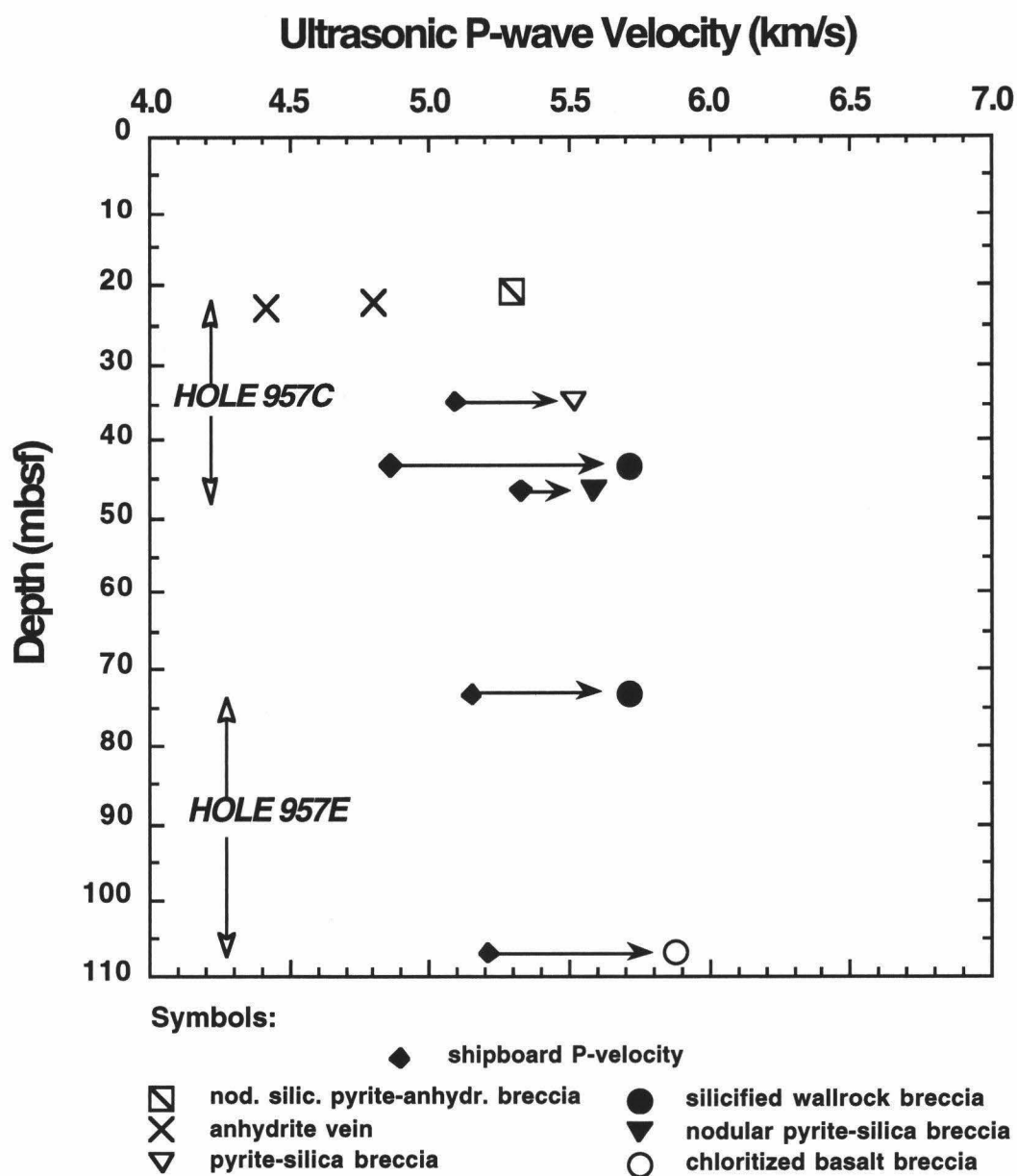# Ultrasonic P-wave Velocity (km/s)

Figure 3.5 Results from ultrasonic compressional-wave velocity measurements at the TAG-1 Area (East Side of the Black Smoker Complex) and comparison with shipboard measurements using the "Hamilton frame".
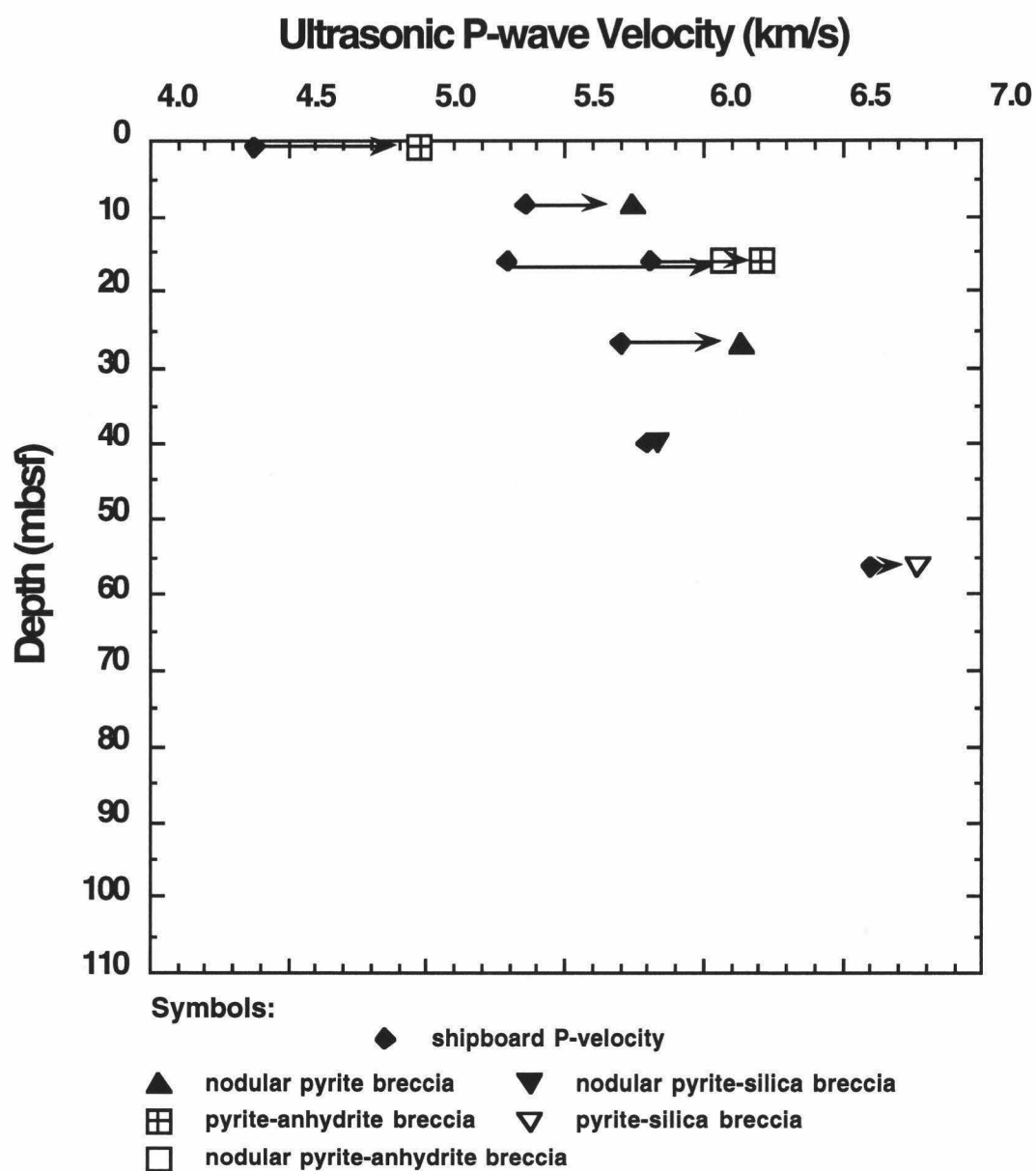
Figure 3.6. Results from ultrasonic compressional-wave velocity measurements at the TAG-5 Area (North Side of the Black Smoker Complex) and comparison with shipboard measurements using the "Hamilton frame".

pressures greater or equal to 20 MPa (Table 3.3). The compressional-wave velocities at 100 MPa were 4.8 and 4.4 km/s respectively (Figure 3.5). These values are considerably higher (22% -33%) than a comparable literature value of 3.6 km/s for a specimen from the Swiss Alps [*Clark*, 1966] perhaps due to traces of massive sulfide clasts present in the TAG samples (Table 3.2).

In Figure 3.7 compressional-wave velocity at 100 MPa is plotted versus bulk density for all samples. As expected, a general trend of increasing velocities with increasing densities can be observed. This trend is especially obvious for the anhydrite-rich samples of Zone 2: The almost pure anhydrite vein sample with a low velocity of 4.4 km/s has also a low bulk density of 2.8 g/cm^3 and a grain density of 3.0 g/cm^3.(The same value of 3.0 g/cm^3 is given for the density of the anhydrite mineral by *Clark* [1966]). The other extreme is a massive pyrite-anhydrite breccia sample with V_p = 6.3 km/s and a bulk density of 4.1 g/cm^3 (Sample 957G-3N-1, 12-14 cm). Not following the same trend are the three altered basalt samples from TAG-4. Their average bulk density is 2.88 g/cm^3 and their average compressional-wave velocity at 100 MPa is 6 km/s. This relationship is later discussed in greater detail.

Compressional-wave velocity at 100 MPa is plotted versus total porosity calculated from index properties measurements for all minicore samples in Figure 3.8. A clear trend can only be determined for the anhydrite-rich rocks of Zone 2, where in general seismic velocity decreases with increasing total porosity. For the other samples the seismic velocity versus total porosity relationship is widely scattered. *Wilkens et al.* [1991] and *Berge et al.* [1992] have shown that the porosity distribution over pore shape is a more useful quantity than total porosity. A more detailed discussion follows in Chapter 3.7.
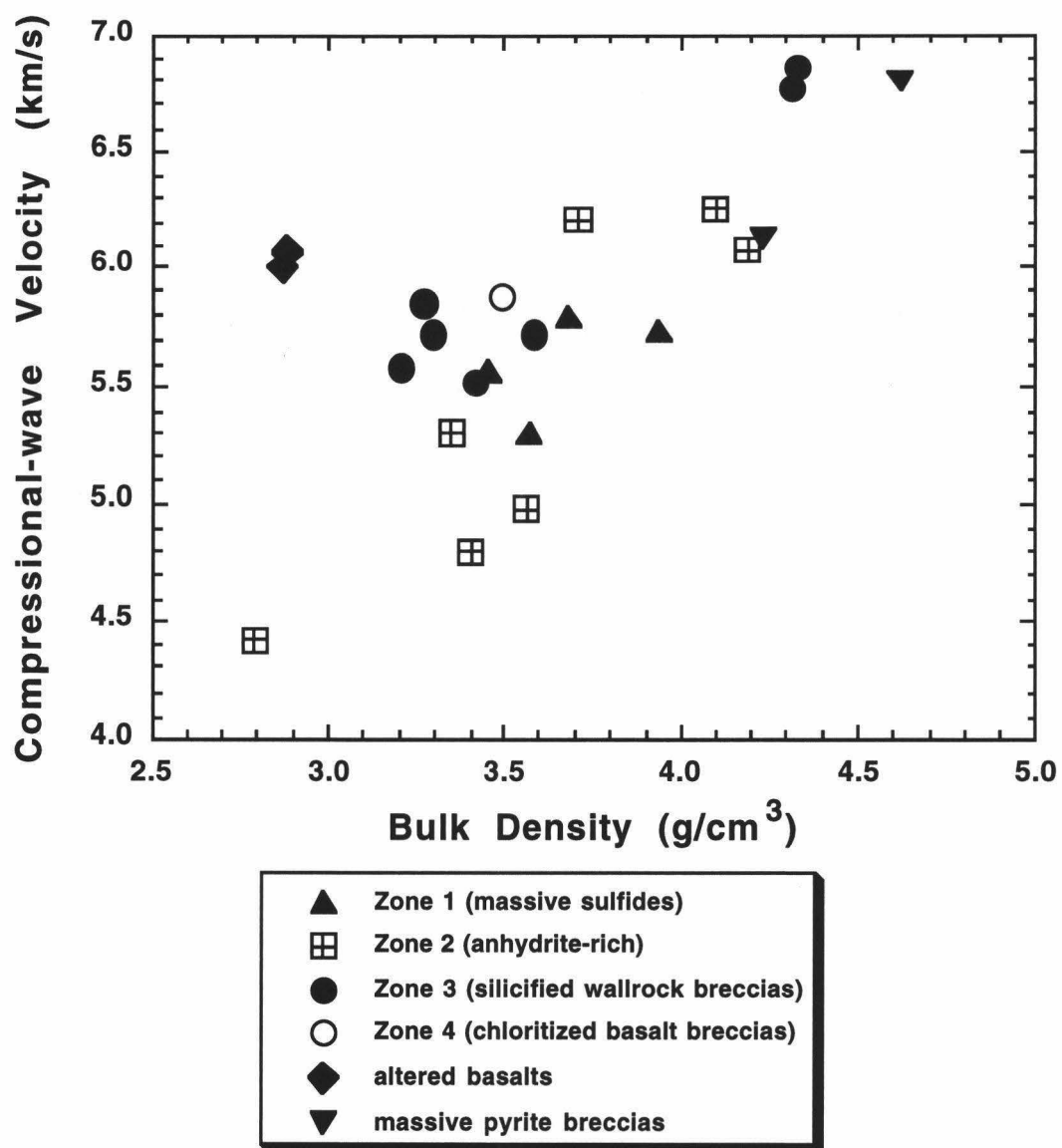
Figure 3.7. Compressional-wave velocity at 100 MPa as a function of bulk density. The plot symbols correspond to the major internal structure zones of the active TAG mound.
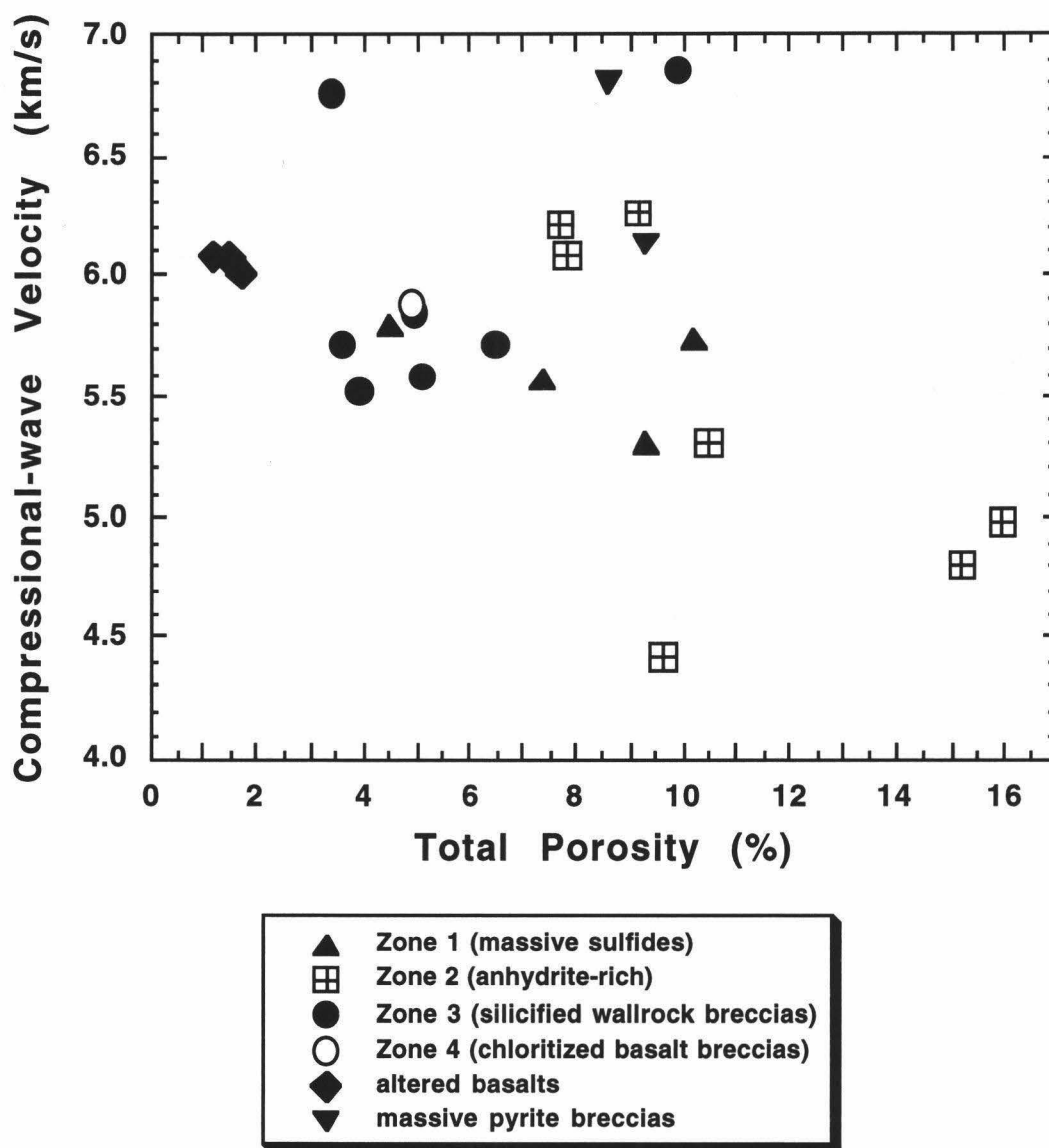
Figure 3.8. Compressional-wave velocity at 100 MPa as a function of total porosity. The plot symbols correspond to the major internal structure zones of the active TAG mound.

3.6 DISCUSSION

3.6.1 Seismic Velocities and Porosity Structure

The results of the ultrasonic experiments for samples from the TAG-1, TAG-2, and TAG-5 area are shown in Figures 3.9, 3.10, and 3.11 respectively. In general, a substantial increase in velocities is recorded between 5 MPa and 15 MPa. At higher pressures both compressional-wave velocities and shear-wave velocities increase steadily. Silicified wallrock breccia samples from both the TAG-1 and the TAG-2 area show steeply increasing velocity versus pressure curves, while a massive granular pyrite sample from TAG-2 and two pyrite-silica breccia from TAG-5 have much "flatter" curves. The application of increasing confining pressure during measurements reduces the aperture of drilling-related cracks and some endemic cracks, so that both compressional-wave velocities and shear-wave velocities increase as porosity effects decrease [*Wilkens et al.*, 1991]. Some of the samples show an abundance of thin cracks and unfilled vesicular pore spaces after microscopic examination (Table 3.2). In general, those same samples show the largest effect on velocity increases with pressure.

In a recent study by *Johnston et al.* [1995], it has been suggested that thin cracks may be introduced by a reduction of confining pressure from raising the rocks from the seafloor to atmospheric pressure. This observation was made for low-porosity basalts with a low population of microcracks. The low permeability of these rocks prevents seawater-saturated pore spaces from losing pressure quickly, thereby significantly increasing the pore pressure until cracking occurs while the confining pressure decreases. This effect, however is not of any concern for the sulfide-rich samples from the TAG mound, since their relatively high porosity and permeability would prevent pore fluid overpressuring. Microscopic analyses of the TAG samples suggest that the thin cracks and vesicular pore
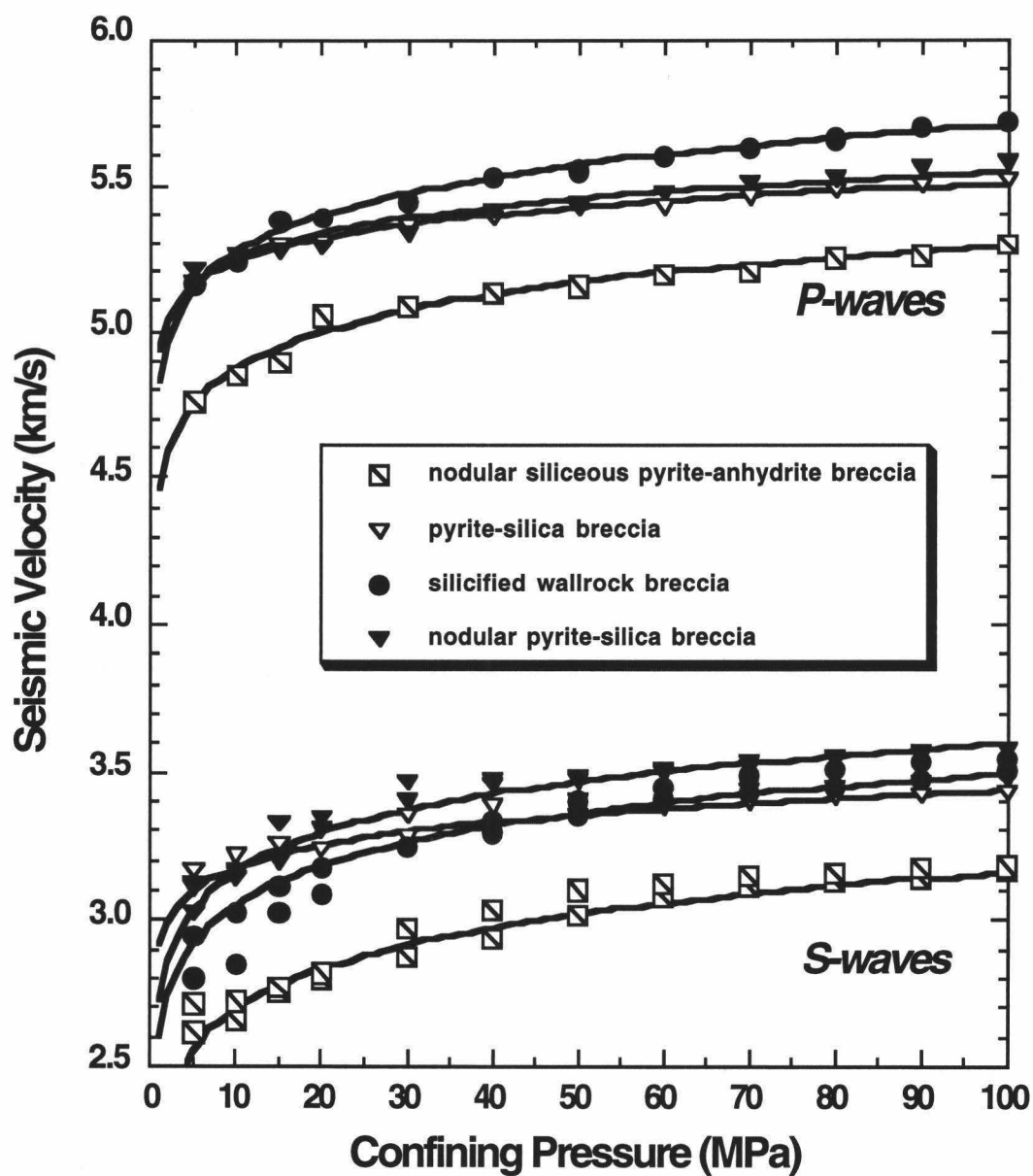
63

Figure 3.9. Compressional-wave and shear-wave velocity as a function of confining pressure for sulfide samples from the TAG-1 Area (Southeast Side of the Black Smoker Complex).
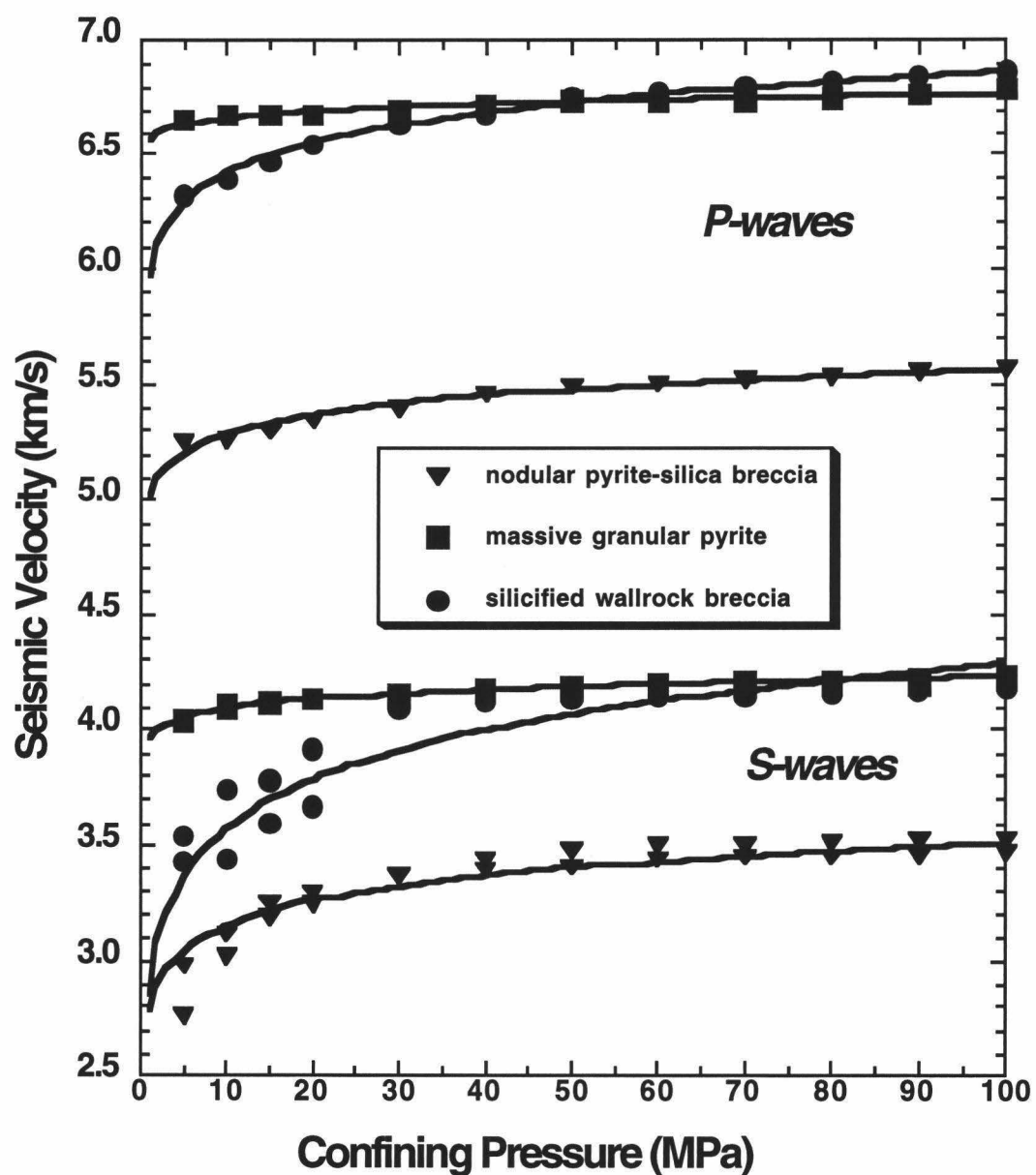
Figure 3.10. Compressional-wave and shear-wave velocity as a function of confining pressure for sulfide samples from the TAG-2 Area ("Kremlin" White Smoker Complex).
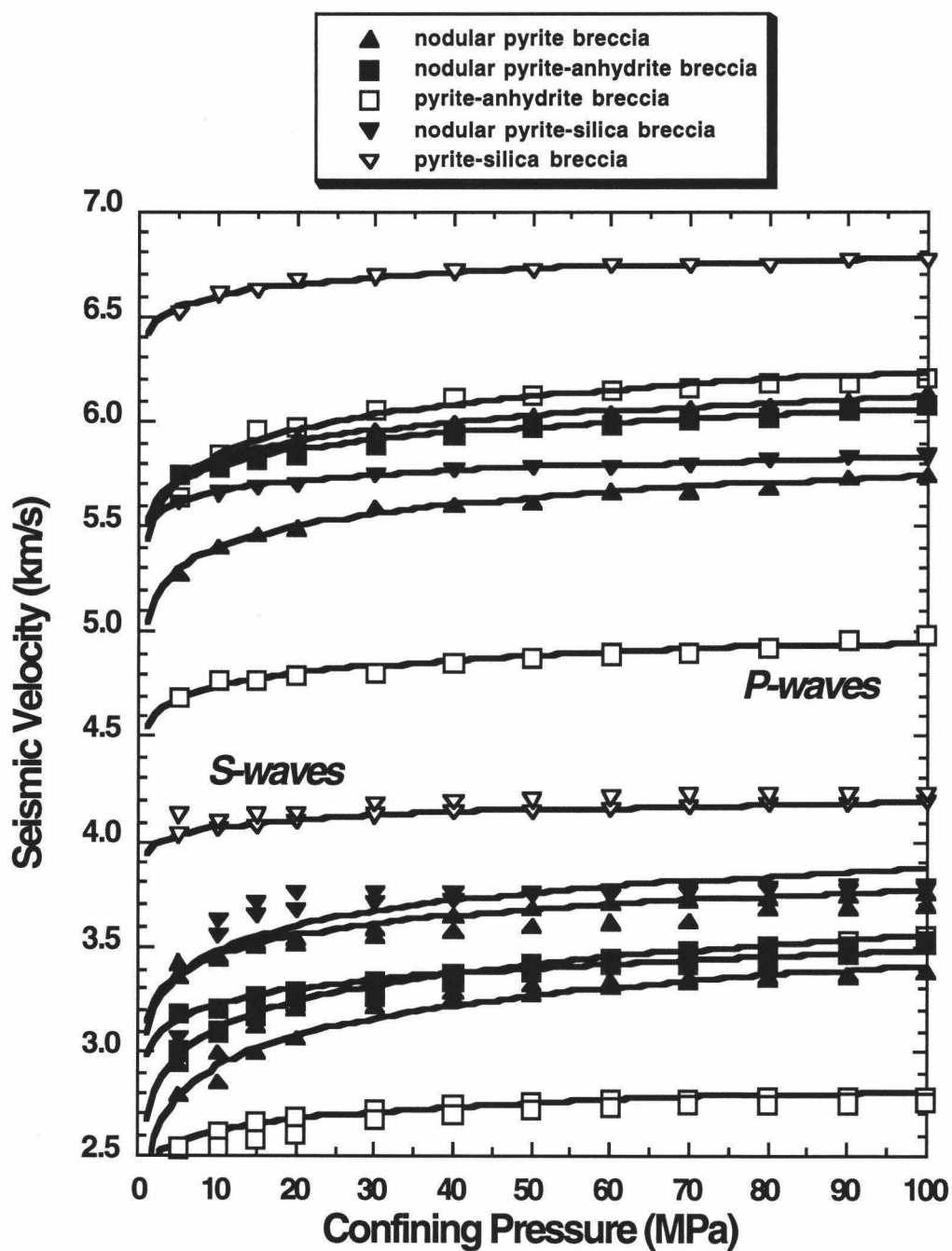
Figure 3.11. Compressional-wave and shear-wave velocity as a function of confining pressure for sulfide samples from the TAG-5 Area (North Side of the Black Smoker Complex).

spaces present are probably in-situ properties of those rocks, since no radial cracking, typical for the pore fluid overpressuring, was observed. The effect of different pore shapes on the measured seismic velocities is discussed later.

Compressional-wave velocities are plotted versus average shear-wave velocities in Figure 3.12, along with lines of constant V_p/V_s ratio. Rock types of the different zones have distinct characteristics. Two of the massive sulfides near the surface of the mound tend to have a high V_p/V_s ratio of 1.8 to 1.9. Anhydrite-rich samples exhibit medium to high values ranging from 1.65 to 1.85. The more silicified samples of Zone 3 as well as the chloritized basalt sample of Zone 4 clearly plot on lines of low V_p/V_s, narrowly ranging from 1.55 to 1.6 for seven out of eight samples, with the remaining sample only slightly higher at 1.65. While increased silicification of the different rock types with depth increases compressional-wave velocities (Figures 3.5 and 3.6), the shear-wave velocities are less affected. In terms of porosity structure, these relatively high shear-wave velocities can be explained by a high concentration of large aspect ratio pore spaces (e.g. vesicles) rather than a high concentration of small aspect ratio voids (e.g. thin cracks), because vesicular pore spaces will reduce shear-wave velocities much less than thin cracks.

The velocities of the two orthogonal shear waves S1 and S2 are compared in Figure 3.13. Most samples plot on or near the line of equality, confirming visual and microscopic observations which indicate a random rather than preferred orientation of both minerals and void spaces. However, the nature of this study can only detect variations at the hand sample scale and while large-scale anisotropy might exist within the mound, nothing can be inferred at this point due to the lack of any other kind of seismic data.
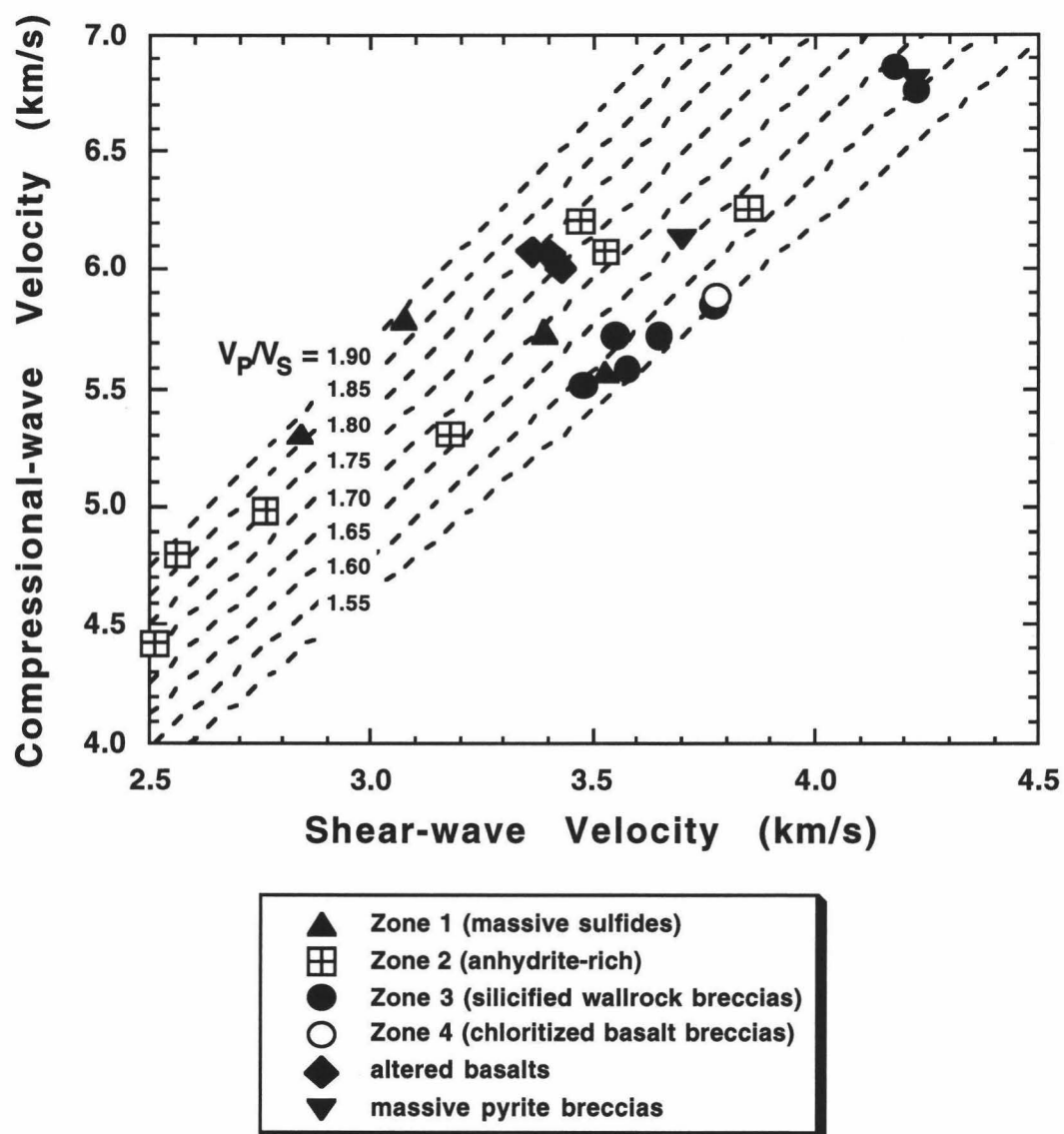
Figure 3.12. Compressional-wave over shear-wave velocity ratio for all minicore samples at 100 MPa. Lines of constant Vp/Vs are shown.
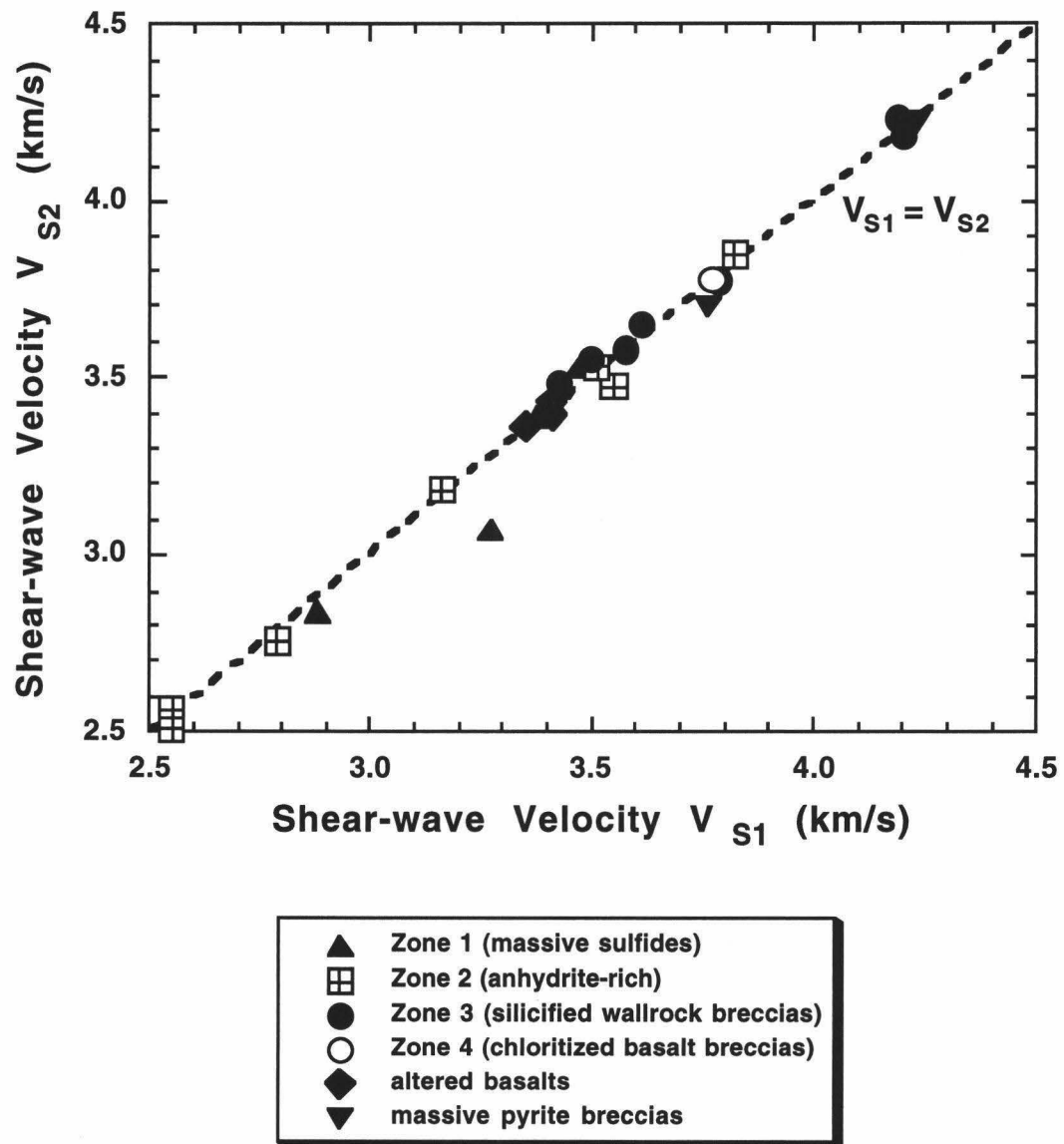
Figure 3.13. The relationship between the velocities of the two orthogonally to each other propagating shear waves S1 and S2 is plotted to test for potential anisotropy effects.

3.6.2 Sulfides

An exception to the near-equality of shear-wave velocities for the two orthogonally propagating shear waves S1 and S2 can be observed for the massive sulfide samples found in the upper few meters of the mound (Zone 1) which is illustrated in Figure 3.14. Two massive sulfide samples from the TAG-1 area have significantly lower S2 than S1 velocities. Those samples were recovered from Hole 957F in relatively close proximity of the active Black Smoker Complex (BSC). Since these samples are oriented, propagation of S2 waves is in the plane parallel to the drill core axis (Figure 3.3). The distinct orientational preference might be explained by the location of those samples near the major upflow conduit (Figure 3.1). A massive sulfide sample recovered at TAG-5 shows the opposite effect of having a higher S2 than S1 velocity. TAG-5 being at the northern side of the actively venting BSC represents an area where seawater preferably penetrates into the mound, a very different hydrothermal regime than at TAG-1. One other massive sulfide sample from the TAG 2 "Kremlin" area does not exhibit any preferred orientation for shear wave propagation. These anisotropic shear-wave velocity observations, however, must be interpreted with caution, since too few of the massive sulfide samples were available for the seismic velocity measurements.

Compressional-wave velocities as a function of sulfide mineral percentage is presented in Figure 3.15. An increase in V_p can be observed with increase in the concentration of the TAG samples' major sulfide minerals, i.e. pyrite and chalcopyrite for all samples of Zone 2 and Zone 3 (Table 3.2) owing to the high bulk moduli of the sulfide minerals.
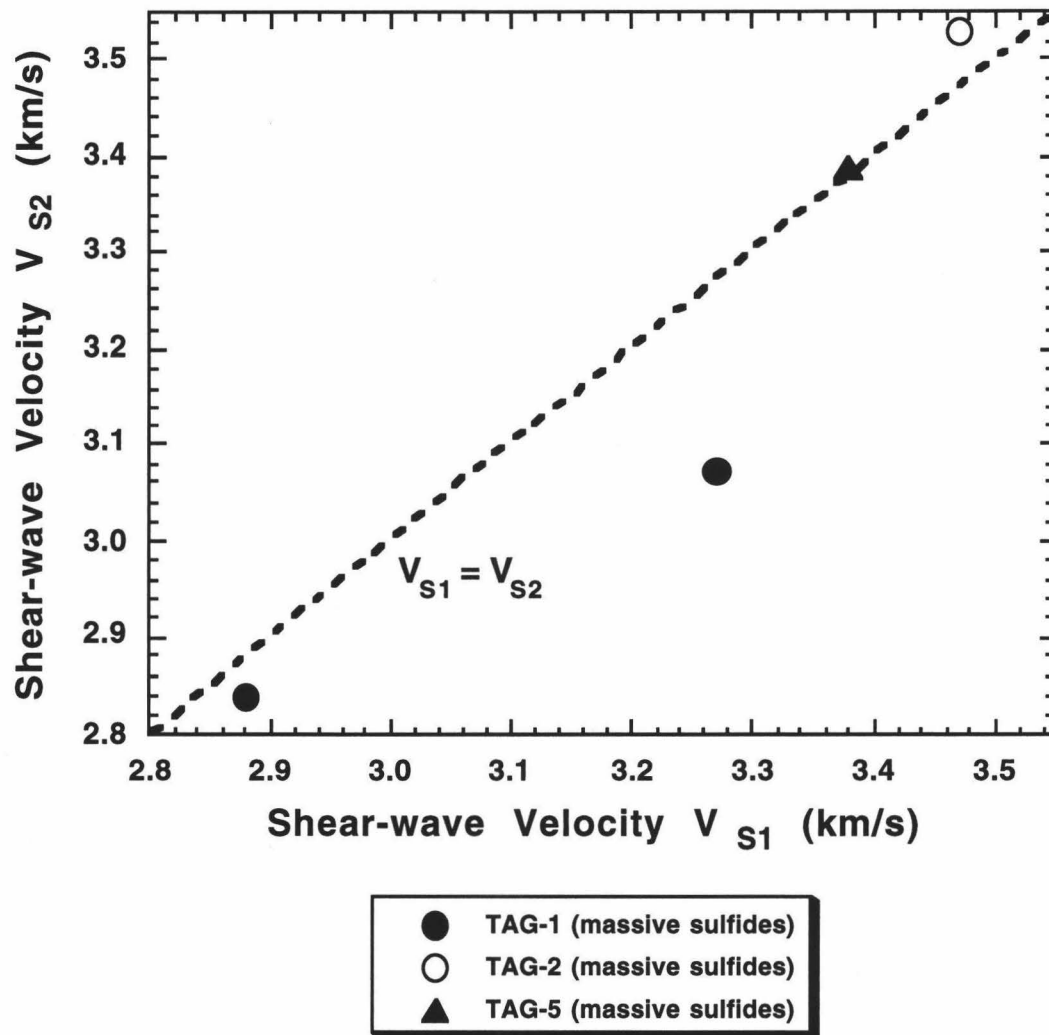
Figure 3.14. The relationship between the velocities of the two orthogonally to each other propagating shear waves S1 and S2 for massive sulfides of the upper Zone 1. A distinct shear-wave velocity anisotropy was measured on samples from the TAG-1 Area (Southeast Side of the Black Smoker Complex).
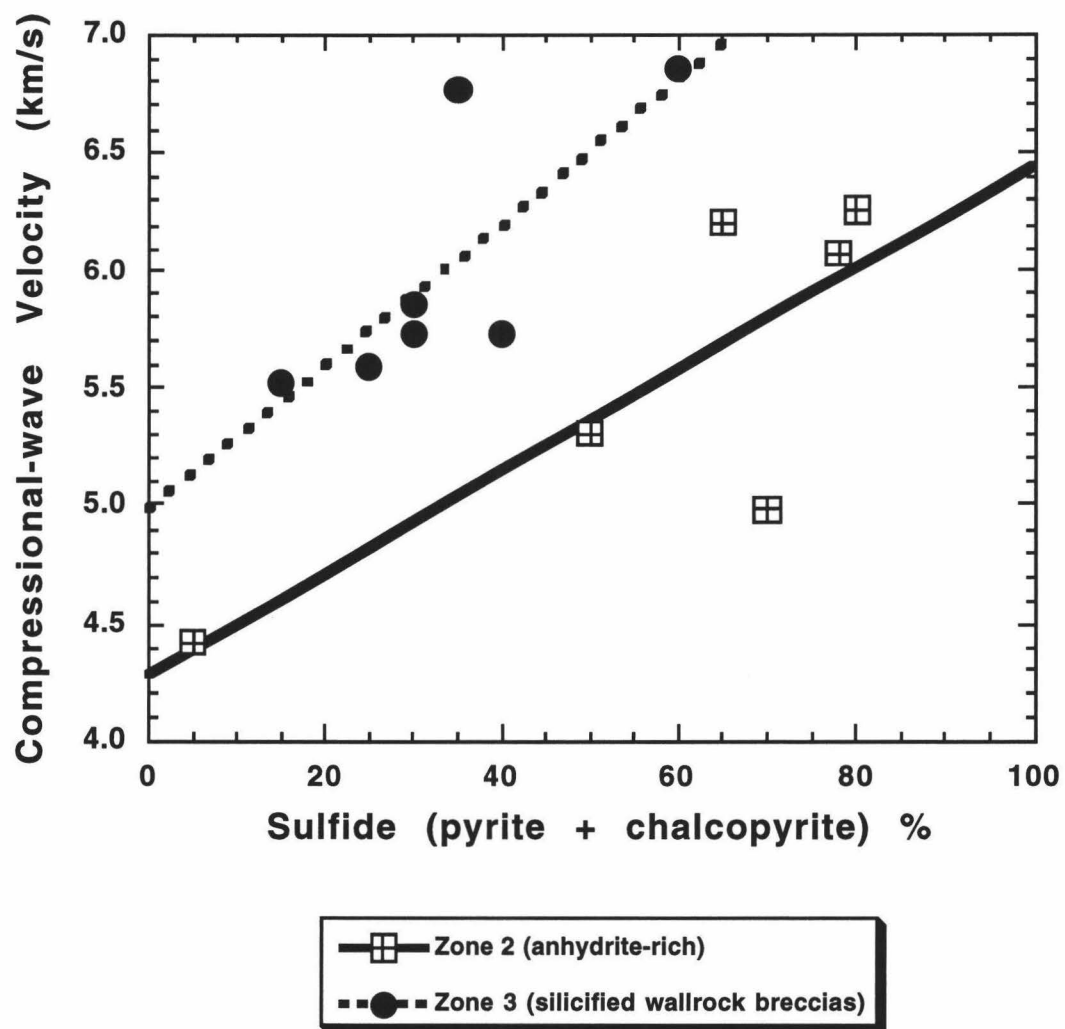
Figure 3.15. Compressional-wave velocity measured at 100 MPa as a function of the samples' major sulfide minerals concentration. Minicores from the anhydrite-rich Zone 2 and minicores from the intensely silicified wallrock breccia Zone 3 show a linear correlation.

3.6.3 Sulfates

The abundance of anhydrite preserved within the mound (estimated to be in the order of 10^5 m^3) was unexpected. Owing to its retrograde solubility (i.e. its solubility decreases with increasing temperature), the precipitation of anhydrite from seawater at a water depth of 3,650 m requires the seawater to be heated to temperatures higher than 150° C. Hence the presence of anhydrite reflects the high temperatures maintained within the mound and its abundance implies substantial entrainment of cold seawater into the interior of the deposit. Estimates of the convective heat flux from the BSC are in excess of 200 megawatt [*Rona et al.*, 1993]. The focusing of this flux in a small area suggests that the vigorous high velocity discharge of hot, hydrothermal fluids result in seawater being drawn into the edges of the mound and into the upflow zone beneath the BSC [*Tivey et al.*, 1995], where it is heated by mixing with the high temperature hydrothermal fluids. By this mechanism many cubic kilometers of seawater may have been entrained over the life of the hydrothermal system. During long periods of inactivity, temperatures within the mound undoubtedly decreased below 150° C causing abundant dissolution of anhydrite and resulting in the formation of open spaces and collapse breccias.

Compressional-wave velocities as a function of anhydrite concentration are shown in Figure 3.16. Seismic velocities of the anhydrite-rich samples of Zone 2 are substantially affected by the abundance of the sulfate mineral. A linear correlation of decreasing V_p with increasing anhydrite concentration can be postulated. Two anhydrite-bearing samples from the underlying silicified Zone 3 show an even greater dependence. From microscopic observations of some of the samples plotted in Figure 3.16, it can be concluded that with an increase in anhydrite concentration, concentration of thin cracks and vesicular pore spaces also increases. Both effects, the relatively low bulk moduli of anhydrite and the
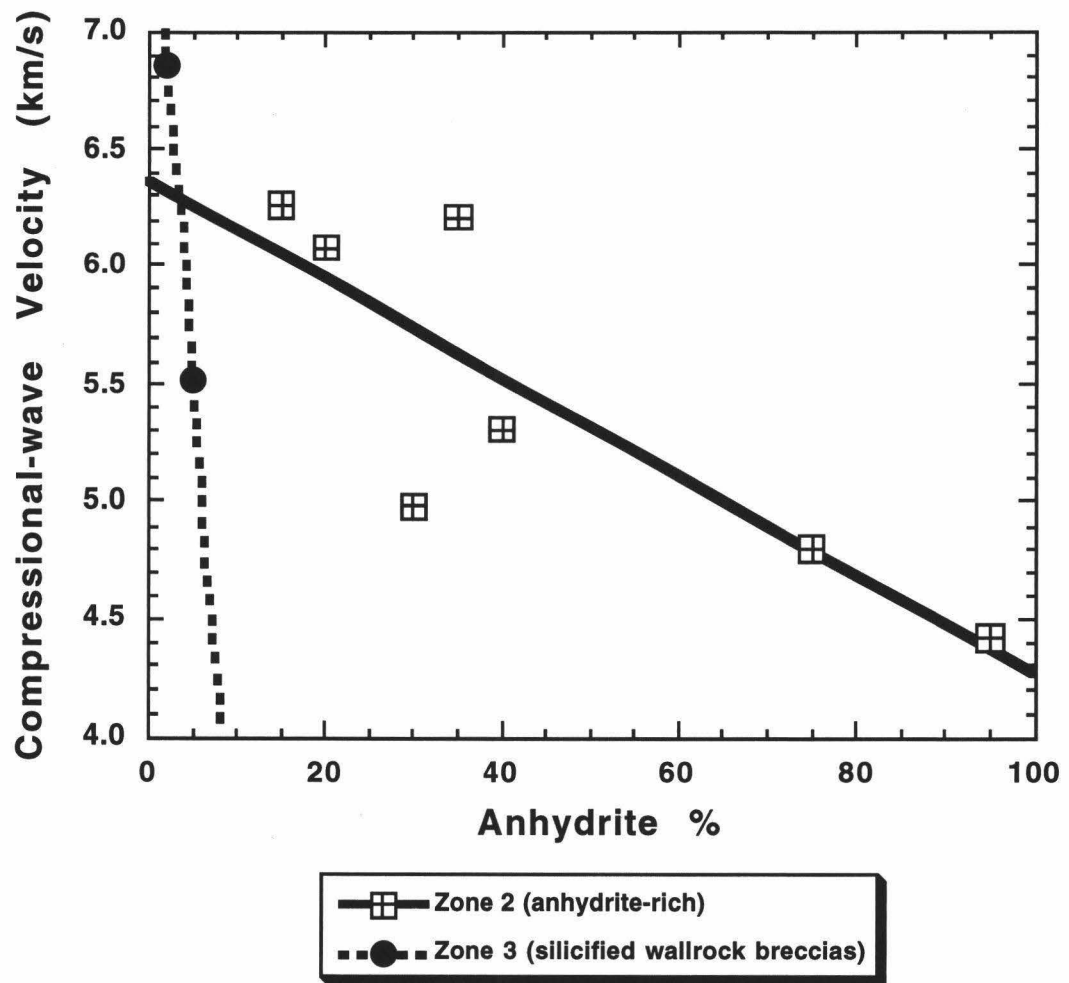
Figure 3.16. Compressional-wave velocity measured at 100 MPa as a
function of anhydrite concentration for samples from Zone 2 and 3.
Minicores from the anhydrite-rich Zone 2 show an inverse linear
correlation.

increase in small aspect ratio pore spaces are the cause of this observed velocity/anhydrite concentration dependence.

Another characteristic of the sulfate-rich samples is illustrated in Figure 3.17. As increasing confining pressures were applied to the anhydrite Sample 957C-7N-3, 15-17 cm, some cracks closed but only partially reopened after pressures were reduced, resulting in velocity hysteresis, as seen between 5 and 20 MPa. While similar measurements consisting of increasing and decreasing pressure cycles were performed for all major rock types, only the anhydrite-enriched samples of Zone 2 showed this hysteresis behaviour.

3.6.4 Basalts

Drilling into basalt with different degrees of alteration is an indicator of the horizontal and vertical dimensions of the mineralized upflow zone. Altered basalt samples were recovered at a depth range of 43-47 m at TAG-4, Hole 957M, west of the BSC and a chloritized basalt breccia was recovered at a depth of 107 m at TAG-1 Hole 957E . Results of the ultrasonic measurements on these samples are presented in Figure 3.18. Although similar in appearance the different basalts have distinctively different characteristics associated with different degrees of alteration and porosity structure. Basalts from TAG-4 are altered, have a low porosity (Φ = 1.2%-1.7%) and increase in compressional-wave velocities from about 5.9 km/s at 5 MPa to 6.1 km/s at 100 MPa. In the same samples shear-wave velocities increase from about 3.3 km/s at 5 MPa to 3.4 km/s at 100 MPa. On the other hand, the relatively high porosity (Φ = 3.5%) chloritized basalt sample from TAG-1 shows an increase in compressional-wave velocity from 5.3 to 5.9 km/s and an increase in shear-wave velocity from 3.2 to 3.8 km/s at 5 MPa and 100 MPa respectively. These very distinguishable velocity versus pressure curves for basalt samples from
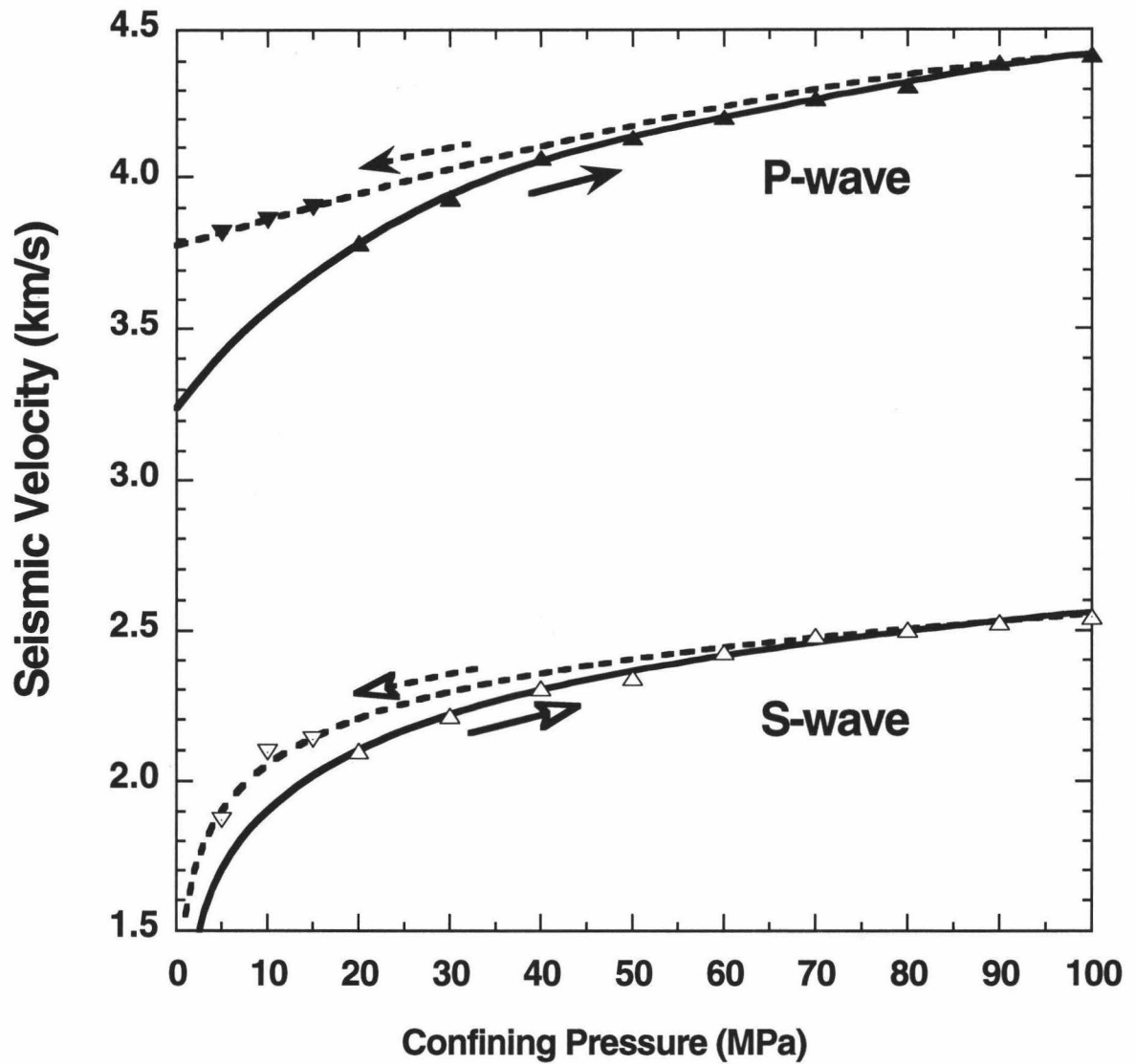
75

Figure 3.17. Compressional-wave and shear-wave velocity as a function of
confining pressure for anhydrite Sample 158-957C-7N-3, 15-17 cm. Both,
compressional-wave and shear-wave velocities show hysteresis between
measurements during increasing pressures (upward pointing triangles)
and measurements during decreasing pressures (downward pointing
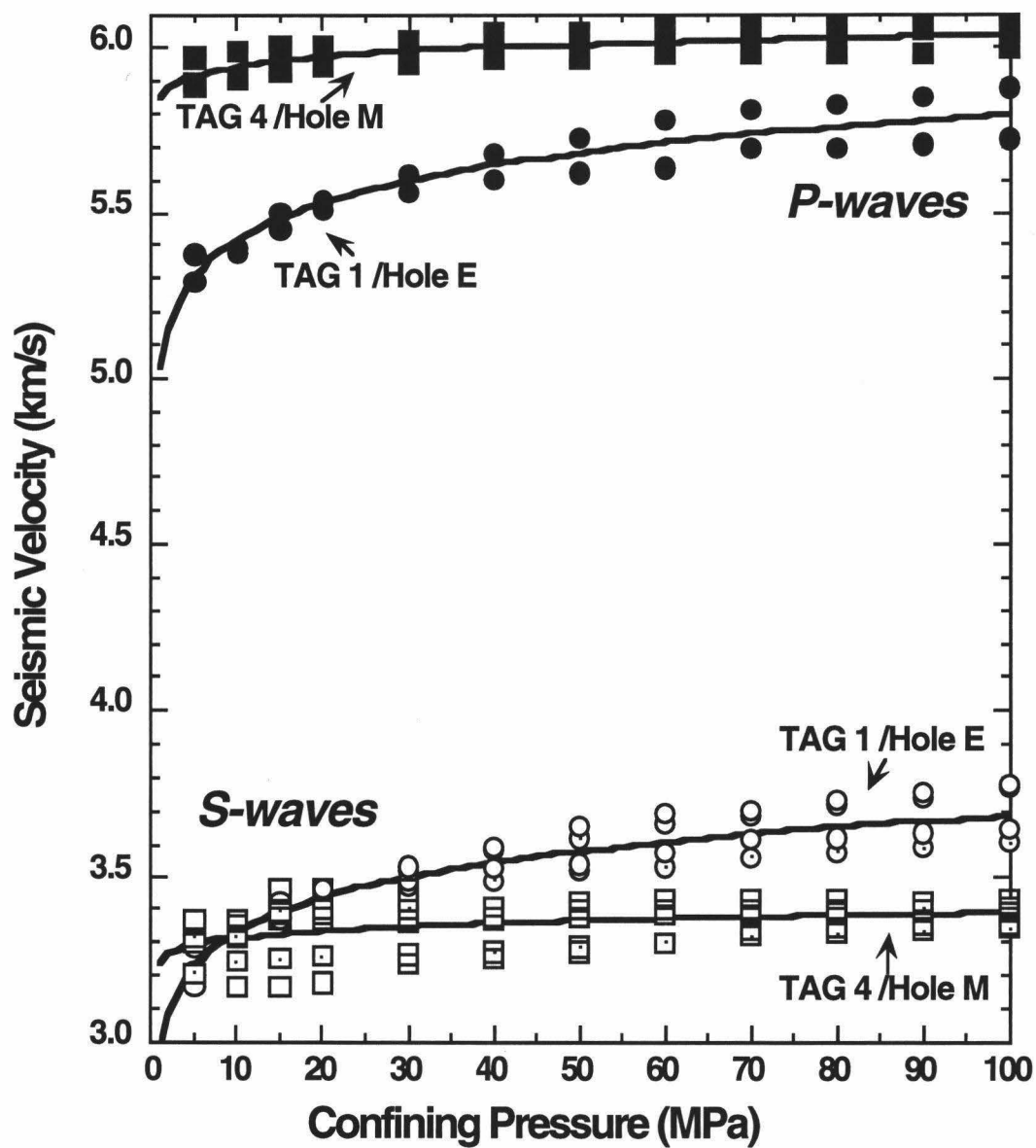triangles) as a result of only partial reopening of cracks.

76

Figure 3.18. Compressional-wave and shear-wave velocity as a function of confining pressure for three basalt samples from the TAG-4 area (west of the Black Smoker Complex) and one chloritized basalt breccia sample from TAG-1 (southeast of the BSC).

different parts of the TAG mound indicate dissimilar porosity structures. The TAG-4 basalts must contain only small concentrations of thin, small aspect ratio cracks while the TAG-1 basalt must be comprised of many thin cracks that close during the increasing pressure cycle.

Christensen and Salisbury [1975] compared compressional-wave velocities and densities for 77 seafloor basalts and suggested a non-linear relationship between these quantities. For "normal" seafloor basalts their model predicts a compressional-wave velocity of 6.37 km/s for a given density of 2.88 g/cm^3 (the density of the basalt samples from TAG-4; Table 1). For the TAG basalts, however, V_p is less than 6.1 km/s and the total porosity of 1.2%-1.7% is low. Microscopic analysis suggests few unfilled pore spaces and the few void spaces seen are predominantly vesicular (Table 3.2), however the samples have a framework composed of altered grains. A low concentration of large aspect ratio pore spaces (e.g. vesicles) will cause only a negligible reduction in compressional-wave velocity [e.g. *Ludwig et al.*, 1996 in review; *Shearer and Orcutt*, 1985; *Wilkens et al.*, 1991].The deviation from "normal" basalt velocities must therefore be a direct result of hydrothermal alteration rather than porosity effects.

3.7 POROSITY MODELS

Understanding the porosity structure of an active hydrothermal system is essential for describing both present and past episodes of hydrothermal activity. Research projects concerning fluid flow, geochemical fluxes, and alteration mechanisms would greatly benefit from constraints on the pore shape concentration of the different rock types encountered during drilling of the active TAG hydrothermal mound.

The velocities of seismic waves traveling through a rock are affected by the rock's porosity, the shape of its pores, and the media filling the pores. To infer porosity and pore shape from seismic velocities requires a theory relating these different properties, but as *Berge et al.* [1992] show, no theory is completely adequate for the high porosities and broad range of pore shapes present in the seafloor. There are two broad groups of theories: self-consistent theories, for which each crack is treated as if it were embedded in a cracked background medium (following rock physics orthodoxy we use "crack" to identify any pore space), and noninteraction theories, which treat each crack as if it were isolated in an uncracked background. Strictly, these theories are valid only for very small crack densities (i.e., for small porosities). As crack density is increased, self-consistent theories will tend to overestimate the softening effects of cracks, so for a given porosity the velocity they predict will be too small. Noninteraction theories underestimate the effects of cracks and err in the other direction, predicting velocities which are too high for a given porosity. The disagreement between the theories at large porosity can be significantly reduced by treating the total porosity as if it has been built up recursively, a small number of cracks at a time, with each new crack "feeling" the cracks which came before but being unaffected by the cracks which have yet to be added. The result is an hybrid or extended theory, which combines both noninteraction and self-consistent philosophies and which is correct at least to second order in the crack density [*Berge et al.*, 1992; *Cheng*, 1978] .

In order to infer pore shape distributions of oceanic crust from seismic data, extended versions of both, the Kuster-Toksöz theory [*Kuster and Toksöz*, 1974a; *Kuster and Toksöz*, 1974b] and the Walsh theory [*Walsh*, 1969] have previously been applied with success. [*Berge et al.*, 1992; *Ludwig et al.*, 1996 in review]. The resulting models provide a distribution of pore space volume over different pore shapes defined by their aspect ratio.

To reproduce the compressional and shear wave velocities of the TAG samples measured at a confining pressure of 1 MPa, we applied an iterative modeling scheme using the extended Kuster-Toksöz (KT+) and the extended Walsh (Walsh+) theories described by *Berge* [1991] and *Berge et al.* [1992] to several samples representing the major internal structure zones of the active TAG mound. Microscopic observations on thin sections corresponding to the ultrasonically-measured minicores together with index property measurements, provided constraints on starting models for this non-unique parameter estimation problem. From these observations, we chose to model for seven aspect ratio (α) bins ranging from $\alpha = 1$ (vesicles) to $\alpha = 0.001$ (thin elongated cracks). Besides this assumed distribution of pore spaces, elastic moduli and densities for both the background material and the pore fluid are required as input parameters. For the background material these parameters were estimated by the mineralogy of the sample, and the measured grain density (Tables 3.1 and 3.2). For the parameters of the pore fluid, we assumed those of seawater with a salinity of 3.5%, a typical value for North Atlantic deep water [*Sverdrup et al.*, 1942]. The same value was obtained during several bottom water measurements by shipboard analyses during ODP Leg 158 [*Humphris et al.*, 1996].

We computed the theoretical velocities for the model, compared the result to Table 3.3, and adjusted the model by changing the contribution to porosity in each bin. As porosity at any particular aspect ratio is adjusted, both V_p and V_s are affected. Very roughly, an increasing population of thin, water-filled cracks (a<0.01) will reduce V_s faster than it reduces V_p, while an increasing population of thick cracks (a>0.01) will reduce V_p faster than V_s [*Shearer*, 1988]. From this knowledge it is relatively easy to work out how to adjust the porosity at each aspect ratio to achieve the desired velocities.

In the following figures pore volume is plotted on a logarithmic scale versus bins of aspect ratio. By summing the porosities in each aspect ratio bin, we obtain the total

porosity, with the extended Walsh modeling providing us an upper porosity bound and the extended Kuster-Toksöz modeling provided a lower bound.

The pore shape distribution of a representative massive sulfide sample of Zone 1 is shown in Figure 3.19. The sample, a massive pyrite breccia, Sample 957F-1N-1, 62-64 cm, has a very high concentration of sulfides (85% pyrite and 5% chalcopyrite; Table 3.2) and a grain density of 3.83 g/cm^3. Unfortunately, pore shape constraints are very limited for this particular sample, because the matching thin section was damaged during preparation. However, an overall high porosity was determined visually. To obtain matching compressional-wave and shear-wave velocities of 5.3 km/s and 2.9 km/s during modeling, a relatively high concentration (5.9% for KT+ and 6.6% for Walsh+) of spherical pores (α = 0.5-1.0) is required. Pore spaces of smaller aspect ratio have lower concentrations with the thin cracks of α = 0.001 having the lowest concentration of 0.5% for KT+ and 0.7% for Walsh+. The total porosity for this sample after modeling is 9.9% for KT+ and 10.8% for Walsh+ compared to 9.3% obtained by the calculation of index properties.

The anhydrite-rich Zone 2 is comprised of two distinctive type of rocks: Up to 45 cm long almost pure anhydrite veins and sulfide-anhydrite breccias. Sample 957C-7N-3, 15-17 cm represents the first type, comprised of 95% anhydrite and only 5% sulfides (Table 3.2). Microscopic analysis suggests a high total porosity. The modeled porosity distribution is presented in Figure 3.20. A high concentration of spherical pore spaces (9.7% for KT+ and 10.1% for Walsh+) is necessary to account for the high total porosity without considerable reduction in seismic velocities which are less affected by high concentrations of large α pores than by high concentrations of small α pores. The KT+ method yields a total porosity Φ = 10.6% and the Walsh+ method yields Φ = 11.1%. The total porosity obtained from index properties measurements is 9.6%.
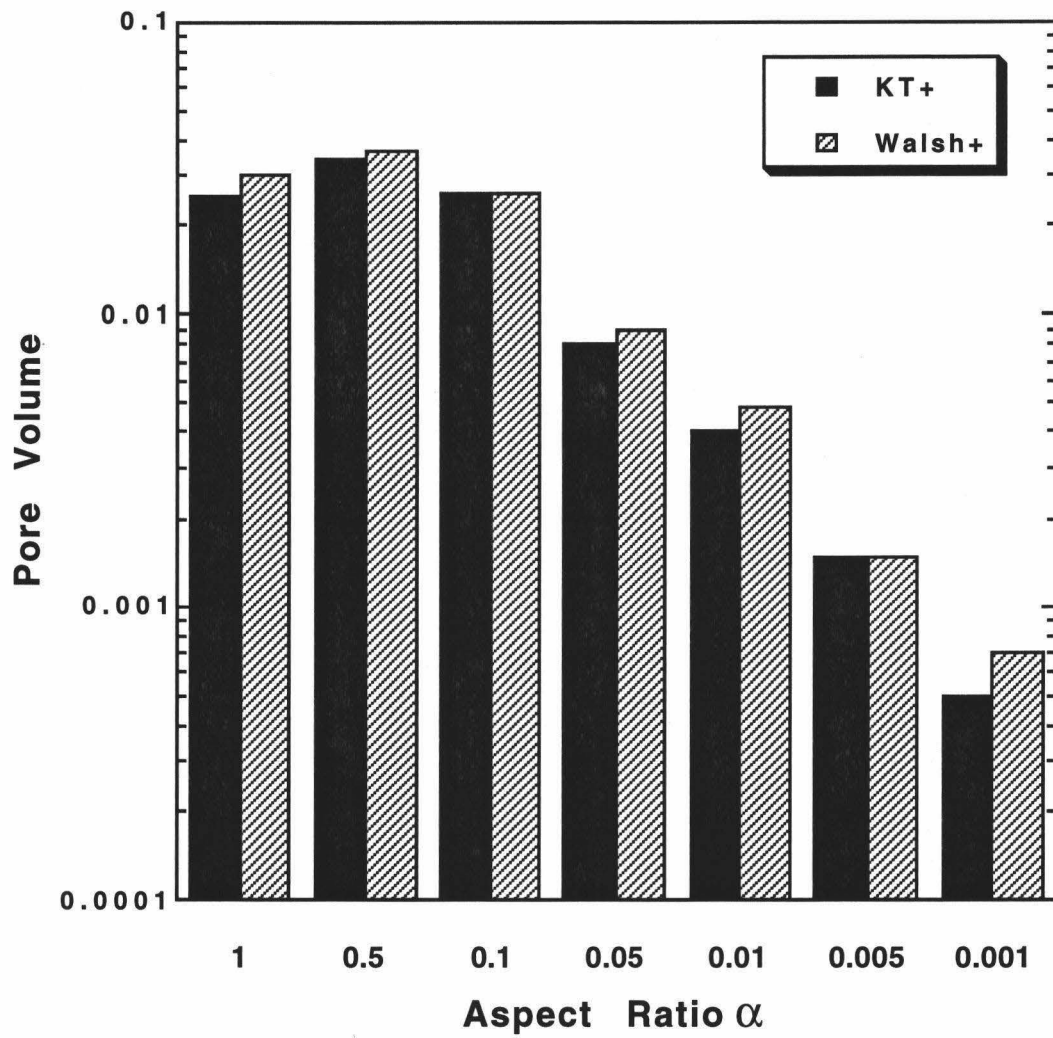
Figure 3.19. Aspect Ratio distribution for massive pyrite breccia Sample
158-957F-1N-1, 62-64 cm, representing the massive sulfides of Zone 1
after using extended Kuster - Toksöz (KT+) and extended Walsh (Walsh+)
theory. The total porosity $\Phi = 9.9\%$ for the KT+ model and $\Phi = 10.8\%$
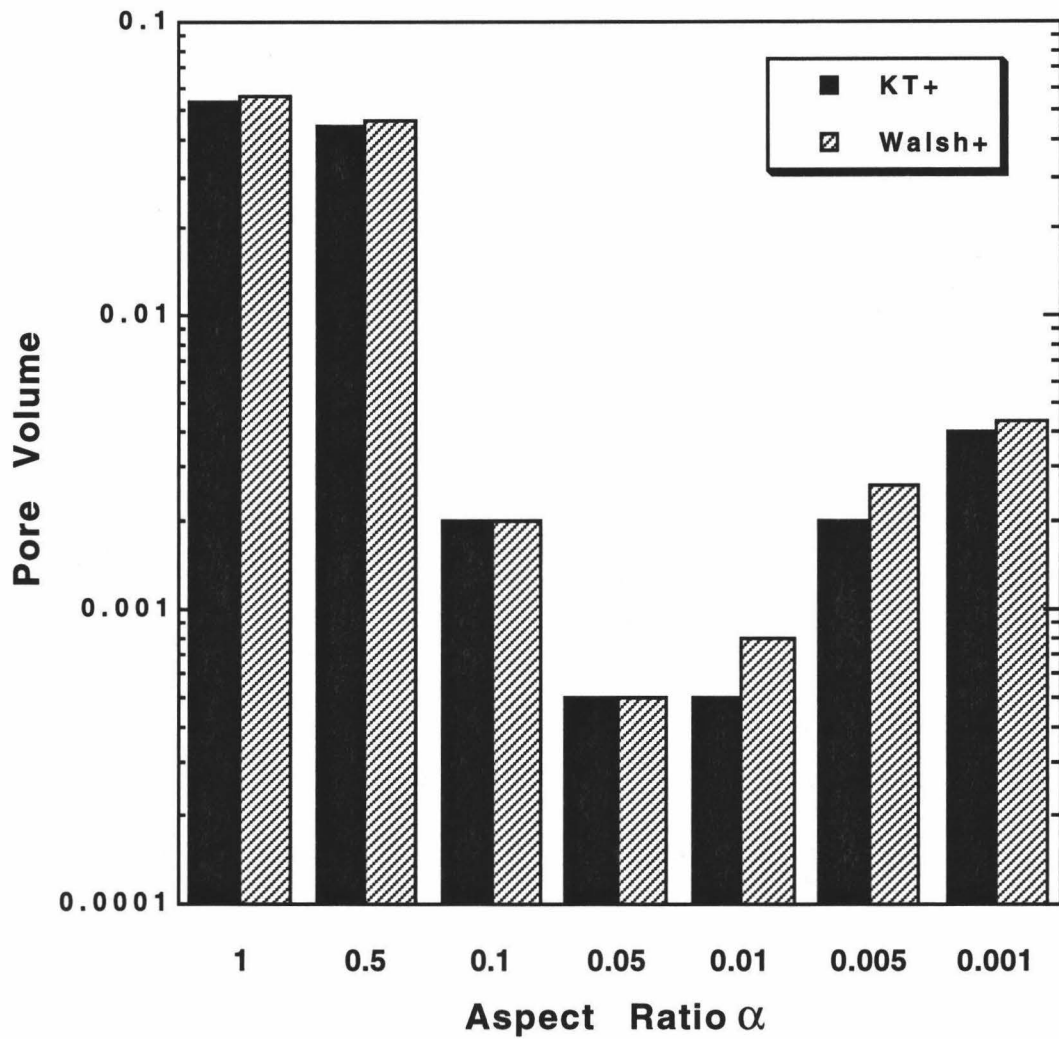for the Walsh+ model.

Figure 3.20. Aspect Ratio distribution for an "almost pure" anhydrite Sample 158-957C-7N-3, 15-17 cm, representing an anhydrite vein of Zone 2 after using extended Kuster - Toksöz (KT+) and extended Walsh (Walsh+) theory. The total porosity $\Phi = 10.6\%$ for the KT+ model and $\Phi = 11.1\%$ for the Walsh+ model.

Sample 957P-1R-1, 49-51 cm represents the second type of Zone 2 rocks, a pyrite-anhydrite breccia. Although this sample has a massive sulfide concentration of 70% and "only" 30% anhydrite, the measured seismic velocities (V_p = 4.98 km/s; V_s = 2.78 km/s) are only slightly higher than for the almost pure anhydrite sample (V_p = 4.42 km/s; V_s = 2.53 km/s). This is explained by the high total porosity of the pyrite-anhydrite sample, calculated to almost 16% from index properties measurements. The sample's porosity distribution obtained after modeling is presented in Figure 3.21. As for the anhydrite vein sample, the concentration of α = 0.5-1.0 pore spaces is high at 11.8% and 12.3% for KT+ and Walsh+ respectively. In addition modeling pore space distribution for Sample 957P-1R-1, 49-51 cm requires a high concentration of "crack-like" pore spaces (α = 0.001-0.05) of 5.0% to 5.6%. Total porosity values after modeling are very high, being 17.2% with KT+ and 18.3% with Walsh+. The modeling results agree well with microscopic observations indicating a high porosity sample with elongated cracks and unfilled voids near the intrusion of anhydrite veins (Table 3.2).

A representative sample for Zone 3, the increasingly silicified part of the TAG mound, is Sample 957C-16N-1, 35-37 cm, a nodular pyrite-silica breccia. The corresponding thin section analysis indicates an intermediate porosity with many pyrite nodules being surrounded by cavities and cracks. Pore space modeling results for this sample are shown in Figure 3.22. Ultrasonic velocity measurements (V_p = 5.58 km/s; V_s = 3.58 km/s) were matched by a relatively high concentration of "sphere-like" pores and a low concentration of small aspect ratio pore spaces. This is in agreement with a low V_p/V_s ratio as seen in Figure 3.12, since for a given total porosity large α pore spaces will reduce V_s less than small α pore spaces. The total porosities obtained are 5.5% for KT+ and 5.9% for Walsh+, compared to 5.1% obtained from index properties measurements.
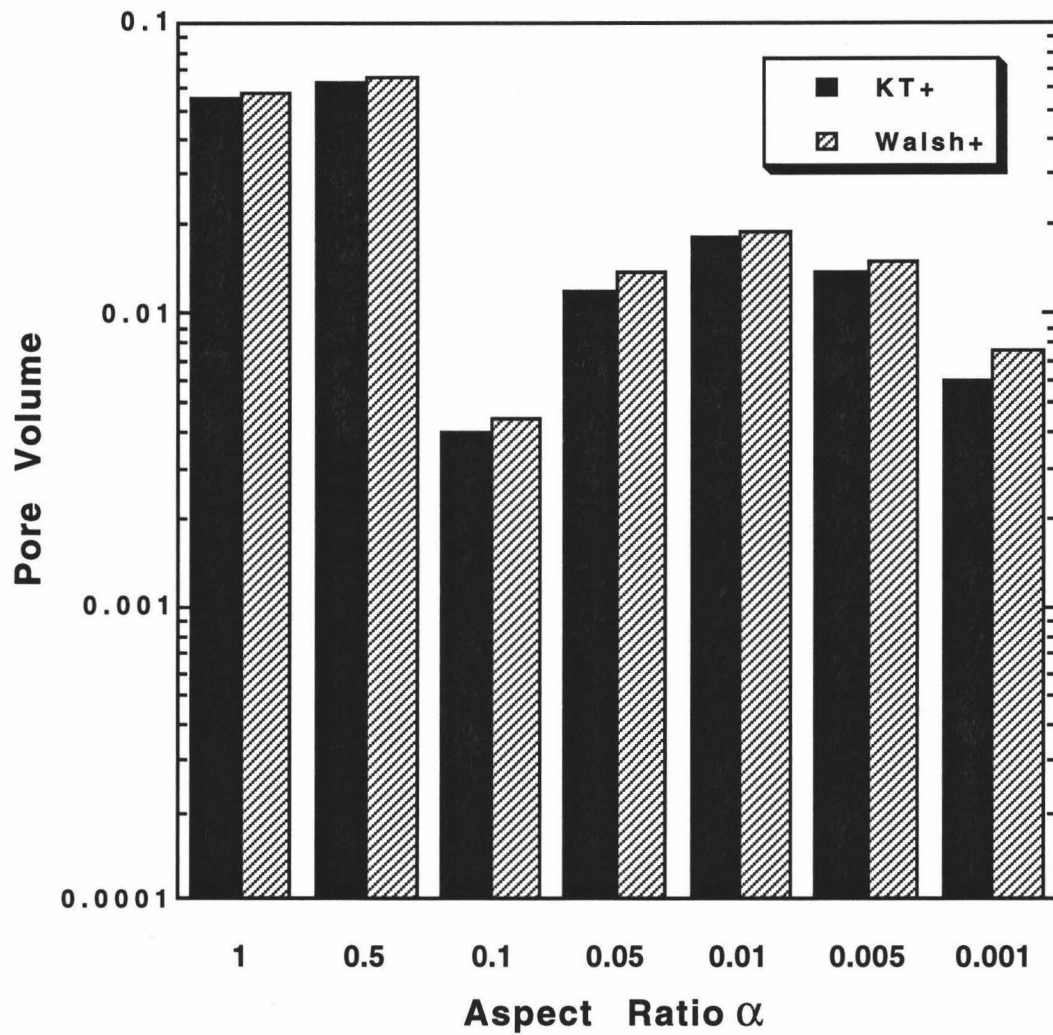
Figure 3.21. Aspect Ratio distribution for high-porosity pyrite-anhydrite breccia Sample 158-957P-1R-1, 49-51 cm, representing the anhydrite-rich Zone 2 after using extended Kuster - Toksöz (KT+) and extended Walsh (Walsh+) theory. The total porosity Φ = 17.2% for the KT+ model and Φ = 18.3% for the Walsh+ model.
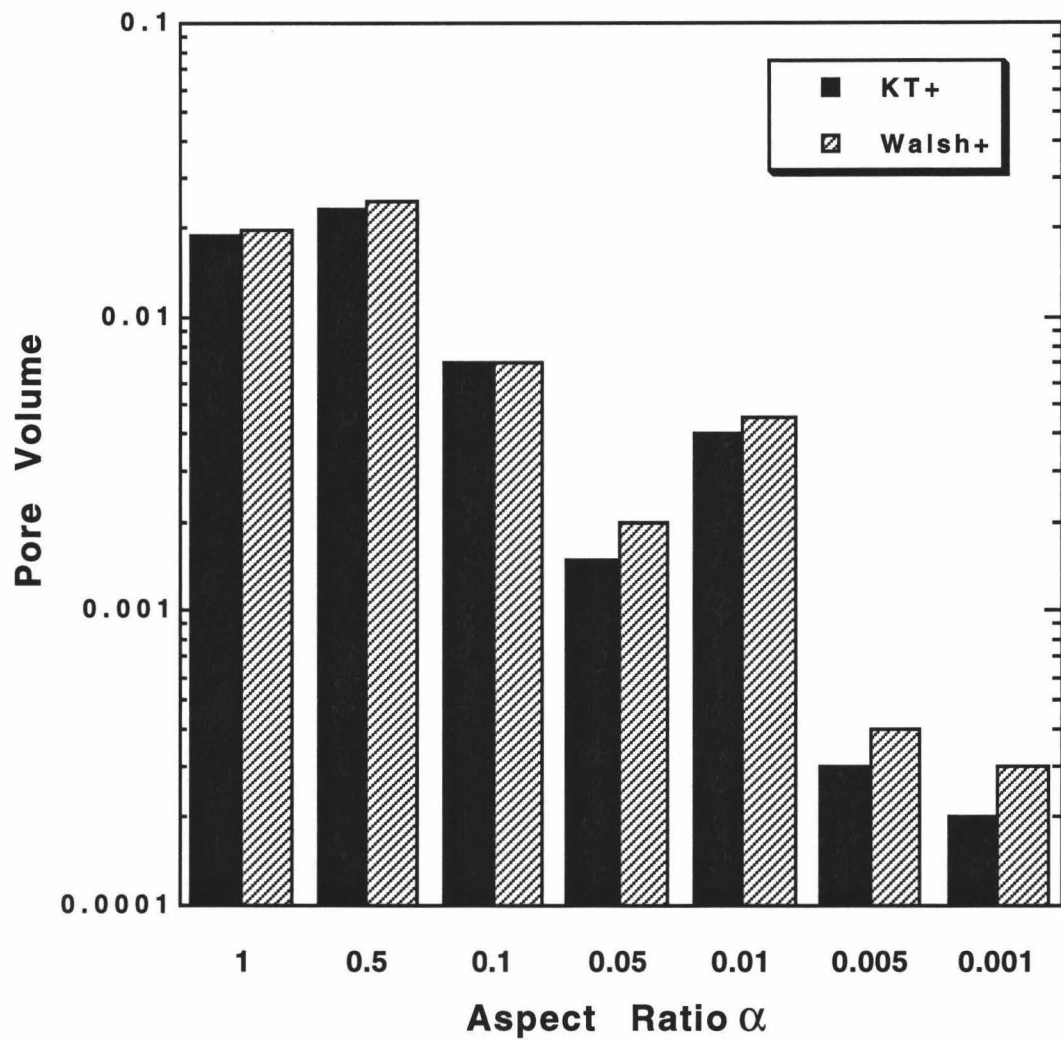
Figure 3.22. Aspect Ratio distribution for nodular pyrite-silica breccia Sample 158-957C-16N-1, 35-37 cm, representing the silicified Zone 3 after using extended Kuster - Toksöz (KT+) and extended Walsh (Walsh+) theory. The total porosity $\Phi = 5.5\%$ for the KT+ model and $\Phi = 5.9\%$ for the Walsh+ model.

One chloritized basalt breccia, Sample 957E-15R-1, 30-32 cm from Zone 4 was analyzed. Its aspect ratio distribution, shown in Figure 3.23, suggests a broad spectrum of pore spaces with a peak for vesicular pores and a low at extremely thin cracks. Total porosity values are 5.8% from KT+ modeling and 6.4% from Walsh+ modeling, compared to 4.9% from index properties calculations. Having no thin section available for this sample, its porosity structure is less constrained. However, at a depth of about 107 mbsf, it is to be expected that thin cracks are either closed or filled by alteration minerals [*Wilkens et al.*, 1991], therefore the results of the modeling are physically meaningful.

The last minicore analyzed for porosity distribution was a basalt sample recovered at TAG-4 (west of the BSC) at a depth of about 47 m. Since all basalt samples showed very similar characteristics during physical properties measurements, Sample 957M-10R-1, 39-41 cm is representative of the entire basalt sequence drilled in Hole 957M. (Tables 3.1-3.3, Figure 3.18). Index properties measurements determined a very low total porosity of 1.7%. The porosity distribution for this sample is shown in Figure 3.24. While there is a broad peak at vesicular pore spaces (α=0.5-1), small aspect ratio pore spaces (i.e. thin cracks) contribute very little to the total porosity of the basalt sample. This agrees well with microscopic observations where most pore spaces were identified as vesicles. However, to match the ultrasonic velocity measurements, a higher than expected total porosity is required by both the KT+ and the Walsh+ theory ($\Phi = 1.9\%$ and $\Phi = 2.1\%$, respectively). Elastic moduli of "normal" oceanic crust basalt, which were used as input parameters for the modeling, are probably "stiffer" than the actual elastic moduli of the background material of the TAG basalts, due to softening effects of altered versus unaltered grains. However, even if the correct moduli were known, we expect the overall porosity distribution to remain similar.
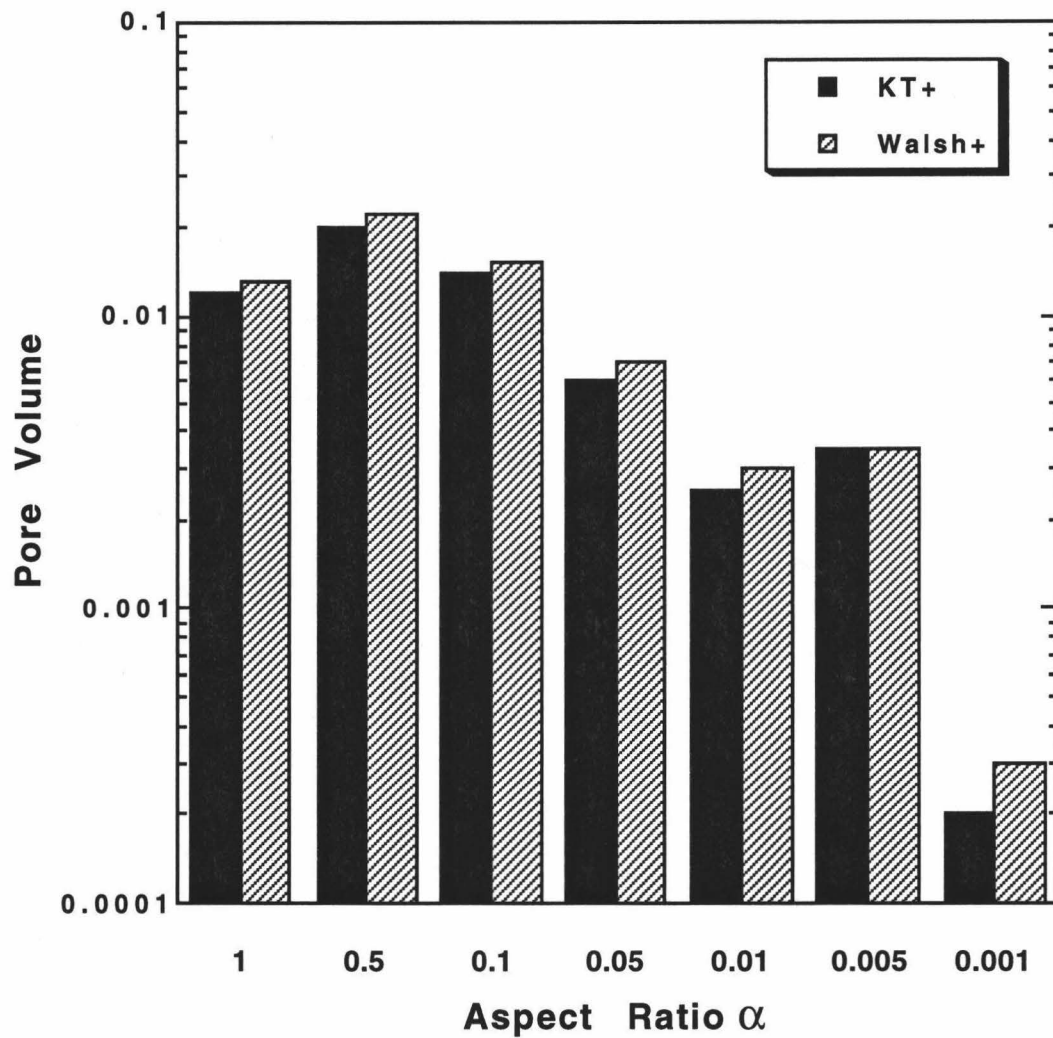
Figure 3.23. Aspect Ratio distribution for chloritized basalt breccia Sample 158-957E-15R-1, 30-32 cm, representing Zone 4 after using extended Kuster - Toksöz (KT+) and extended Walsh (Walsh+) theory. The total porosity $\Phi = 5.8\%$ for the KT+ model and $\Phi = 6.4\%$ for the Walsh+ model.
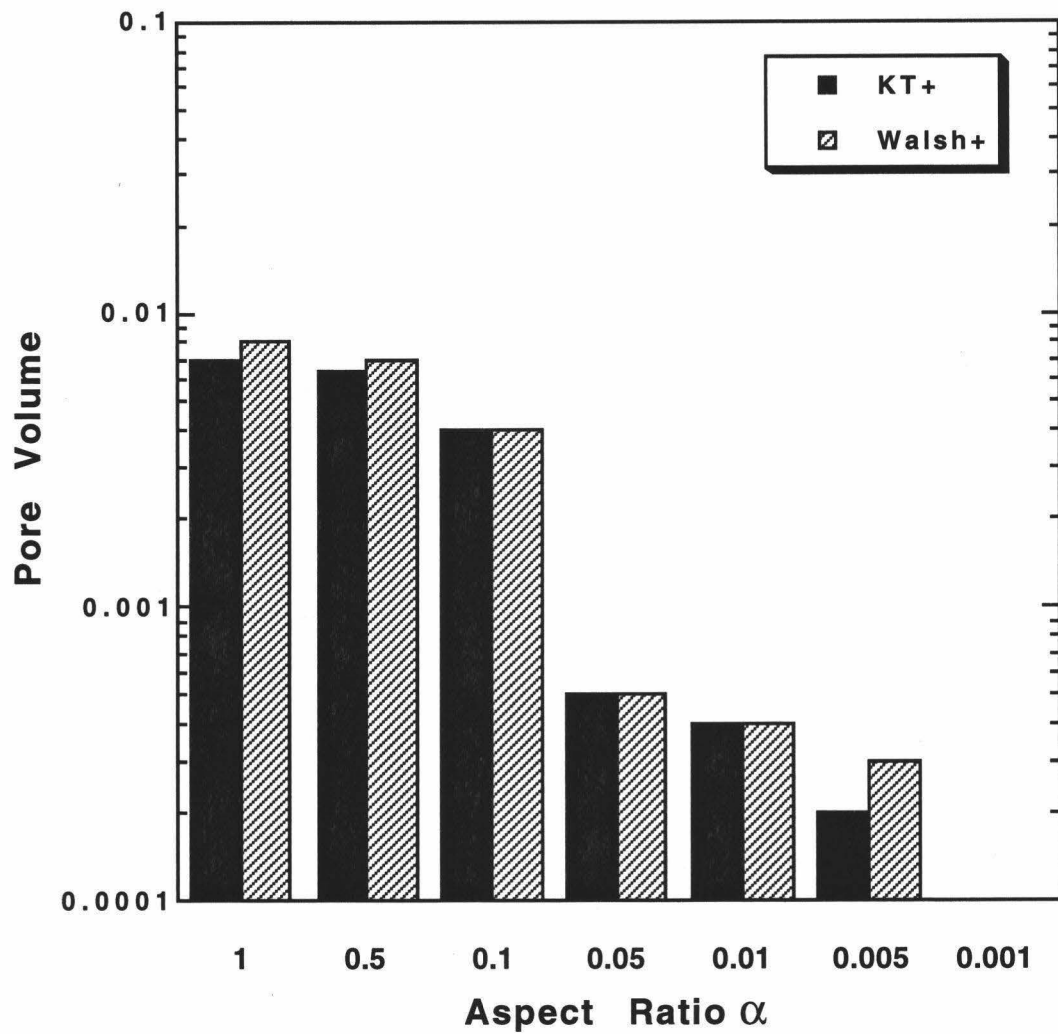
Figure 3.24. Figure 24. Aspect Ratio distribution for altered basalt Sample 158-957M-10R-1, 39-41 cm, representing the basalt sequence recovered at TAG-4 Hole 957M after using extended Kuster - Toksöz (KT+) and extended Walsh (Walsh+) theory. The total porosity $\Phi = 2.0\%$ for the KT+ model and $\Phi = 2.2\%$ for the Walsh+ model.

The extended Kuster-Toksöz and the extended Walsh theory were applied for the first time on a hand sample scale. In summary, the modeling of pore shape distribution from ultrasonic measurements on minicores, which represent the different lithologies of the TAG mound, yield satisfactory results. Whenever microscopic pore shape observations are available, the reliability of the model is greatly improved.

The total porosities obtained from the models are consistently higher than those obtained from direct index properties calculations. The explanation for this is two-fold: First, the assumed elastic moduli as modeling input parameters may be too "stiff", thereby requiring porosities that are too high in order to match the seismic data. Second, index property measurements are likely to underestimate the total porosity due to the assumption that all pore spaces are interconnected (very unlikely for the multi-mineral structures of the TAG for most of the TAG samples) and fluid-saturated during determination of the bulk properties of the wet samples. Estimating an error margin for the assumed elastic moduli of the background material is very difficult due to the heterogeneity of the brecciated samples. Therefore, the results of this modeling are rather speculative. However, without any other porosity-structure information available, these porosity models provide a first-order estimate that matches both the limited visual observations of pore shapes and the seismic velocity measurements.

3.8 CONCLUSIONS

Results from this study provide a unique data and reference set for sulfide, sulfate, and basalt samples from an active sediment-free hydrothermal system.

In general, physical properties (including seismic velocities, densities, porosities, and pore space distribution) are extremely variable within very short distances of the

hydrothermally active mound, both horizontally and vertically. Here is a summary of the results of this research project:

Ultrasonic measurements yield an extensive data set of both compressional-wave and shear-wave velocities and provide a vast improvement over shipboard seismic measurements of P-waves only. A general increase of V_p with depth is observed probably due to increased cementation and silicification of the mostly brecciated rocks recovered from TAG. Anhydrite-rich rocks of Zone 2 show a clear trend of increasing V_p with increasing densities and decreasing porosities. The different rock types have distinct V_p/V_s ratios, illustrating the importance of measuring both V_p and V_s. Massive sulfide samples of Zone 1 show a preferential direction for S-wave propagation, depending on their location within the mound. Rocks of Zone 2 and 3 show a seismic velocity dependence on total sulfide mineral concentration. Porosity effects on seismic velocities increase with higher anhydrite concentration of the rocks. The almost pure anhydrite sample exhibits velocity hysteresis during decreasing confining pressure cycle. Basalt samples deviate from "normal" mid-ocean ridge basalt velocities due to hydrothermal alteration rather than porosity effects.

Porosity distribution models were calculated for representative samples of each major lithologic zone within the TAG mound. Microscopic analysis provides constraints on the models and improves their reliability. Total porosity is consistently higher after modeling than the values obtained from index properties measurements. The discrepancies can be explained with errors in the assumptions for both methods.

Studies such as this should provide further constraints for future investigations of hydrothermal systems. Now that the distribution of porosity over aspect ratio can be delivered from application of rock physics theories to rock samples at a hand-sample scale, the links between porosity, permeability, fluid flow, geochemical fluxes and alteration

91

mechanisms can be explored. At present, the inversion procedure to obtain aspect ratio distribution from velocity measurements, is done by trial and error in a rather ad hoc manner. For future work this step could easily be automated and rendered more objective.

3.9 REFERENCES

Alt, J. C., 1995. Subseafloor processes in mid-ocean ridge hydrothermal systems. in *Seafloor Hydrothermal Systems-Physical, Chemical, Biological, and Geological Interactions*, edited by S. E. Humphris, R. A. Zierenberg, L. S. Mullineaux, and R. E. Thomson, AGU Geophysical Monograph 91, Washington, pp. 85-114.

Berge, P. A., 1991. Seismic anisotropy and velocity-porosity relationships in the seafloor. Ph.D. dissertation, Univ. of Hawaii, Honolulu.

Berge, P. A., Fryer, G. J., and Wilkens, R. H., 1992. Velocity-porosity relationships in the upper oceanic crust: theoretical considerations. *J. Geophys. Res.*, 97: 15239-15254.

Cheng, C. H., 1978. Seismic velocities in porous rocks: direct and inverse problems. Ph.D. thesis, Mass. Inst. of Tech., Cambridge.

Christensen, N. I., and Salisbury, M. H., 1975. Structure and composition of the lower oceanic crust. *Rev. Geophys. Space Phys.*, 13: 57-86.

Clark, S. P., 1966. *Handbook of physical constants*. Geol. Soc. Am. Memoir 97, 587 pp.

Hannington, M. D., Jonasson, I. R., Herzig, P. M., and Petersen, S., 1995. Physical and chemical processes of seafloor mineralization at mid-ocean ridges. in *Seafloor Hydrothermal Systems-Physical, Chemical, Biological, and Geological Interactions*, edited by S. E. Humphris, R. A. Zierenberg, L. S. Mullineaux, and R. E. Thomson, AGU Geophysical Monograph 91, Washington, pp. 115-157.

Herzig, P. M., Hannington, M. D., Scott, S. D., Maliotis, G., Rona, P. A., and Thompson, G., 1991. Gold-rich seafloor gossans in the Troodos ophiolite and on the Mid-Atlantic Ridge. *Econ. Geol.*, 86: 1747-1755.

Humphris, S. E., Herzig, P. M., Miller, D. J., and Shipboard Scientific Party of ODP Leg 158, 1995. The internal structure of an active sea-floor massive sulphide deposit. *Nature*, 377: 713-716.

Humphris, S. E., Herzig, P. M., Miller, D. J., et al, 1996. *Proc. ODP, Init. Repts.* 158, College Station, TX (Ocean Drilling Program).

Jacobson, R. S., 1992. Impact of crustal evolution on changes of the seismic properties of the uppermost ocean crust. *Rev. Geophys.*, 30: 23-42.

Johnston, J. E., Fryer, G. J., and Christensen, N. I., 1995. Velocity-porosity relationships of basalts from the East Pacific Rise. *Proc. ODP, Sci. Results*, 142, College Station, TX (Ocean Drilling Program).

Kuster, G. T., and Toksöz, M. N., 1974a. Velocity and attenuation of seismic waves in two-phase media, Part I, Theoretical formulations. *Geophysics*, 39: 587-606.

Kuster, G. T., and Toksöz, M. N., 1974b. Velocity and attenuation of seismic waves in two-phase media, Part II, Experimental results. *Geophysics*, 39: 607-618.

Ludwig, R. J., Fryer, G. J., Christeson, G. L., and Purdy, G. M., 1996 in review. Porosity and evolution of the shallow oceanic crust at the East Pacific Rise. *J. Geophys. Res.*

McGregor, B. A., Harrisson, C. G. A., Lavelle, J. W., and Rona, P. A., 1977. Magnetic anomaly pattern on the Mid-Atlantic Ridge crest at 26°N. *J. Geophys. Res.*, 82: 231-238.

Purdy, G. M., Sempéré, J.-C., Schouten, H., DuBois, D. L., and Goldsmith, R., 1990. Bathymetry of the Mid-Atlantic Ridge, 24-31°N: a map series. *Mar. Geophys. Res*, 12: 247-252.

Rona, P. A., Bogdanov, Y. A., Gurvich, E. G., Rimski-Kursakov, A., Sagalevitch, A. M., Hannington, M. D., and Thompson, G., 1993. Relict hydrothermal zones in the TAG hydrothermal field, Mid-Atlantic Ridge, 26°N, 45°W. *J. Geophys. Res.*, 98: 9715-9730.

Rona, P. A., Klinkhammer, G., Nelsen, T. A., Trefry, J. A., and Elderfield, H., 1986. Black smokers, massive sulphides and vent biota at the Mid-Atlantic Ridge. *Nature*, 321: 33-37.

Shearer, P., and Orcutt, J., 1985. Anisotropy in the oceanic lithosphere - theory and observations from the Ngendei seismic refraction experiment in the south-west Pacific. *Geophys. J. R. Astron. Soc.*, 80: 493-526.

Shearer, P. M., 1988. Cracked media, Poisson's ratio and the structure of the upper oceanic crust. *Geophys. J. R. Astron. Soc.*, 92: 357-362.

Smith, D. K., and Cann, J. R., 1992. The role of seamount volcanism in crustal construction at the Mid-Atlantic Ridge (24°-30°N). *J. Geophys. Res.*, 97: 1645-1658.

Sverdrup, H. U., Johnson, M. W., and Fleming, R. H., 1942. *The Oceans*. Prentice Hall, Englewood Cliffs, NJ, .

Thompson, G., 1983. Basalt-seawater interaction. in *Hydrothermal Processes at Seafloor Spreading Centers*, edited by P. R. Rona, K. Bostrom, and K. L. Smith, New York, pp. 225-278.

Tivey, M. K., Humphris, S. E., Thompson, G., Hannington, M. D., and Rona, P. A., 1995. Deducing patterns of fluid flow and mixing within the active TAG mound using mineralogical and geochemical data. *J. Geophys. Res.*, 100: 12,527-12,555.

Walsh, J. B., 1969. New analysis of attenuation in partially melted rock. *J. Geophys. Res.*, 74: 4333-4337.

Wilkens, R. H., Fryer, G. J., and Karsten, J., 1991. Evolution of porosity and seismic structure of upper oceanic crust: importance of aspect ratios. *J. Geophys. Res.*, 96: 17981-17995.